

MASTER OF SCIENCE THESIS

Numerical Simulation for the  
Pressure Distribution of the  
Compaction Roller in in-situ  
consolidation processes

Peixuan Zhou

Faculty of Aerospace Engineering · Delft University of Technology



# **Numerical Simulation for the Pressure Distribution of the Compaction Roller in in-situ consolidation processes**

MASTER OF SCIENCE THESIS

For obtaining the degree of Master of Science in Aerospace Engineering  
at Delft University of Technology

Peixuan Zhou

June 22, 2018



Copyright © Peixuan Zhou  
All rights reserved.

DELFT UNIVERSITY OF TECHNOLOGY  
FACULTY OF AEROSPACE ENGINEERING  
DEPARTMENT OF AEROSPACE STRUCTURES AND MATERIALS

**GRADUATION COMMITTEE**

Dated: June 22, 2018

Chair holder:

\_\_\_\_\_  
Pro. dr.ir. Rinze Benedictus

Committee members:

\_\_\_\_\_  
Dr. ir. Sonell Shroff

\_\_\_\_\_  
Dr. Julie Teuwen

\_\_\_\_\_  
Dr. Boyang Chen



## Abstract

Automated tape or fiber placement (ATP/AFP) with in-situ consolidation has been identified as a promising manufacturing technique for thermoplastic (TP) composites, which are highly in-demand in the aerospace industry for future aircraft structural applications. This manufacturing technique is attractive since it has the potential to eliminate the energy and time consuming autoclave consolidation. However, low quality is one of the biggest challenges in the application of in-situ consolidation. It seems that pressure contribution to the bond quality has received less attention than thermal one. Therefore, this work is initiated to simulate the pressure distribution between the compaction roller and the mandrel.

The objective in this work is to predict the pressure distribution in the contact area between the rubber-covered roller and the mandrel in room temperature by finite element methods (FEM). Rubber material is characterized by mechanical testing and then modeled as hyperelastic material. 3rd-order Ogden material model is found to well describe the strain-stress behavior of rubber material. The material constants are then implemented in FE models as an input. The pressure distribution is predicted by FE models and the influence of compaction force, rubber thickness, pre-stretching force on the pressure distribution are discussed, followed by an optimization between compaction force and rubber thickness. Experiments are conducted to validate the FE models regarding the three influencing factors, that are: (a). compaction force, (b). with/without pre-stretching and (c). various rubber thickness. Rubber deformation can be captured by the digital image correlation (DIC) Pressure distribution is obtained from the Prescale pressure measurement film produced by Fujifilm<sup>®</sup>, which are the films that show different color densities under different pressures. Experimental results of strain and pressure distribution are compared with FEM results, followed by discussions and conclusions.

It can be concluded that pre-stretching force should be used to avoid rubber-roller separation and prevent rubber from moving out to the sides. Both of the compaction force and rubber thickness affects the maximum pressure and contact length linearly. A trade-off between compaction force and rubber thickness can be made based on the force limit of the equipment and pressure requirements.



## Acknowledgements

I would first like to express sincerest gratitude to my thesis advisor Dr. ir. Sonell Shroff. When establish the research objectives, I was lost at all different aspects to improve the bond quality of in situ consolidation. It was she that helped me finalize the thesis topic. I could not have complete the thesis without her patient guidance and continuous encouragement.

I would also like to thank Dr. Boyang Chen and Dr. Julie Teuwen, who supervised me when Sonell had a maternity leave. Boyang helped me with simulation part of my thesis. He always thought in a broader perspective and could offered creative suggestions. Julie helped me with experimental part and guided me through the entire work. She has a sharp mind and was able to point out the weak points in my reasoning. Thanks to them, I can research more independently and think more critically.

I would like to acknowledge all the technicians in the DASML lab for helping me with my experiments. Thank Rob, Peter and ED for building the experimental setup; Thank Fred, Victor and Cees for providing me with instruction about sample preparation; Thank Frans and Marlies for Keyence supports; Thank Gertjan, Berthil and Johan for helping me with mechanical testing and final experimental validation. I had a tough time when material was delayed and when Keyence's lamp was broken so that testing plan was delayed. Without their passionate participation and input, the experiments could not have been completed.

Special thanks to Ozan for solving the FEM problems and checking my draft; to Willy for designing the experimental setup; to Tom for sharing scientific resources; to Lijian, Jianchen and Yuanyuan for their help in every little thing I encountered in my day life.

Finally, I must express my very profound gratitude to my parents and my relatives for their unconditional love and continuous encouragement. This Thesis would not have been completed without them. Thank you.

Delft, University of Technology  
June 22, 2018

Peixuan Zhou



# Table of Contents

Abstract.....	i
Acknowledgements.....	ii
1 Introduction.....	1
2 Literature Study .....	3
2.1 Bond theory .....	3
2.2 Finite element analysis for pressure distribution.....	7
2.3 Hyperelasticity.....	8
2.4 Pressure measurement .....	11
2.5 Conclusion .....	14
2.6 Research questions .....	15
3 Characterization of Rubber Material .....	17
3.1 Rubber testing.....	17
3.1.1 Tensile testing.....	17
3.1.2 Compressive testing .....	20
3.1.3 Planar tension testing.....	21
3.2 Material model selection .....	24
3.3 Conclusion .....	25
4 Finite element analysis .....	26
4.1 Model description .....	26
4.1.1 Two-dimensional static contact model.....	27
4.1.2 Three-dimensional static contact model.....	34
4.1.3 Two-dimensional rolling model .....	40
4.2 Model selection.....	42
4.2.1 Comparison between 2D and 3D static models.....	42
4.2.2 Comparison between 2D static and 2D rolling models .....	45
4.2.3 Conclusion.....	54
4.3 Results & discussion.....	47
4.3.1 Influence of the compaction force on the pressure distribution .....	47
4.3.2 Influence of rubber thickness on the pressure distribution.....	47
4.3.3 Influence of rubber's pre-stretching force on the pressure distribution .....	48
4.3.4 Rubber size optimization.....	51
4.4 Conclusion .....	52
5 Experimental validation.....	53
5.1 Experimental setup .....	53
5.2 Force calibration of the pneumatic cylinder .....	55
5.2.1 Test procedure .....	55
5.2.2 Results & discussion .....	55
5.3 Validation of rubber's displacement/strain field.....	56
5.3.1 Sample preparation.....	56
5.3.2 Test procedure .....	56
5.3.3 Results & discussion .....	59
5.4 Validation of contact pressure .....	63

5.4.1 Calibration of the pressure sensitive film.....	64
5.4.2 Test procedure .....	66
5.4.3 Results & discussion .....	66
5.5 Conclusion .....	66
6 Conclusion .....	70
7. Recommendation .....	72
References .....	73
A. Appendices.....	76
Appendix 1. Sample manufacturing for rubber characterization.....	76
Appendix 2. Detailed descriptions of finite element models.....	78
Appendix 3. Image process of digital image correlation .....	81

# List of Figures

Figure 1.1 Illustration of the in-situ consolidation system .....	1
Figure 1.2 Thermoplastic tape winding process with in-situ consolidation .....	2
Figure 2.1 Illustration of the bonding process between two thermoplastic pieces .....	4
Figure 2.2 Processing window of experimental parameters to complete intimate contact for APC-2 graphite/PEEK composite .....	5
Figure 2.3 Effect of process parameters coupling on bond degree .....	5
Figure 2.4 Time to achieve intimate contact versus consolidation pressure for an APC-2 laminate/PEEK film lap-shear coupon .....	6
Figure 2.5 (a) Effect of consolidation force on bond strength with different temperature and velocity and (b) effect of consolidation force on bond strength with different temperature and velocity .....	6
Figure 2.6 Abaqus finite elements thermo-mechanical model .....	7
Figure 2.7 Simulating of the deformation of the rubber coated roller .....	8
Figure 2.8 Stress-strain curve (a) linear elastic (b) hyperelastic .....	8
Figure 2.9 Schematic illustrations of deformation modes .....	10
Figure 2.10 (a) C film gets colored when microcapsules burst under pressure; (b) The magnitude of applied pressure is determined using a color intensity chart .....	12
Figure 2.11 (a). Scanned stain image obtained from uniform pressure, (b). Pressure sensitive film calibration apparatus and (c). calibration curve .....	12
Figure 2.12. (a). The prepreg is placed over samples of pressure sensitive film. (b). Setup is heated using an infrared lamp. (c). Placement machine performing a compaction pass over the pressure sensitive film .....	13
Figure 2.13. (a). Untreated digital pressure imprint for 10 kg on compaction roller with a crop rectangular. (b). Generated pressure map of the cropped image .....	13
Figure 2.14 Thesis outline .....	16
Figure 3.1 Uniaxial tensile testing .....	18
Figure 3.2 Experimental data for Uniaxial tensile testing .....	19
Figure 3.3 Uniaxial compressive testing .....	20
Figure 3.4 Stress-strain curve of compressive testing under three loading cycles up to different compressive strains .....	20
Figure 3.5 Experimental data for Uniaxial compressive testing .....	21
Figure 3.6 Gluing the mental plates to rubber film .....	22
Figure 3.7 Planar tension testing .....	22
Figure 3.8 Experimental data for planar tension testing: (a) under with 20 loadings for one sample up to two different strain limits: first 0.5 and then 0.8 of the nominal strains; (b) under 1st- loading; (c) under 20th-loading .....	23
Figure 3.9 Comparison between planar tension test and tensile test in experiments (left) and in literature for the unfilled silicone rubber RTV 141(right) .....	24
Figure 3.10 Fitting of the three hyperelastic models with uniaxial data (left) and corresponding planar data .....	25
Figure 3.11 Comparison of the calculated planar curve and tensile curve .....	25
Figure 4.1 Two-dimensional FE model under plane strain condition: whole model (left) and half model (right) .....	27
Figure 4.2 Coupling in roller (left) and mandrel (right) under symmetric condition .....	28
Figure 4.3 2D FE model with two interactions: Int-1 and Int-2 .....	28
Figure 4.4 Step explanation for 2D static model .....	29
Figure 4.5 Mesh strategy: bias direction (left) and results locations (right) .....	31
Figure 4.6 Mesh refinement in circumferential direction .....	31
Figure 4.7 Mesh refinement in radial direction .....	31
Figure 4.8 Explanations of 2D element: Full/reduced integration and first/second-order	

interpolation .....	32
Figure 4.9 Radial logarithmic strain and radial stress at the element center .....	33
Figure 4.10 Selection elements for radial logarithmic strain and radial stress .....	33
Figure 4.11 Deformation comparison between linear and quadratic element .....	33
Figure 4.12 3D FE model with symmetric conditions about xy and yz planes (left) and the side view of 3D model: before (middle) and after pressing (right).....	34
Figure 4.13 Step explanation of 3D model.....	35
Figure 4.14 Mesh strategy: bias direction (left) and results locations (right).....	35
Figure 4.15 Mesh strategy in the out-of-plane direction: uniform mesh (left) and uniform + biased mesh.....	36
Figure 4.16 Comparisons of S22, S33, LE22, LE33 and CPRESS between a uniform mesh and a uniform + bias mesh when $c = 0.5$ mm .....	37
Figure 4.17 Mesh refinement in circumferential direction .....	37
Figure 4.18 Mesh refinement in radial direction .....	37
Figure 4.19 S22 distribution along the out-of-plane direction .....	38
Figure 4.20 S22 (right) and LE22 (left) distribution along the out-of-plane direction (S3 direction) when the four outermost layers of elements in rubber are removed.....	38
Figure 4.21 Distributions of S22, S33, LE22, LE33 and CPRESS along the out-of-plane direction under various mesh sizes .....	39
Figure 4.22 Mesh refinement of the 5th point ( $x = -21$ ) in the out-of-plane direction (S3 direction) .....	39
Figure 4.23 Comparison of out-of-plane logarithmic strain between linear and quadratic element	40
Figure 4.24 Step explanation for 2D rolling model.....	40
Figure 4.25 Pressure distribution of the rubber's outer surface over rolling time.....	41
Figure 4.26 Maximum pressure along the rubber's outer surface line over time using different mesh sizes in circumferential direction (left) and averaged pressure after stabilization under different mesh size.....	42
Figure 4.27 Comparison of contact pressure between 2D and 3D static models .....	43
Figure 4.28 Comparison of contact pressure between 2D and 3D static models in the circumferential direction (left) and in the out-of-plane direction (right).....	43
Figure 4.29 Comparison of out-of-plane logarithmic strain between 2D (upper) and 3D (lower) static models .....	44
Figure 4.30 Comparison of vertical logarithmic strain between 2D and 3D static models.....	44
Figure 4.31 Comparison of vertical logarithmic strain (LE22) between 2D and 3D static models in the out-of-plane direction .....	44
Figure 4.32 Comparisons of contact status (left), CSHEAR (middle) and circumferential stress ( $S_{\theta}$ ) distribution (right) at rolling time $t = 0$ and $t = 4$ s in the 2D rolling model.....	45
Figure 4.33 COPEN distribution along the rubber's inner surface over time (left y axis) and the maximum COPEN over time (right y axis) .....	46
Figure 4.34 The Pressure distribution at different rolling time in the 2D rolling model (left) and comparisons of pressure distribution between 2D static and rolling model (right).....	46
Figure 4.35 Pressure distribution between the mandrel & a 5 mm thick rubber under different forces.....	47
Figure 4.36 Pressure distribution under different rubber thicknesses .....	47
Figure 4.37 Pressure distribution with pre-stretched rubber and non-stretched rubber under different loads .....	48
Figure 4.38 (a) 2D rolling models for pre-stretched rubber (upper) and unstretched rubber (lower) and (b) Comparison of the maximum pressure over time between pre-stretched rubber and non-stretched rubber .....	49
Figure 4.39 The comparison of circumferential stress distribution between pre-stretched rubber and non-stretched rubber at roller time $t_{rolling} = 0$ s and $t_{rolling} = 4$ s .....	50
Figure 4.40 Effects of rubber thickness on maximum pressure under same compaction force (left) and effects of compaction force on maximum pressure under same rubber thickness (right) .....	51

Figure 4.41 Effects of rubber thickness on contact length under same compaction force (left) and effects of compaction force on contact length under same rubber thickness (right) .....	51
Figure 5.1 Experimental setup .....	53
Figure 5.2 Control system of the air pressure.....	54
Figure 5.3 Results of pressure sensitive film: unevenly distributed pressure (left) and evenly distributed pressure (right).....	54
Figure 5.4 Experimental setup of the force calibration for the pneumatic cylinder .....	55
Figure 5.5 Force - air pressure curves of the pneumatic cylinder under two loading cycles: experimental data (left) and fitted data (right).....	55
Figure 5.6 Paint the speckle pattern to stretched 5 mm-thick rubber rings (left), the roller covered with stretched 10 mm-thick rubber before (middle) and after paint (right) .....	56
Figure 5.7 Experimental setup of DIC.....	57
Figure 5.8 Initial status of one rubber sample (15 mm thick, No.4).....	57
Figure 5.9 Vertical logarithmic strain distribution of 10 mm-thick rubber: initial status (left), start to rotate (middle) and end of rolling (right).....	58
Figure 5.10 The grid in the area of interest (ROI) of the undeformed image (reference image) ....	58
Figure 5.11 Location of the vertical displacement and vertical logarithmic strain results in DIC (left), 2D FEM (middle) and 3D FEM (right) .....	59
Figure 5.12 Vertical displacement and vertical strain comparisons of 5 different rubber sizes between DIC, 2D and 3D FEM static results .....	60
Figure 5.13 Vertical displacement distribution under different loads and through thickness of 5 different rubber sizes between DIC and 2D FEM static results .....	61
Figure 5.14 Comparison of the vertical logarithmic strain distribution between DIC and 2D FEM before and during rolling .....	63
Figure 5.15 Averaged LE22 at the mid-point along the mid-line under different load levels during rolling.....	63
Figure 5.16 Calibration setup (left) and stain image under 1300 N (upper right) and from literature (lower right).....	64
Figure 5.17 Stain image scan (left), transformation to grey level (middle), and grey level map (right) .....	64
Figure 5.18 Stain image with two contour filtered by two thresholds: ratio 1 = 0.08 (blue) and ratio 2 = 0.3 (green) .....	65
Figure 5.19 Calibration curves of three ratio combinations (left) and the comparison between the corresponding calculated forces and applied force.....	65
Figure 5.20 Experimental setup for pressure measurement.....	66
Figure 5.21 Comparison of room condition between calibration and experiment of pressure measurement .....	66
Figure 5.22 Pressure comparison between experimental and FEM results under two loads.....	67
Figure 5.23 Comparison of pressure map for 5 mm stretched and rubber under two loads .....	68
Figure A1.1 Mold for rubber ring manufacturing .....	76
Figure A1.2 Injecting process.....	76
Figure A1.3 Post processing.....	77
Figure A1.4 Procedures of cylinder sample manufacturing .....	77
Figure A1.5 Procedures of film sample manufacturing: molding (left), vertically curing (middle) and mold releasing (right).....	78
Figure A1.6 Gluing the mental plates to rubber film.....	78
Figure A2.1 Interaction setup .....	79
Figure A2.2 Interaction properties setup .....	79
Figure A2.3 Step setup for 2D static model .....	80
Figure A2.4 Step setup for 3D model.....	81
Figure A2.5 Step setup for 2D rolling model .....	81
Figure A3.1 Flow chart to obtain the pressure map from the scanned pressure imprint image .....	82
Figure A3.2 Graphical output during image processing: (a) scanned image of the pressure imprint,	

(b) convert the image to grayscale, (c) invert the grayscale map, (d) crop the image and remove the background, (e) grayscale map and (f) pressure map .....	83
Figure A3.3 Illustration of averaging the grayscale map .....	84
Figure A3.4 Pressure results using different block size and border size .....	84

# List of Tables

Table 3.1 Dimension comparison between ISO and ASTM standards, and the chosen dimensions .....	18
Table 3.2 Material constants and stable limits of hyperelastic material models fitted on experimental data from all tests .....	25
Table 4.1 Master surface and slave surface in the interaction setting .....	28
Table 4.2 Summary of loads, BCs and interactions and their actives in each step .....	29
Table 4.3 Mesh sizes for 2D model: rubber, roller and mandrel .....	31
Table 4.4 Boundary conditions of different symmetric planes.....	34
Table 4.5 Mesh sizes for 3D model: rubber, roller and mandrel .....	36
Table 4.6 Summary of loads, BCs and interactions and their actives in each step .....	41
Table 5.1 Numbering of the five sizes of the rubber ring.....	54
Table 5.2 All seven load levels that are used for DIC measurement.....	57
Table 5.3 Three ratio combinations found by comparing applied and calculated force.....	65
Table 5.4 Maximum pressure and contact length obtained from the pressure films and 3D FEM under two different compaction forces. ....	67



# List of Abbreviations

2D	Two-Dimensional
3D	Three-Dimensional
AFP	Automated Fiber Placement
ATP	Automated Tape Placement
BC	Boundary Condition
COPEN	The gap between two adjacent surfaces
COV	Coefficient of Variation
CPRESS	Contact Pressure
CSHEAR	Friction
CSTATUS	Contact Status
LE	Logarithmic strain
LLW	Super Low Pressure Range
DIC	Digital Image Correlation
FE	Finite Element
FEA	Finite Element Analysis
FEM	Finite Element Method
ILSS	Inter-Laminar Shear Strength
MPC-Beam	Multiple Point Constraint of Beam type
RH	Relative Humidity
TP	Thermoplastic
TPC	Thermoplastic Composites
SD	Standard Deviation



# List of Symbols

$t_b$	Autohesion Time
$t_{ic}$	Intimate Contact Time
$W$	Strain-Energy Function
$I_i$	Invariants of Green Deformation Tensor
$E_s$	Nominal Strain
$S_e$	Nominal Stress
$s$	Standard Deviation
$C_v$	Coefficient of Variation
LE22	Vertical Logarithmic Strain
LE33	Out-of-plane Logarithmic Strain
U2	Vertical Displacement
S22	Vertical stress
S33	Out-of-plane Stress
$S_\theta$	Circumferential Stress
$t_{rolling}$	Rolling Time
$l$	Contact Length



# 1 Introduction

Automated tape or fiber placement (ATP/AFP) with in-situ consolidation has been identified as a promising manufacturing technique for thermoplastic composites (TPC), which are highly in-demand in the aerospace industry for future aircraft structural applications. This manufacturing technique is attractive since it has the potential to eliminate the energy and time consuming autoclave consolidation. During the process, the thermoplastic tape is laid on a mold/mandrel and consolidated simultaneously given a large amount of heat and pressure, as illustrated in Fig 1.1. However, low quality and limited production rate are two of the biggest challenges in the application of in-situ consolidation. Investigations (Lionetto, Dell'Anna, Montagna, & Maffezzoli, 2016; Yu, Shi, He, Kang, & Deng, 2017) have been carried out to improve the bond quality as well as manufacturing speed. It seems that the contribution of pressure has received less interest than that of temperature, despite the fact that they are of equal importance for quality improvement. In literature, thermal distribution is usually focused on while assuming pressure stays constant (Lionetto et al., 2016), or at a very high value (Schell, Guillemot, Binetruy, & Krawczak, 2009), or using consolidation force instead (Yu et al., 2017). But it is not true in real case since the pressure is not uniformly distributed in the contact area (nip point). Even worse, too high pressure also leads to the degradation of bond quality (Yu et al., 2017), not to mention the damage it causes to costly roller, which is often worn and replaced. Nevertheless, pressure is considered as one of the most important parameters that determines the bond quality in analytical theories, including intimate contact (Chao, M and Gillespie Jr, 1994), void formation (Pitchumani, Ranganathan, Don, Gillespie, & Lamontia, 1996) and material deformation (Bourban, Bernet, Zanetto, & Manson, 2001) under in-situ consolidation. Therefore, a study is initiated to investigate the relation between pressure distribution in the contact area and the force applied to the roller, depicted in Fig 1.1 as pressure roller.

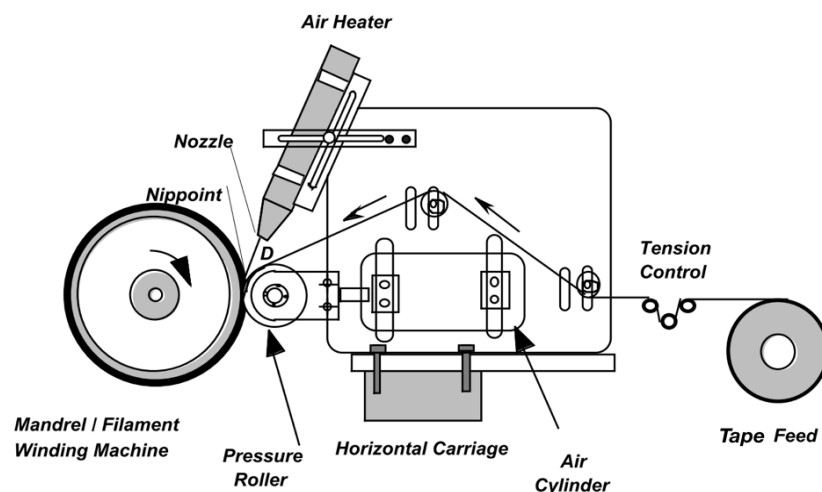
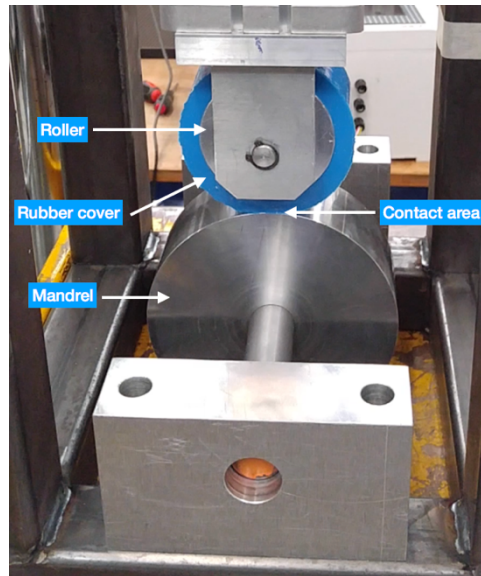


Figure 1.1 Illustration of the in-situ consolidation system (Shih & Loos. A. C., 1997)

Generally, a roller is covered with a rubber ring, forming a stiff-soft roller combination to provide larger contact area when compared to rigid rollers. The preliminary experimental setup is shown in Fig 1.2. The roller and the mandrel are made of aluminum. Also, the roller is covered with a silicone rubber with relative high temperature resistance is selected since consolidation temperature of TP tape is around 350°C. During the in-situ consolidation, TP tape is coming from the feeder to the mandrel, heated up to melting temperature and pressed by the roller. However, separation between roller and rubber occurs and rubber is moving out to the sides, leading to non-uniform pressure in the contact area and thus poor

quality. This can be possibly prevented by using a pre-stretching force to the rubber ring. Hence, finite element analysis (FEA) are used to simulate the pressure distribution of pre-stretched and unstretched rubber rings. Furthermore, the influence of compaction force and rubber thickness on pressure distribution will be investigated by FEA.



*Figure 1.2 Thermoplastic tape winding process with in-situ consolidation*

This work is focused on the simulation of the pressure distribution in the contact area at room temperature, which is the first step towards the quality improvement for ATP/AFP with in-situ consolidation processes. The objectives are the prediction of pressure distribution and the investigation of the influences of compaction force, rubber thickness and with/without pre-stretching force on the pressure distribution, followed by rubber size optimization. Literature is reviewed and research questions are raised to achieve the objectives.

The novelty of this work lies in the simulation of pressure prediction and the experimental validation of FE models by pressure measurement, which is rare in the existing literature (Batra, Levinson, & Betz, 1976; Lynch, 1969). Also, material characterization of selected silicone rubber is made to simulate rubber behavior more accurately when compared to current studies (Batra, 1980; Levy et al., 2012) where material models are obtained either from previously studies (Batra, 1980) or by limited experimental work (Levy et al., 2012). Furthermore, this also generates valuable input for future work, such as the simulations of bond quality and the optimization of processing window.

## 2 Literature Study

The literature study consists of four parts. First of all, bonding theories of the thermoplastic composites are explained in in-situ consolidation, which is the process used in this work. The influences of temperature, pressure and processing time on the bond quality are also discussed. In the second part, finite element analysis (FEA) of pressure distribution between rubber and mandrel is reviewed. In the third part, hyperelasticity of rubber materials is elaborated, where the implementation of hyperelastic material models in Abaqus® is also discussed. Lastly, pressure measurement is explained by using pressure sensitive films.

### 2.1 Bond theory

The manufacturing process for TPC is usually composed of three stages (Schell et al., 2009): applying pressure to initiate intimate contact, heating up the material above the melting point of the resin matrix for a certain amount of time to achieve a full consolidation, and cooling down under the applied pressure. Fusion bonding is a typical manufacturing technique for TPC, which mainly contains the process of heat-transfer and consolidation (C Ageorges, Ye, & Hou, 2001). The consolidation process will be elaborated in this section, followed by the three experimental parameters that influences the bond quality, including temperature, pressure and processing time.

#### 2.1.1 Consolidation

An understanding of consolidation is an essential step towards quality improvement of in-situ consolidation for TPC, during which fusion bonding is the main physical mechanism as stated by Schell *et al.* (Schell et al., 2009), including intimate contact and autohesion (Christophe Ageorges, Ye, Mai, & Hou, 1998b). Wool and co-workers (Kim & Wool, 1983) developed the healing theory, which contains the establishment of intimate contact and the development of autohesion. The bond strength (Mantell & Springer, 1992; Pitchumani et al., 1996; Tierney & Gillespie, 2006) is also developed during these processes. As shown in Fig 2.1, an intimate contact is initiated between contact surfaces, which is rough with gaps existing between plies. Heat and pressure are applied locally, resulting in viscous deformation in the contact area and an increase of the intimate contact degree. This process depends on both temperature and pressure. Once the surfaces are intimately contacted, all the physical barriers existing between the surfaces disappear and polymer chains start to diffuse across the interface (Ageorges et al., 1998b) in the autohesion process. As a result, bonding time contains intimate contact time and autohesion time. Intimate contact time is referred to the time required to reach fully intimate contact while autohesion time means the time for polymer chains to completely diffuse across the interfaces (Lee & Springer, 1987).

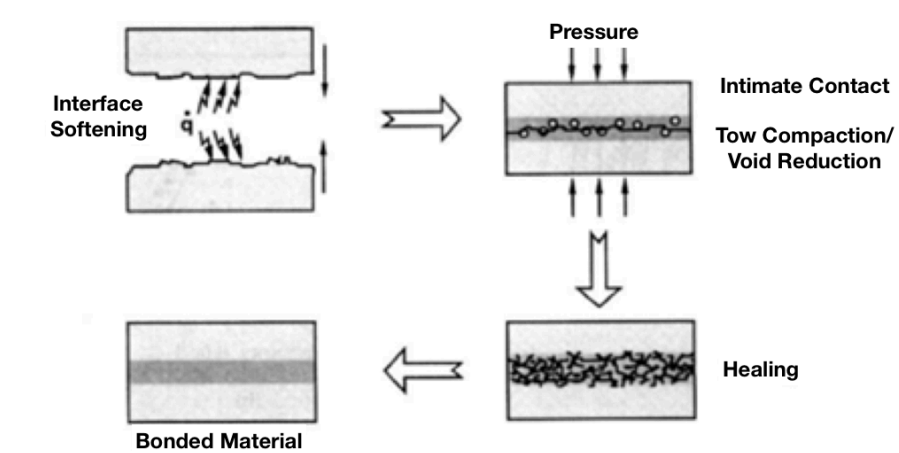


Figure 2.1 Illustration of the bonding process between two thermoplastic pieces, including intimate contact and healing processes (He, Alfred, & Loos, 1985)

In order to quantify bond strength, the degree of bonding has been studied by various researchers (Bastien & Gillespie, 1991; Lee & Springer, 1987; Mantell & Springer, 1992). It is dependent on the material and process parameters of the bonding and healing, including the roughness, viscosity, pressure, temperature and process time (Schell et al., 2009), etc. As mentioned before, bonding time contains intimate contact time and autohesion time. In some material systems, autohesion time is much faster than intimate contact time and thus the degree of bonding can be reduced to the degree of intimate contact as discussed by Mantell *et al.* (Mantell & Springer, 1992), which is the percent of the contact surfaces that achieve intimate contact. A dimensionless parameter  $\Omega$  is introduced Buttler (Butler, Mccullough, Pitchumani, & Gillespie, 1998), which is a time ratio between the time of healing process ( $t_h$ ) over the time of intimate contact ( $t_{ic}$ ). By comparing  $\Omega$  to 1, it indicates whether the rate-controlling mechanism of bond strength is determined by the intimate contact or healing process.

It should be noted that semi-empirical (Schell et al., 2009) and numerical (Christophe Ageorges, Ye, Mai, & Hou, 1998a; Kim & Wool, 1983; Lee & Springer, 1987; Mantell & Springer, 1992; Pitchumani et al., 1996; Schell et al., 2009; Wool, Yuan, & McGarel, 1989) models have also been well studied to explain the phenomena such as intimate contact and healing processes existed during bonding. Analytical results are compared with experimental data to predict/verify the analytical models, including interface temperatures, melting time and intimate time, autohesion time (Lee & Springer, 1987), and so forth. Consequently, a processing window was established by Lee *et al.* (Ageorges et al., 1998b) (shown in Fig 2.2), which was verified by experiments tested with APC-2 graphite/PEEK composite. In the latest studies, Yu *et al.* (Yu et al., 2017) made a valuable contribution to improve the inter-laminar shear strength (ILSS) by developing theoretical model of tape winding process using thermoset prepreg. Furthermore, the processing window based on the degree of bonding is written as a function of heating temperature and consolidation force is simulated under a constant winding velocity, as shown in Fig 2.3. When increasing temperature, a good bond can be achieved by smaller pressure. However, a combination of high pressure and high consolidation force leads to the degradation of bond quality, which will be further elaborated later.

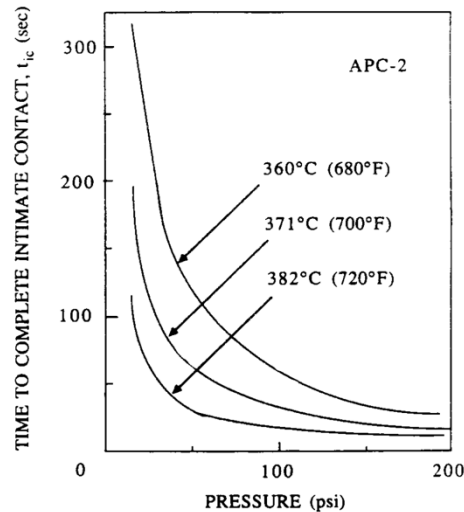


Figure 2.2 Processing window of experimental parameters to complete intimate contact (Degree of intimate contact  $D_{ic} = 1.0$ ) for APC-2 graphite/PEEK composite, including time, pressure and temperature (Lee & Springer, 1987)

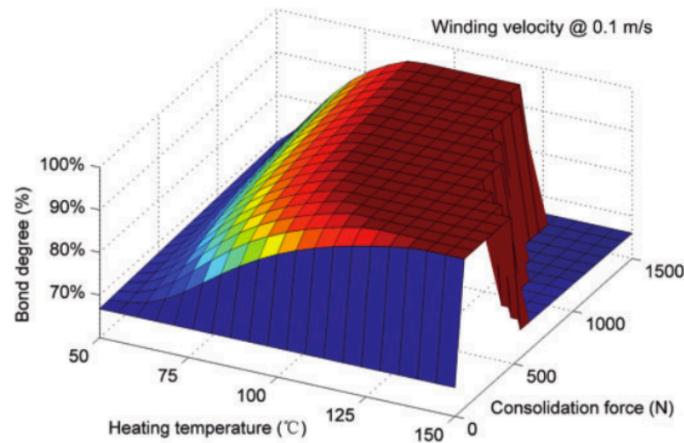


Figure 2.3 Effect of process parameters coupling on bond degree (Yu et al., 2017)

## 2.1.2 Influence of experimental parameters

### Temperature

The interface temperature has a significant impact on bonding quality as highlighted by Schell *et al.* (Schell et al., 2009). For autohesion, the interface temperature has to rise above the melting point so that the polymer matrix is able to diffuse across the interfaces (Bourban et al., 2001). When the temperature is below melting point, the chain motion is prevented by the crystalline section of the semi-crystalline polymer matrix. The higher the interface temperature, the faster the polymer chains move and entangle through the interface, causing a superior bond strength (C Ageorges et al., 2001; Kim & Wool, 1983; Lee & Springer, 1987; Pitchumani et al., 1996; Wool et al., 1989). On one hand, lower temperatures may result in lower bond strength due to the fact that the transportation of molecular chains is slower at the contacting interfaces when the temperature is lower (F. Yang & Pitchumani, 2003). On the other hand, the temperature cannot exceed the degradation temperature, otherwise polymer chains would start to degrade. Grove analyzed the consolidation process of AS4/PEEK composite and effective consolidation was introduced (Grove, 1988). Depending on the defined consolidation temperature at the interfaces, the maximum possible layup speed can be obtained given a

particular laser power.

### Pressure

The influence of the applied pressure on the establishment of intimate contact has been studied for various manufacturing processes, such as fusion bonding and resistant welding. Those two processes are comparable with the main difference lying in the heating methods. Pressure plays a vital role in both intimate contact and autohesion. Even though autohesion is only a function of temperature and resistance time in the model proposed by Ageorges *et al.* (Ageorges et al., 1998b), pressure also helps to initiate and maintain an intimate contact, which is the prerequisite of autohesion in order to achieve good bond strength. As shown in Fig 2.4, the intimate contact time ( $t_{ic}$ ) is plotted with respect to the pressure for carbon fibers reinforced PEEK composite (APC-2) given a constant power. It seems that there is a threshold value for the pressure, above which pressure is not a key factor anymore for resistance welding process (Ageorges et al., 1998b). For one thing, a long process time is needed under this threshold, causing high cost and small production volume (Ageorges et al., 1998b). For another, the high pressure required for consolidation leads to warpage/flow in the higher temperature areas (Benatar, A. ; Gutowski, 1986).

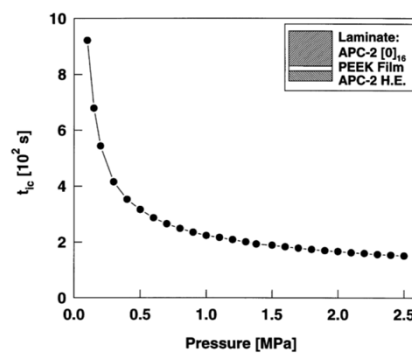


Figure 2.4 Time to achieve intimate contact versus consolidation pressure for an APC-2 laminate/PEEK film lap-shear coupon using a power level of  $52 \text{ kW m}^{-2}$  (Ageorges et al., 1998b)

Studying the influence of pressure on thermoset composite is also beneficial to knowing more about the material behavior of TPC, owing to similarity in the processing mechanisms in the consolidation of TPC and curing for thermoset composite. Similar conclusions on the effect of pressure can also be made for thermoset composite. This was done experimentally by Yu *et al.* (Yu et al., 2017), proving that bond quality of thermoset composite drops dramatically when pressure is too high as illustrated in Fig 2.5. This is because resin is squeezed out under high pressure. The fibers in the tape and the fibers in the composite substrate get contact with each other at the interface when increasing pressure, leading to the degradation of bond quality.

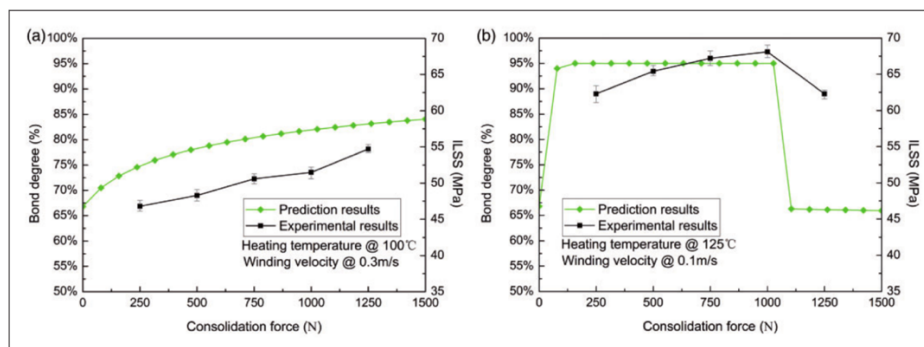


Figure 2.5 (a) Effect of consolidation force on bond strength with different temperature and velocity and (b) effect of consolidation force on bond strength with different temperature and velocity. ILSS: inter-laminar shear strength (Yu et al., 2017)

### Processing time

The effects of processing time were also discussed by Lee *et al.* (Lee & Springer, 1987), which consists of intimate contact time ( $t_{ic}$ ) and autohesion time ( $t_b$ ). Certain amount of time is required to fully develop intimate contact and for polymer chains to diffuse across the interfaces. For resistance welding, too-low processing time and/or too-low power levels cause two failure mechanisms in the lap shear test: (a) interfacial failure of the joint and (b) cohesive failure of the heating element (Christophe Ageorges, Ye, & Hou, 2000a), where the latter is not applicable in this study. However, too-long processing time and/or too-high power levels result in the resin degradation (Hinkley, Messier, & Marchello, 1997) and/or de-consolidation within several layers inside the laminates. Ageorges *et al.* (Ageorges, Ye, & Hou, 2000) discover that the processing time is optimized experimentally according to a criterion of maximum lap shear strength (LSS) and is compared with  $t_{ic}$  and  $t_b$  predicted by a three-dimensional transient model (FEM) they developed before (Christophe Ageorges et al., 1998a, 1998b)

## 2.2 Finite element analysis for pressure distribution

Pressure distribution can be obtained using finite element method (FEM), which is a useful tool to investigate the roller-mandrel contact problem for in-situ consolidation. A three-dimensional FE model was developed by Tannous *et al.* (Tannous, Barasinski, Binetruy, & Courtemanche, 2016) in order to investigate the thermal and mechanical phenomena for the in-situ consolidation tape winding process. The thermo-mechanical model is revealed in Fig 2.6. The roller is meshed with 3D quadratic elements while the tape and the mandrel with 3D shell elements. In case of the depositing tape, one end is attached to the mandrel and the other is subjected to a tape tension. Ten layers of substrate are already placed on the mandrel before the simulation starts and they are modeled by cylindrical shell.

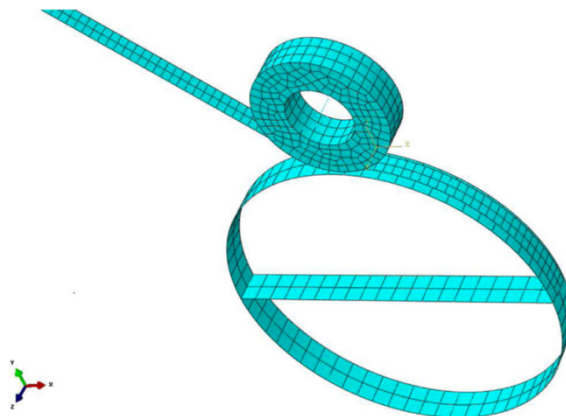


Figure 2.6 Abaqus finite elements thermo-mechanical model (Tannous *et al.*, 2016)

The boundary conditions are also discussed. In case of the roller, it has the freedom to move around its rotational axis (z axis) and in the vertical direction (y direction). The roller should be deformable for providing a uniform pressure distribution but the inner surface should be non-deformable since the roller attaches to a rigid metal axis. In order to simulate this, a MPC-Beam (multiple point constraint of beam type) is introduced between a node that belongs to the beam, which is assigned to the rotational axis and internal surface of the roller. The mandrel and the composite substrate are modeled as rigid materials with the thermal properties.

When considering interaction, normal contact is used between the tape and composite substrate to simulate the deformable roller, which also enables the tape to have the shape of the mandrel. The tangential contact is taken into account due to friction, which ensures the

roller to rotate with the mandrel.

Pressure distribution between a rubber covered roller and a rigid flat surface was simulated by Batra (Batra, 1980) and Levy *et al.* (Levy et al., 2012). Rubber is modeled as a Mooney-Rivlin material and material constants are gained from the tensile test only. A force is applied vertically on the roller center and the penalty method (Kikuchi N. a., 1988) is used for the contact with the substrate. Fig 2.7 shows the displacement field as well as pressure distribution under the roller. However, no experimental work was done to validate the model. As a result, similar approach will be applied to simulate the pressure distribution between rubber and mandrel. However, more mechanical tests will be performed to have a more accurate hyperelastic model describing the rubber behavior. Furthermore, A step of pre-stretching the rubber will be added prior to the pressing step to mimic the pre-stretching force. Also, experimental validation will be conducted in this work to validate FE models.

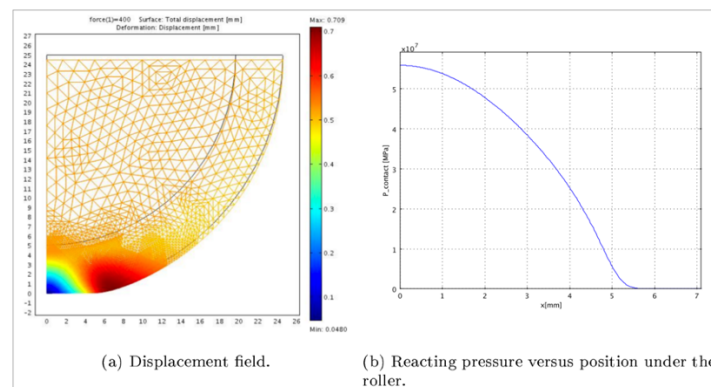


Figure 2.7 Simulating of the deformation of the rubber coated roller (Levy et al., 2012)

## 2.3 Hyperelasticity

Material characterization of rubber is required run the FE simulations. Rubber materials exhibit nonlinear elastic behavior, which is also known as hyperelasticity. They often remain elastic for large deformation (around 300%) under relatively small force compared to elastic materials, as indicated in Fig 2.8. The nonlinearity of stress-strain relation implies Hooke's law is not applicable anymore (Martins, Jorge, & Ferreira, 2006). As a result, great interest has been received in characterization of these rubber materials.

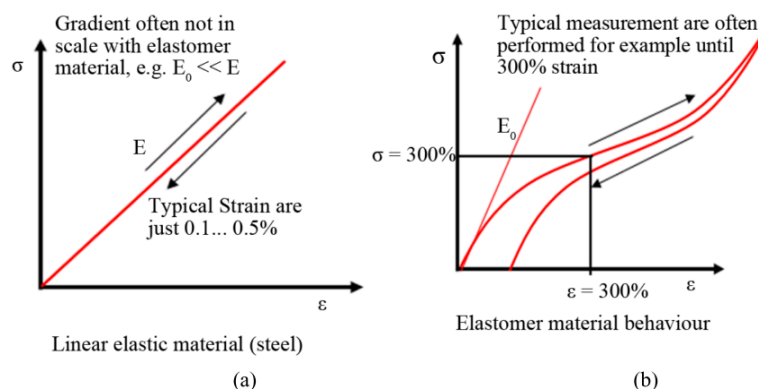


Figure 2.8 Stress-strain curve (a) linear elastic (b) hyperelastic (Abubakar, Myler, & Zhou, 2016)

Instead of Hooke's law, strain-energy functions  $\mathcal{W}$  are used to describe the stress-strain relation of rubberlike materials in terms of three strain invariants ( $I_1$ ,  $I_2$  and  $I_3$ ), which is the energy per unit volume at that point in material (Shahzad, Kamran, Siddiqui, & Farhan, 2015;

Yousefpour & Ghasemi Nejhada, 2001). It should be noted that the volume refers to the volume in the initial configuration.

$$W = f(I_1, I_2, I_3)$$

2.1

where  $I_1$ ,  $I_2$  and  $I_3$  are the three invariants of Green deformation tensor that are defined based on principal stretch ratios  $\lambda_1$ ,  $\lambda_2$  and  $\lambda_3$  given by (Dolwichai, 2006)

$$\begin{aligned} I_1 &= \lambda_1^2 + \lambda_2^2 + \lambda_3^2 \\ I_2 &= \lambda_1^2 \lambda_2^2 + \lambda_2^2 \lambda_3^2 + \lambda_3^2 \lambda_1^2 \\ I_3 &= \lambda_1^2 \lambda_2^2 \lambda_3^2 \end{aligned}$$

2.2

Rubber materials are often assumed to be incompressible and thus  $I_3 = 1$  (Shahzad et al., 2015). It indicates the strain-energy function is only dependent on two variables  $I_1$  and  $I_2$  in the form of

$$W = W(I_1 - 3, I_2 - 3)$$

2.3

Different strain-energy functions, also known as hyperelastic material models, have been developed and applied in rubber characterization. The commonly used models are Mooney-Rivlin model (Mooney, 1940), polynomial model and Ogden model (Ogden, 1972), etc. The first two are dependent on invariants of the right Green deformation tensor as stated in Eq 2.1 - 2.2 and the last one depends on principal elongations.

Mooney-Rivlin model. The Mooney-Rivlin model is the special case of polynomial model and has a good fit for moderately large stains regarding uniaxial elongation and shear deformation (Mooney, 1940; Rivlin, 1948). For incompressible rubber, model has the form

$$W = C_{10}(\bar{I}_1 - 3) + C_{01}(\bar{I}_2 - 3)$$

2.4

where  $I_i$  are the invariants of Green deformation tensor.

Full polynomial model. Polynomial model can be written as

$$W = \sum_{i,j=0}^N C_{ij} (\bar{I}_1 - 3)^i (\bar{I}_2 - 3)^j$$

2.5

where  $C_{ij}$  - material constants that control the shear behavior and can be determined from uniaxial, biaxial and planar tests.

$N$  = Number of terms in strain energy function.

Ogden model. The Ogden model is also widely used due to its high versatility to almost any testing data (Meunier, Chagnon, Favier, Orgé As, & Vacher, 2008). Moreover, it has been observed that Ogden model has a good fit to Treloar's experimental data up to 700% of deformation of unfilled rubber (Treloar, 1975). However, it is not recommended to rely on this model with limited test (e.g. just uniaxial tension) (Shahzad et al., 2015). Ogden model can be written in the form of

$$W = \sum_{i=1}^N \frac{2\mu_i}{\alpha_i^2} (\bar{\lambda}_1^{\alpha_i} + \bar{\lambda}_2^{\alpha_i} + \bar{\lambda}_3^{\alpha_i} - 3)$$

2.6

where  $\lambda_i$  is the deviatoric principal stretch

$\mu_i, \alpha_i$  are temperature dependent material properties.

There are several ways to characterize the mechanical properties of rubber materials. Commonly used methods (Sasso, Palmieri, Chiappini, & Amodio, 2008) are marked in Fig 2.9 below. Tensile testing can be performed in uniaxial, planar or equibiaxial states while compressive testing is generally used in uniaxial state (Pearson & Pickering, 2001). It should be noted that an extensometer cannot provide accurate results for small strain measurements (Gent, 2012). Alternatively, Digital image correlation (DIC) can be used for more accurate results and it is also possible to obtain local strain field on a deformed sample surface (Meunier et al., 2008). Generally, rubber materials are assumed to be incompressible due to large bulk modulus (Treloar, 1975; Gent, 2012). Otherwise, volumetric test can be used to determine bulk modulus if rubber is compressible (Shahzad et al., 2015). Furthermore, it is also suggested to use rubber samples made from one batch due to the fact that the properties can vary significantly from different batches (Abaqus, 2011). After obtaining rubber properties, data can be fit to those material models, which can later be implemented into FE models to analyze hyperelastic structures.

In Abaqus, the finite element software, some of the hyperelastic material models are available under the isotropic assumption, including the Arruda-Boyce form, the Marlow form, the polynomial form, and the Van der Waals (Abaqus, 2011). However, other material models are also possible to be used by user subroutine UHYPER, where number of property values as well as the form of the strain energy function can be specified (Abaqus, 2011). Furthermore, Abaqus provides hyperelastic material evaluation by finding the optimized strain energy function from experimental data (stress-strain relations) (Abubakar et al., 2016) based on least-squares-fit procedure (Abaqus, 2011), which minimizes the relative error in stress. Additionally, Drucker stability (Romanov, 2001) is also checked during material evaluation to determine the strain range where the unstable behavior (Mishra & Gowda, 2015) occurs based on whether the incremental internal energy of a material increases or not (Abubakar et al., 2016).

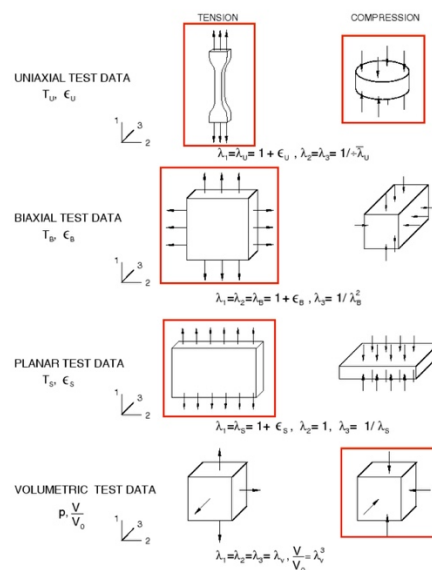


Figure 2.9 Schematic illustrations of deformation modes, where the commonly used testing methods are marked in red (Abaqus, 2011)

Experimental data from the following deformation modes are accepted by Abaqus (Abaqus, 2011):

- Uniaxial tension and compression
- Equibiaxial tension and compression
- Planar tension and compression (also known as pure shear)
- Volumetric tension and compression

These deformation modes and corresponding stretch ratio  $\lambda$  are shown in Fig 2.9, where  $\lambda_1$ ,  $\lambda_2$  and  $\lambda_3$  are principal stretches and the relation between stretch ratio  $\lambda$  and nominal strain  $\epsilon$  is illustrated.

If incompressible material is assumed, volumetric tests are not required and some equivalent deformation modes exist (Abaqus, 2011), including:

- Uniaxial tension  $\Leftrightarrow$  Equibiaxial compression
- Uniaxial compression  $\Leftrightarrow$  Equibiaxial tension
- Planar tension  $\Leftrightarrow$  Planar compression

In general, experiments should be performed for different deformation modes and should cover the range of strains used in the real applications (Abaqus, 2011).

In a nutshell, it is required by FEM to characterize rubber and model it as hyperelastic material. Some of the commonly used hyperelastic material models are implemented in Abaqus, for which material constants can be automatically obtained from experimental data by least-squares-fit procedure, where Drucker stability is also checked to ensure strain energy function always has a positive incremental internal energy. As a result, the hyperelastic material model of rubber can be implemented in FEM and simulation can be initiated.

## 2.4 Pressure measurement

Pressure measurement will be conducted to validate FE models. Pressure sensitive film (Prescale film<sup>®</sup>) has been widely used to measure the pressure between two contact areas in the field of biomechanical engineering. It was firstly introduced by Fukubayashi and Kurosawa (Fukubayashi & Kurosawa, 1980) to study the contact pressure distribution patterns in the knee and later applied by Brulotte *et al.* (Brulotte, Hubert, & Hojjati, 2012) to investigate the contact pressure distribution for the in-situ consolidation process. The accuracy of the pressure measurement is expected to be around  $\pm 10\%$  for visual analysis and around  $\pm 2\%$  for digital analysis when using digital scanners or microscopes (Brulotte et al., 2012).

Pressure sensitive film consists of an A film and a C film that are made of PET (polyethylene terephthalate) base when pressure range is below 50 MPa. As illustrated in Fig 2.10. a), A film is coated with a micro encapsulated color forming material and C film is coated with a color developing material. The two films should be placed together when measuring pressure. Once pressure is applied on the film, microcapsules are broken and the color forming material is released and reacts with the color developing material, forming magenta color. The color density depends on the true pressure distribution and their relation is provided as a color intensity chart shown in Fig 2.10. b). Based on the mechanism of color development, both of the extended (continuous) and momentary pressure (Fujifilm, n.d.) can be measured by the pressure sensitive film. The former requires 2 minutes of applying force up to its highest level and 2 minutes of holding at that level, and the latter requires 5 seconds of ramping up and 5 seconds of force holding. In addition, it is suggested to measure the pressure at a certain room conditions, where the temperatures should remain in the range from 20°C to 35°C and the humidity should stay from 35% to 80% (Fujifilm, n.d.).

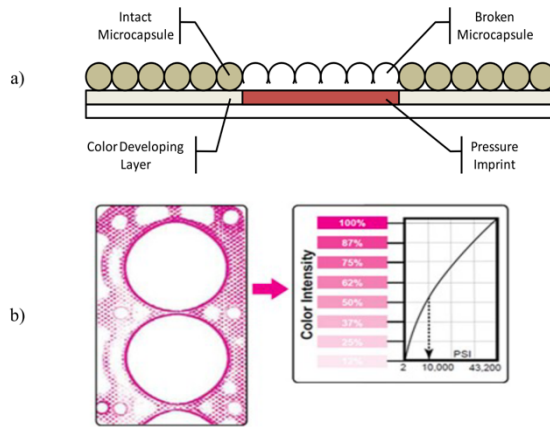


Figure 2.10 a) C film gets colored when microcapsules burst under pressure; b) The magnitude of applied pressure is determined using a color intensity chart (Sensor Products Inc., n.d.)

The color intensity chart has been often calibrated by researchers (Harris, Morberg, Bruce, & Walsh, 1999; Liggins, Hardie, & Finlay, 1994; Liggins, Stranart, Finlay, Rorabeck, & E.G.Little, 1992; Wang et al., 1995) since the pressure sensitive film is highly sensitive to room temperature and humidity. Pressure measurement should be performed immediately after the calibration in order to limit the fluctuations of temperature and humidity (Liggins et al., 1992). In order to obtain the relation between color density and pressure, pressure sensitive film is uniformly pressed at a known pressure. The stain image is then scanned by digital scanner (Fig 2.11 a) and can be transformed into grey-scale mode (256 grey levels) pixel by pixel (Harris et al., 1999), using image processing software. Hence, the averaged grey level is obtained at a known pressure. Liggins *et al.* (Liggins et al., 1994, 1992) calibrated the pressure sensitive film of super low pressure (LLW) type, which has a pressure range from 0.5 to 2.5 MPa. The calibration apparatus is shown in Fig 2.11 (b), including a 63.59 mm diameter base plate, 25.39 mm diameter calibration punch, ball bearing and a 15 kN load cell. The pressure sensitive film is put on top of the base plate and the stains are formed when the punch is press against the base-plate. Load control is applied with the load profile that is ramping up to full load in one minute, hold at that load for one minute, and ramping down to zero in one minute. Eleven different pressures uniformly distributed between 0.25 - 3 MPa are selected. Then, the calibration curve (color intensity chart) is fitted to the pressure/grey level data points, as shown in Fig 2.11 (c). Besides the mean values, coefficient of variation (COV) (Liggins et al., 1994) is calculated at each pressure level to check the degree of repeatability.

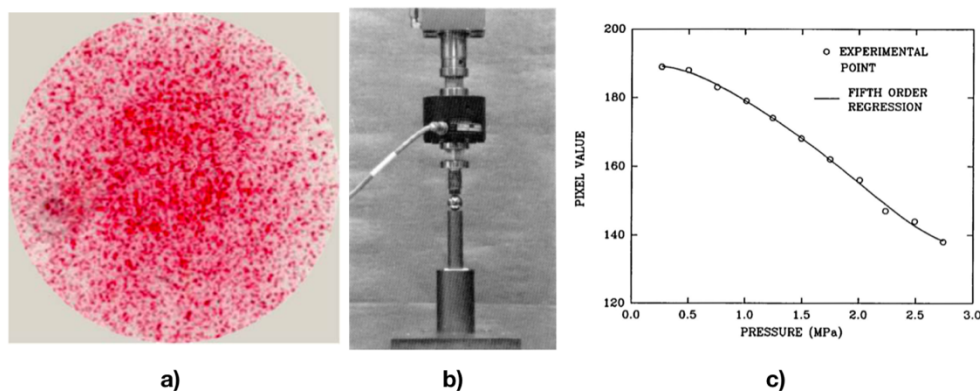


Figure 2.11 a). Scanned stain image obtained from uniform pressure, b). Pressure sensitive film calibration apparatus and c). calibration curve (Bachus, DeMarco, Judd, Horwitz, & Brodke, 2006; Liggins et al., 1992)

The contact pressure distribution has been investigated by Brulotte *et al.* (Brulotte et al., 2012) for the in-situ consolidation process. The intention is to measure the pressure under processing (370°C) between a flat mandrel and TP prepreg (APC-2/IM7) that is pressed by a

roller. However, this is prevented by the temperature and humidity limitation of the pressure sensitive film. Alternatively, another type of material is used such that a similar viscosity to molten PEEK can be achieved at around 50°C. The pressure measurement is shown in Fig 2.12. The prepreg was placed on top of the Prescale films. An infrared lamp is used to heat up the prepreg at 60°C. A compaction force was applied on the prepreg. Afterwards, the Prescale films are scanned by a digital microscopy. As a result, stain images are obtained and analyzed by a Matlab code developed by them (Brulotte et al., 2012). Fig 2.13 a) shows a stain image obtained from 10 kg provided by the compaction roller and Fig 2.13 b) shows a pressure distribution map of the cropped image with a crop position that is illustrated in a), which accurately describes the pressure distribution between the prepreg and the flat mandrel.

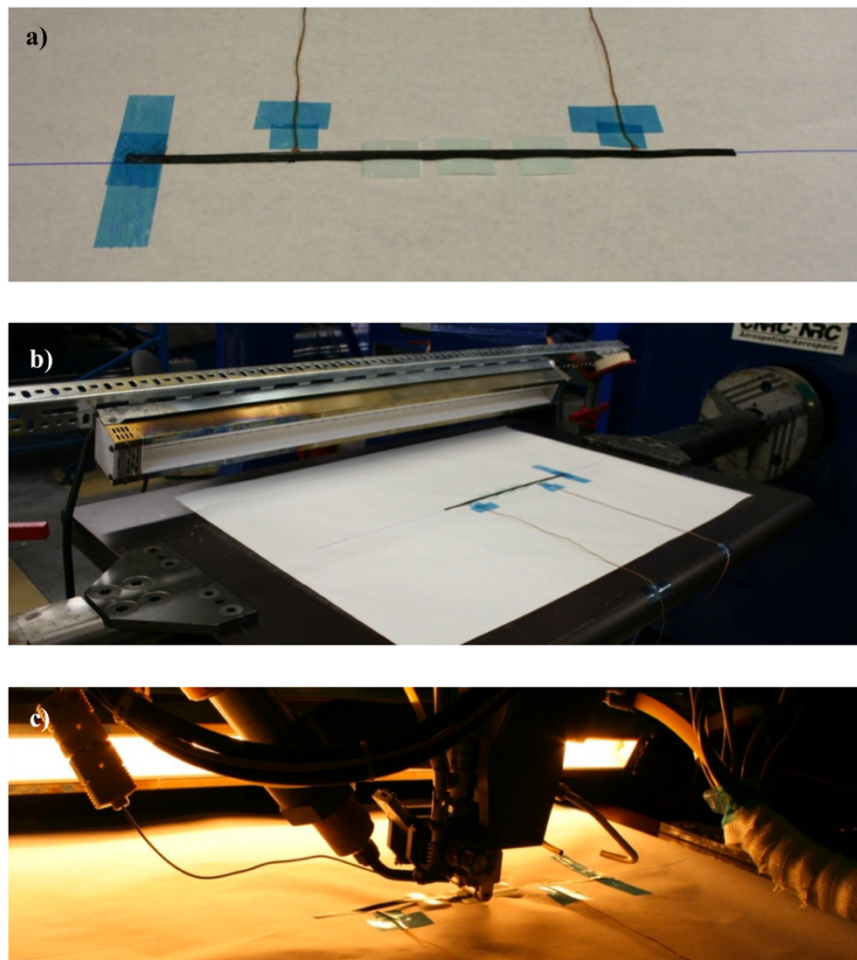


Figure 2.12. a). The prepreg is placed over samples of pressure sensitive film. b). Setup is heated using an infrared lamp. c). Placement machine performing a compaction pass over the pressure sensitive film (Brulotte et al., 2012)

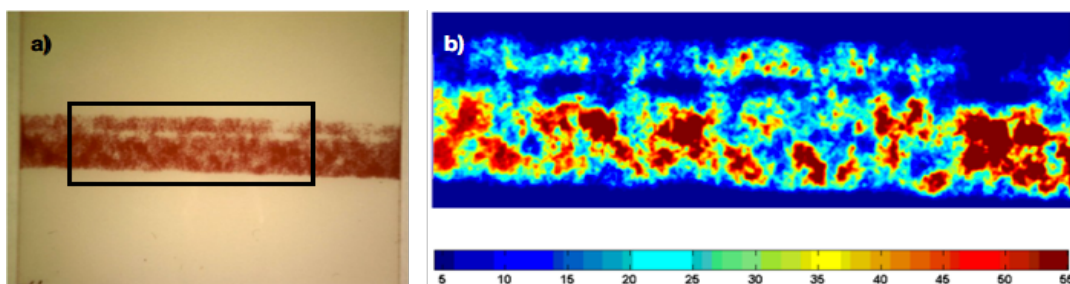


Figure 2.13. a). Untreated digital pressure imprint for 10 kg on compaction roller with a crop rectangular. b). Generated pressure map of the cropped image in MPa (Note: the darker red areas are saturated) (Brulotte et al., 2012)

In a word, pressure sensitive film can be used to measure the contact pressure to validate FE models. The film shows different color densities under different pressure levels. Therefore, pressure distribution map can be obtained from the stain image scanned by digital microscopes, using image processing software. However, it is recommended to use the pressure sensitive film at the temperature range of 20°C to 35°C, and the humidity range of 35% to 80%, which limits the application of measuring pressure at high temperature.

## 2.5 Conclusion

In-situ consolidation is a promising manufacturing technique for thermoplastic composites. However, its application is constrained by low quality and slow production rate. In order to improve the product quality, pressure plays a vital role in bonding but is obtained less interest than other parameters, such as temperature. Hence, several aspects regarding the pressure distribution in the contact area between rubber and mandrel are summarized as follows.

1. Bonding theories are presented to analytically explain the formation of the fusion bonding, including analytical models of intimate contact and autohesion. Pressure contribution to bond quality has received less attention than that of temperature, despite the fact that they are of equal importance for quality improvement. In fact, the role pressure played in bond quality cannot be neglected, especially in the theory of intimate contact. However, the influence of pressure is often skipped by assuming an averaged pressure, or setting a high value of pressure to ensure a sufficient degree of intimate contact. Therefore, this work is focused on the pressure prediction, which will be a necessary prerequisite to the further investigation of bonding theories.

2. Pressure distribution can be simulated using finite element method (FEM). However, mechanical simulation has received less interest than thermal simulations. The experimental validation of pressure distribution is rare in the existing literature. In addition, limited experimental work has been done for the material characterization of the selected rubber, so that the accuracy of the simulations is not guaranteed.

3. Material characterization of rubber is required as an input to the FE models. Rubber materials exhibit nonlinear elastic behavior. Strain energy functions, so called hyperelastic material models, are used to describe the constitutive behavior of rubber in different deformation modes. Some of the commonly used hyperelastic models are implemented in Abaqus, for which material constants can be automatically obtained from mechanical testing data by least-squares-fit procedure, where Drucker stability is checked to ensure that strain energy function always has a positive incremental internal energy.

4. In order to validate the FE model experimentally, pressure sensitive film (Prescale film) can be used to measure the pressure distribution between two contacted areas at ambient temperature, such as two rolling surfaces. The film shows different color densities under different pressure levels. Therefore, pressure distribution map can be obtained from the stain image scanned by digital microscopes, using image processing software. However, it is recommended to use the pressure sensitive film at the temperature range of 20°C to 35°C, and the humidity range of 35% to 80%, which limits the application of measuring pressure at high temperature.

## 2.6 Research questions

As mentioned before, the objectives are to predict the pressure distribution between rubber and mandrel in room temperature and to investigate the influences of the compaction force, rubber thickness and with/without pre-stretching force on the pressure distribution, followed by the rubber size optimization. Based on the literature study, research questions are raised to provide useful information to fulfill the research objectives. For each central question, several sub-questions are formulated to answer the central question. The research questions with their sub-questions are listed as follows.

1. The pressure simulation needs material properties as input data. To this end, rubber is characterized and modeled as a hyperelastic material. What the is hyperelastic material that most suits the selected type of rubber?
  - a). What kinds of experimental data are needed to form the hyperelastic material model?
  - b). Which hyperelastic material model to use and why?
2. Rolling process can be considered as a continuous contact problem between rubber-covered roller and mandrel. How to use FEM to simulate the pressure distribution for such a contact problem?
  - a). How to model a 3D rolling problem to a FE model? It model reduction needed?
  - b). How to simulate the pre-stretching process?
3. What can be learnt from the FEM results?
  - a). How does the compaction force affect the pressure distribution?
  - b). How does the rubber thickness affect the pressure distribution?
  - c). How is the pressure distribution affected by using pre-stretching force to the rubber or not? Is it suggested to use pre-stretching force?
  - d). What is the applicable range of pressure applied for the selected rubber? How to optimize rubber size? What should be considered when selecting the rubber dimension?
4. How to validate the FE model?
  - a). What variables in the FE models should be validated?
  - b). What kinds of experiments can be done to measure those variables?
  - c). Is there any limitation of the experimental methods?
  - d). What can be learnt from the experimental results?
  - e). Are the experimental results consistent with the conclusion made by FEM? To what extent can the FEM results be trusted?
5. What is the limitation of this work? Is there any recommendation for the future investigation?

The outline of this work is shown in Fig 2.14. In chapter 3, the properties of silicone rubber are obtained experimentally and modeled as a hyperelastic material, which is then used as inputs in the FE models. Chapter 4 describes the FE models that are used to simulate the pressure distribution in the contact area during the tape winding process. As a result, pressure distribution and strain field can be obtained as the output from FE models. In chapter 5, experiments are conducted to validate the FE models, where the pressure distribution and the strain field are measured by digital camera correlation (DIC) and pressure sensitive films, respectively. According to experimental validation, improvements are made to FE models if it is necessary. By comparing simulated results with experimental results, conclusions are drawn in chapter 6 to answer the research questions. Lastly, recommendations are made for future

work in chapter 7.

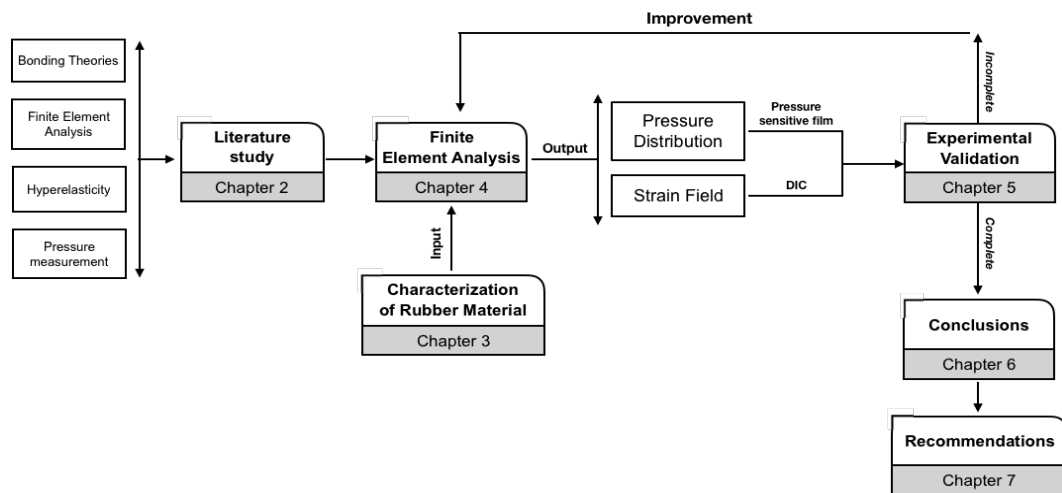


Figure 2.14 Thesis outline

# 3 Characterization of Rubber Material

In this chapter, rubber will be characterized by mechanical tests, including tensile, compressive and planar tension testing. Then, rubber is modeled as hyperelastic material based on experimental data. The material constants will be obtained by automatically fitting the testing data to existing hyperelastic material models in Abaqus. As a result, a most suited model will be selected and then implemented to FEA as inputs.

## 3.1 Rubber testing

The rubber used in this work is an unfilled silicone rubber produced by XIAMETER® (RTV-4136-M). In this section, mechanical tests will be illustrated to obtain rubber properties, including uniaxial tensile testing, compressive testing and planar tension testing. The sample manufacturing of each test is explained in Appendix 1. The mentioned three tests cover all deformation modes as required in Abaqus (Fig 2.9) except for volumetric test. However, volumetric test can be ignored due to the incompressible assumption (Treloar, 1975; Gent, 2012), as discussed in section 2.3. Only small rubber deformation is of interest since the rubber should remain in linear range during the winding process.

### 3.1.1 Tensile testing

The sample dimensions and experimental setup of tensile testing are based on ISO 37 (StandardISO. 37, 2011) and ASTM 412 (StandardASTM, 412, 2016). Sample dimension selection, test procedure, and results & discussion will be explained in this section.

#### *Sample dimension selection*

Ring samples are suggested in both ISO 37 (StandardISO. 37, 2011) and ASTM 412 (StandardASTM, 412, 2016). Compared to Dumb-bell samples, ring samples are easier to clamp by spindles (StandardASTM, 412, 2016). The sample dimensions of the rubber ring are recommended differently in those standards, as listed in table 3.1. In the end, dimensions are selected according to the thinnest rubber ring that will be used on the roller, in order to represent the actual application. The chosen dimensions are also included in table 3.1. It is slightly thicker and has larger inner diameter. On one hand, the ring thickness directly affects the non-uniform stress distribution over the cross section (StandardISO, 37, 2011) close to the spindles. The larger the thickness, the less uniformly the stress is distributed. However, it has negligible influence on the testing results if the displacements are measured between two spindles and the spindle diameter is small (10 mm) compared to their initial distance (95 mm). On the other hand, a larger inner diameter is chosen but it is still smaller than the largest inner diameter suggested in ASTM 412. In fact, a larger inner diameter increases the complexity of the experiment since the rubber ring would be less stable during testing. This is especially true under large tensile strain (> 100%) and tensile properties of rubber are often interesting within a large range of strain (up to 700%). However, the tensile strain won't exceed 50% for the rolling application of rubber ring and thus this deviation is not relevant for the material

characterization in this work.

Sample dimensions	ISO 37		ASTM 412		Chosen dimension
	Type A	Type B	Type1	Type2	
Thickness [mm]	4 ± 0.2	1 ± 0.1	1.0-3.3	1.0-3.3	4.84 ± 0.01
Inner diameter [mm]	44.6 ± 0.2	8 ± 0.1	50.0 ± 0.01	100.0 ± 0.02	67.0

*Table 3.1 Dimension comparison between ISO and ASTM standards, and the chosen dimensions (StandardISO, 37, 2011; StandardASTM, 412, 2016)*

The ring samples for tensile testing are the by-product from the manufacturing of thinnest rubber ring covers that will cover the aluminum roller. Those rubber ring covers are made by molding, which guarantees dimension stability and good surface finish as required by rolling application.

#### *Test procedure*

The experimental setup (StandardASTM, 412, 2016) is illustrated in Fig 3.1, where lubricated spindles are used to clamp the ring samples to eliminate the influence of friction. The initial distance between spindles is set so that rubber rings are slightly stretched at the pre-load of 5N. The testing is conducted at the rate of 500 mm/min. The tensile force is recorded by a load cell and spindle displacement is measured by extensometers until samples break.

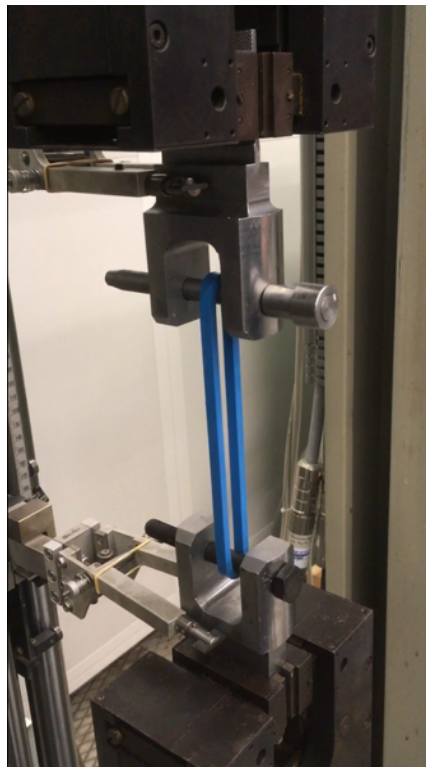


*Figure 3.1 Uniaxial tensile testing*

## Results & discussion

The nominal strain  $E_s$  and nominal stress  $S_e$  are calculated from the following equations (StandardISO\_37, 2011; StandardASTM, 412, 2016)

$$E_s = \frac{\pi d + 2L_s - C_i}{C_m} \quad 3.1$$

$$S_e = \frac{F_e}{2wt} \quad 3.2$$

where  $d$  is the spindle diameter (mm),  $L_s$  is the spindle distance (mm),  $C_i$  is the internal circumference of the ring sample (mm),  $C_m$  is the mean circumference of ring sample (mm),  $F_e$  is the force (N) recorded at the given elongation,  $w$  is the ring width (mm), and  $t$  is the ring thickness (mm).

The averaged stress-strain curve with the strain range from 0 - 80% is presented in Fig 3.2, with error bars. Averaged data is obtained by calculating the mean values of stress results of all four samples at a given strain, which is interpolated from original data (Box, 1978). Besides, standard deviation  $s$  and coefficient of variation  $C_v$  of stress values of all samples at a given strain are calculated by (Box, 1978)

$$s = \sqrt{\frac{1}{N-1} \sum_{i=1}^N (x_i - \bar{x})^2} \quad 3.3$$

$$c_v = \frac{s}{\bar{x}} \quad 3.4$$

where  $N$  is the number of samples,  $x_i$  is the stress value of sample  $i$  (MPa),  $\bar{x}$  is the averaged stress (MPa).

At the strain range of 0 - 80%, the maximum standard deviation of stress is 0.09 MPa and the maximum coefficient of variation is 5.70%. The strain range of 0-80% is chosen to cover the tensile deformation during rolling, typically not exceeding 50% tensile strain. Additionally, it should be noted that Sample No.3 out of the total 5 samples broke at small strain and thus is excluded in the data processing.

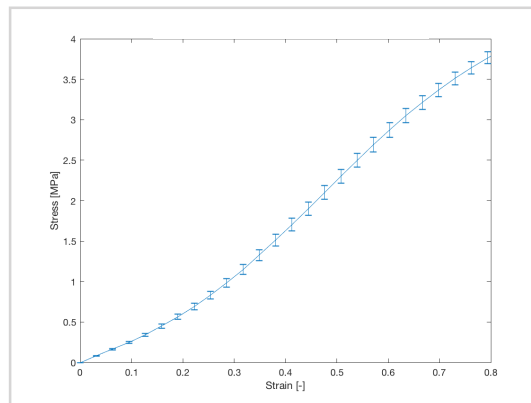


Figure 3.2 Experimental data (nominal stress and nominal strain) for Uniaxial tensile testing

### 3.1.2 Compressive testing

The sample dimensions and experimental setup of compressive testing are based on ASTM D575 (StandardASTM, D575, 2012). The test procedure and results & discussion will be explained in this section.

#### *Test procedure*

Cylindrical rubber samples are used for compressive testing based on ASTM D575 (StandardASTM, D575, 2012), with the diameter of 28 mm and the thickness of 12.5 mm. The test setup is shown in Fig 3.3, where rubber samples are compressed by a loading pin. A metal plate is used to provide a flat surface (the loading pin has a hole in the middle). The compressive test is conducted under three loading cycles at the loading rate of 12 mm/min according to ASTM D575 (StandardASTM, D575, 2012). The first two loading cycles are made to stabilize (StandardASTM, D575, 2012) stress-strain behavior and the third loading date is analyzed to obtain compressive curves. Lateral deformation should be enabled during testing since Abaqus requires simple compression as input in the material model. Therefore, silicone grease is used to lubricate (Abaqus, 2011) compressing plates to limit the influence of friction (Meunier et al., 2008), ensuring that the deformation state required in Abaqus (Fig 2.9) is achieved.

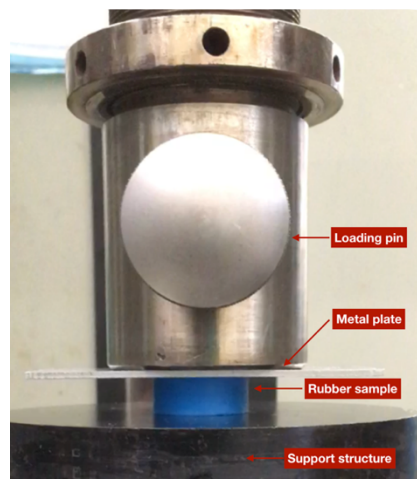


Figure 3.3 Uniaxial compressive testing

The range of compressive strain is determined such that the deformation is within the linear range. Fig 3.4 shows the stress-strain curves under three loading cycles up to 0.5 (left) and 0.35 (right) of compressive strain, respectively. The hysteresis effect in the plot of 0.5 strain indicates that rubber deformation is in plastic range when compressive strain reaches 0.5. On the other hand, the stress-strain curve of 0.35 strain shows good agreement in the three loading cycles, indicating the rubber deformation still remains in the linear range. As a result, compressive testing is decided to be performed up to 0.35 of the compressive strain.

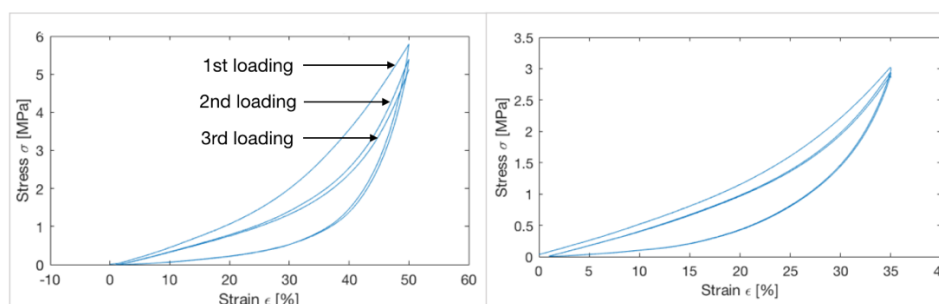


Figure 3.4 Nominal stress-nominal strain curve of compressive testing under three loading cycles up to different compressive strains

## Results & discussion

The nominal compressive strain  $E_s$  and nominal stress  $S_e$  are obtained from

$$E_s = \frac{l}{h} \tag{3.5}$$

$$S_e = \frac{4F}{\pi D^2} \tag{3.6}$$

where  $h$  is the sample thickness (mm),  $D$  is the sample diameter (mm),  $l$  is the compressive distance,  $F$  is the compressive force (N).

Six samples are tested and the averaged stress-strain curve is shown in Fig 3.5 with error bars. Note that the negative values indicate compressive stress and compressive strain. Averaged data, standard deviation (SD) and coefficient of variation (COV) are obtained in a similar way as explained in section 3.1.1. At the strain range from -0.34 to 0, the maximum standard deviation (SD) of stress is 0.10 MPa while the maximum coefficient of variation (COV) is 5.32%, which suggests good repeatability in this range.

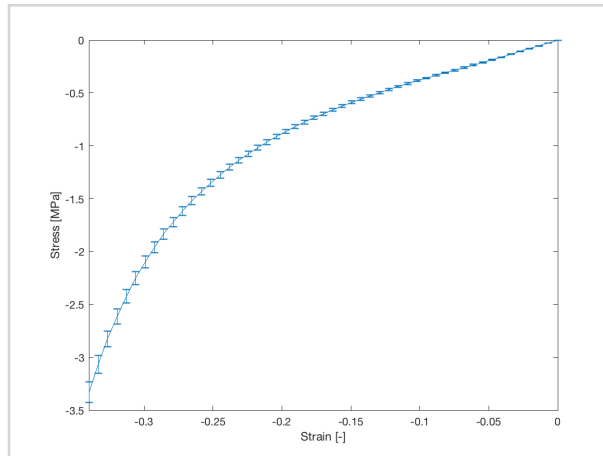


Figure 3.5 Experimental data (nominal strain and nominal stress) for Uniaxial compressive testing

### 3.1.3 Planar tension testing

Planar tension test is carried out according to literature (Meunier et al., 2008; Sasso et al., 2008) since there is not a testing standard yet. Test procedure and results & discussion will be explained in this section.

#### Test procedure

Rubber films bonded with metal strips are used to find the planar tension properties. The sample dimensions are determined by Shahzad *et al.*'s work (Meunier et al., 2008; Shahzad et al., 2015): length x width x thickness = 55 mm x 110 mm x 2 mm and the deformable length is 15 mm, which is marked in Fig 3.6. The aspect ratio between sample width and sample length is suggested to be within the range from 4 to 10 (Duncan, Maxwell, Crocker, & Hunt,

1999), so that the stress-strain curve is not affected by the length of grip separation.

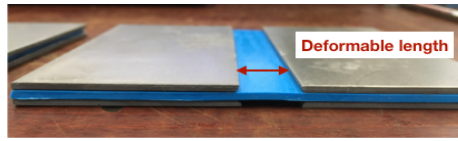


Figure 3.6 Gluing the metal plates to rubber film

The planar tension test is conducted based on Shahzad *et al.*'s work (Sasso *et al.*, 2008). As shown in Fig 3.7, pneumatic grips are used to clamp the sample and prevent slippage. In order to achieve rubber stabilization, 20 loading cycles (Shahzad *et al.*, 2015) are used at the rate of 100 mm/min. The maximum displacement in the test is determined by the maximum absolute value of shear strain. When applying the maximum compressive strain (0.35 based on Fig 3.5) to the FE model, the corresponding maximum absolute value of shear strain can be obtained, which is around 0.3. Hence, a slightly larger planar tensile strain is used than that of FE simulation. The corresponding maximum displacement is 11 mm.

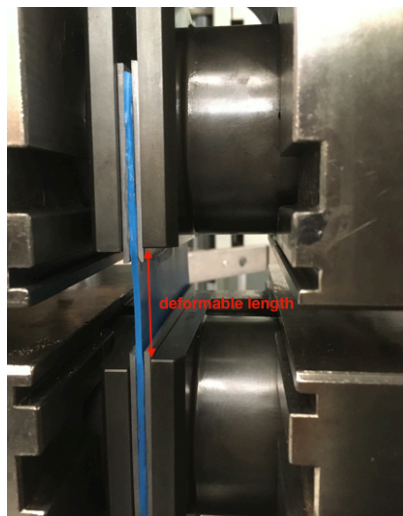


Figure 3.7 Planar tension testing

### Results & discussion

The nominal strain  $E_s$  and nominal stress  $S_e$  for the planar tension test are obtained from

$$E_s = \frac{l}{L_0} \tag{3.7}$$

$$S_e = \frac{F}{wt} \tag{3.8}$$

where  $L_0$  is the initial deformable length (mm),  $l$  is the clamp displacement (mm),  $F$  is the tensile force (N),  $w$  is the sample width (mm) and  $t$  is the rubber thickness (mm).

The stress-strain curves under 20 loading cycles for all five samples are similar. The 20 cycles of loading are applied twice to one sample with two different strain limits. The results are presented in Fig 3.8 (a). Firstly, the sample is stretched to 8 mm (blue curve), corresponding to 0.5 of the nominal strain. Then, the sample is stretched from 0 to 11 mm (red curve), corresponding to 0.7 of the nominal strain. Hysteresis effects are considerable between the 1st loading and the rest 19 loadings. This is because cracks are developed near the bond line (de-bonding) during the testing, which can be proved by the first stretching of the red curve at

the 0.5 of the nominal strain. It follows the path of the 20th cycle of the blue curve but its slope changes suddenly when it exceeds the first strain limit (at around 0.5). Hence, the result of the 20th loading cannot be used. As shown in Fig 3.8 (b) and (c), the 1st-loading and 20th-loading curves are averaged in a similar way discussed in the section 3.1.1. The real curve should be closer to the 1st stretching curve if de-bond doesn't occur.

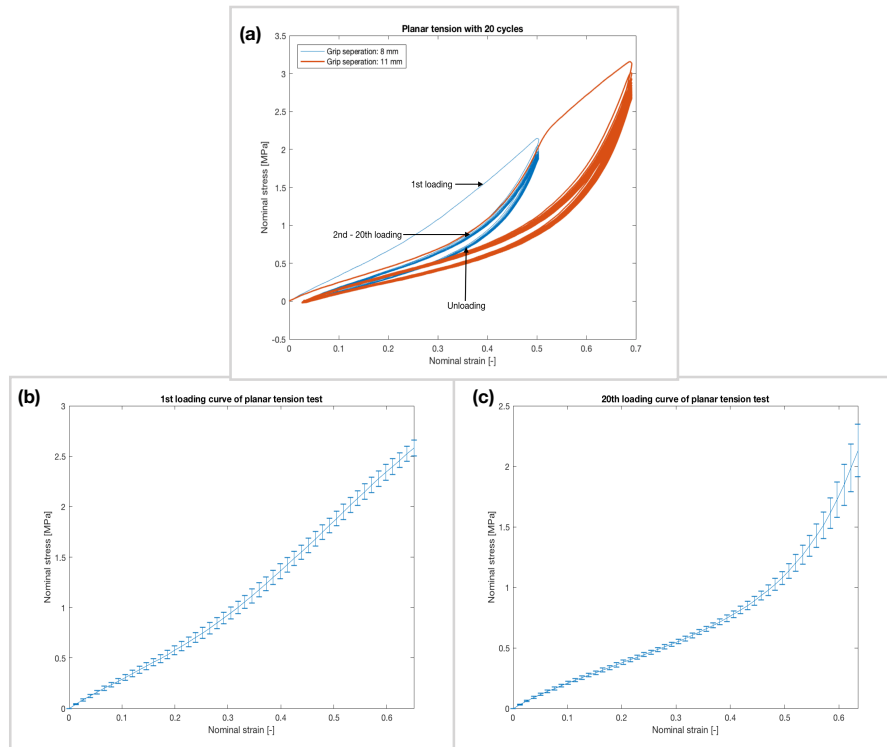


Figure 3.8 Experimental data for planar tension testing: a) under with 20 loadings for one sample up to two different strain limits: first 0.5 and then 0.8 of the nominal strains; b) under 1st-loading; c) under 20th-loading

The results of the 1st loading curve are questionable since the relation between planar tension test and tensile tests is inconsistent comparing to that in literature (Meunier et al., 2008).

Fig 3.9 (right) presents the experimental data of tensile and planar tension tests for another type of unfilled silicone rubber (RTV 141). The stress of the planar curve should be always larger than that of tensile testing under the same strain because planar tension test can be considered as a special tensile test under plane strain condition. However, the 1st and 20th loading curves of planar tension test are compared with the averaged curve of tensile test (Fig 3.2) in Fig 3.9 (left). The stress of the 1st loading planar curve is firstly larger but becomes smaller when nominal strain is increasing. The reason could be attributed to the inaccurate displacement measurement made by the tensile machine, which only measures the displacement of the grips instead of the displacement of unbonded rubber. In fact, more rubber is stretched when debonding occurs, leading to a larger undeformed length compared to the grip separation (15 mm). Hence, smaller nominal strain is obtained under the same force when debonding occurs (before 0.2 of the nominal strain).

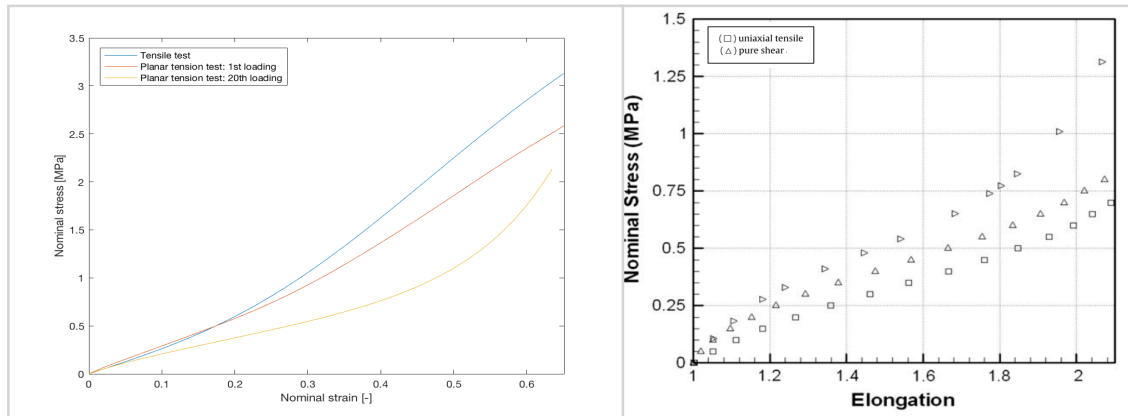


Figure 3.9 Comparison between planar tension test and tensile test in experiments (left) and in literature for the unfilled silicone rubber RTV 141 (right) (Meunier et al., 2008)

In conclusion, the results of planar tension test cannot be used as an input for modeling the hyperelastic material models since it has an inconsistent behavior comparing to literature due to experimental defects and inaccurate displacement measurement.

### 3.2 Material model selection

Commonly used hyperelastic material models are available in Abaqus, such as polynomial models and Ogden models. The material constants of those models can be obtained by experimental data (nominal stress- nominal strain data), including tensile and compressive tests. The results of planar tension test cannot be used as discussed before. Additionally, compression is the main deformation state in the rolling application and thus the planar tension test is not as important as compressive test. Nevertheless, a combination of tensile and compressive data is sufficient to characterize the hyperelastic material model as stated by Mishra *et al.* (Mishra & Gowda, 2015). The data fitting is automatically made in material evaluation in Abaqus. Note that the stress and strain data should be in the form of nominal stress and nominal strain as required by Abaqus (Abaqus, 2011).

The results of material evaluation are shown in Fig 3.10 and the material constants are listed in table 3.2. It can be seen that 3rd-order Ogden model fits best to the testing data and it is stable for the whole strain range. The maximum absolute error 0.22 MPa occurs when nominal strain is 0.5, indicating a good match between simulated and experimental results especially in compressive strain range. Hence, 3rd-order Ogden model is selected to describe the stress-strain relation of the silicone rubber. Furthermore, the stress-strain curves of planar test are calculated from the material constants for the 3rd-order Ogden model and compared to the experimental tensile and planar data, as presented in Fig 3.11. In this case, the relation between simulated planar curve and experimental tensile curve are consistent with the experimental results in literature (Meunier et al., 2008) (Fig 3.9 left), suggesting that calculated planar result is acceptable. In a word, 3rd-order Ogden model is used to describe the stress-strain behavior of the blue rubber.

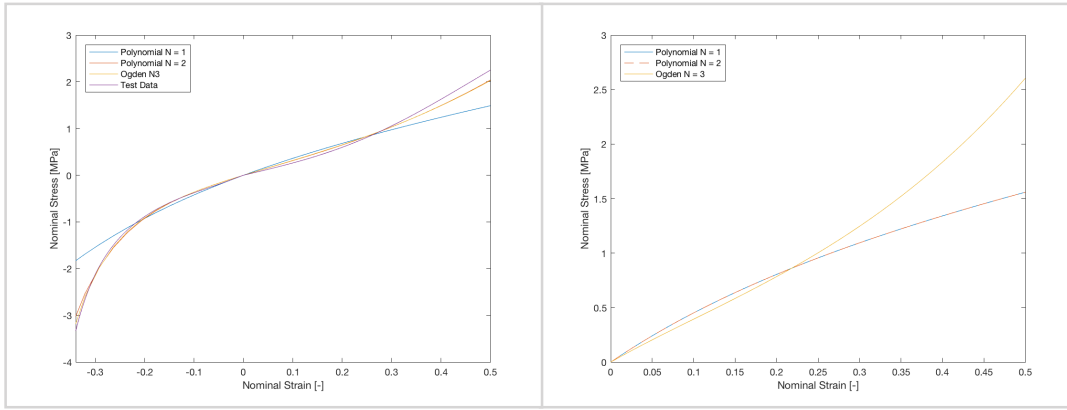


Figure 3.10 Fitting of the three hyperelastic models with uniaxial data (left) and corresponding planar data

	Polynomial N = 1	Polynomial N = 2	Ogden N = 3
Material constants	$C_{10} = 0.819398766$ $C_{01} = -0.172023460$	$C_{10} = 0.743041121$ $C_{20} = 0.415083264$ $C_{01} = -0.208145571$ $C_{02} = -0.376680049$	$\mu_1 = -3.88633842$ $\mu_2 = 4.84404723$ $\mu_3 = 0.123925126$ $\alpha_1 = 3.89882924$ $\alpha_2 = 4.19188540$ $\alpha_3 = -8.66527389$
Stable strain range	Uniaxial: -0.61 - 1.19 Biaxial: -0.32 - 0.61 Planar: -0.52 - 1.07	Uniaxial: -0.76 - 1.81 Biaxial: -0.40 - 1.05 Planar: all strain	Stable for all strain

Table 3.2 Material constants and stable limits of hyperelastic material models fitted on experimental data from all tests

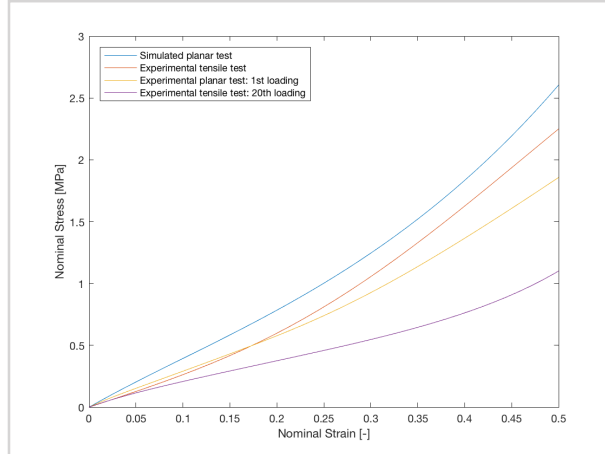


Figure 3.11 Comparison of the calculated planar curve and tensile curve

### 3.3 Conclusion

Rubber properties are required as an input of FEM. To this end, rubber is characterized by mechanical tests, including tensile, compressive and planar tension tests. According to those experimental data, rubber is modeled as a hyperelastic material. However, the results of planar tension test cannot be used due to the limitation of experimental setup. Therefore, only the experimental data of tensile and compressive test is implemented in Abaqus and it is found that the hyperelastic material model of 3rd-order Ogden function is stable in whole strain range and it can well describe the stress-strain behavior of rubber material.



# 4 Finite element analysis

In this chapter, finite element analysis is carried out to predict the contact area and the pressure distribution at the contact interface. There are three parts involved. In the first part, the FE models are described, considering the geometries, element types, load and boundary conditions (BCs). Then, numerical accuracy of the results is ensured by performing a mesh convergence study.

In the second part, model reduction is made to save computational time by using a two-dimensional (2D) static contact model to simulate the three-dimensional (3D) winding process based on several assumptions. Three FE models are investigated to confirm those assumptions, including a 2D static contact model, a 3D static contact model, and a 2D rolling model.

In the last part, several factors that influence the pressure distribution between rubber and mandrel will be discussed, including the compaction force applied to the roller, the rubber thickness, and whether a pre-stretching force in the rubber is used in the rubber or not. Then, a trade-off is made to optimize rubber dimension and the compaction force based on equipment limitations and the pressure requirements.

## 4.1 Model description

The model geometry is based on the experimental setup shown in Fig 1.2. A rubber-covered roller vertically presses on the rolling mandrel and it rotates along with the mandrel due to the friction, which will be further explained in the next chapter. The material properties of aluminum and rubber is required as an input to the FE model. The rubber is characterized as a hyperelastic material and the material constants have been obtained in the previous chapter, while Aluminum properties are available in previous studies (Aluminum Association, 1984).

Owing to material nonlinearity (hyperelastic material) and boundary nonlinearity (contact problem) (Abaqus, 2011), nonlinear analysis are performed in Abaqus/standard (implicit integration) (Wriggers, 2008) by using an incremental approach to split the history-dependent problem into small steps (time increments) (Abaqus, 2011). Generally, Abaqus/standard uses Newton-Raphson as a numerical algorithm to iterate the nonlinear equilibrium in each time increment (Abaqus, 2011). It is computationally expensive due to the fine mesh that is required to capture the deformation of the rubber and details of the pressure distribution at the contact interface. Hence, model reduction is required. The 3D Rolling process can be simplified to a 2D rolling process, which can be further reduced to a 2D static contact problem owing to relatively low rotating speed up to 100 mm/min (Stokes-Griffin & Compston, 2016) and thus the inertia effect can be ignored (Abaqus, 2011). Additionally, the static contact model can be further reduced by symmetry, which will be elaborated later in this section.

The present finite element analysis is performed in three stages. In the first stage, a two-dimensional (2D) static model is created based on plane strain condition. It models the static contact problem, where the roller is fitted along with a pre-stretched rubber and then presses the fixed mandrel. In the second stage, a three-dimensional (3D) static model is developed with similar loads and geometry to the 2D model, taking into account the pressure distribution in the out-of-plane direction. Lastly, the dynamic rolling process is modelled by adding an extra rolling step to the 2D static model mentioned before. As a result, an equivalent 2D static model can be simplified from a 3D dynamic rolling process. This equivalency is evaluated by two comparisons. The first comparison is made between 3D and 2D static models and the second one is between 2D static and 2D rolling models.

### 4.1.1 Two-dimensional static contact model

#### Geometry

The geometry is illustrated in Fig 4.1 (left) below, which represents the mid-plane of the experimental setup (Fig 1.2) based on plane strain condition (Logan, 2011) since the width of the contact area (z direction) is relatively large compared to its length (x direction) and the rubber thickness (y direction). The plane strain condition is a strain state where  $\epsilon_z$ ,  $\gamma_{xz}$  and  $\gamma_{yz}$  are assumed to be zero. As a result, the width (in z direction) will not affect the in-plane properties and thus 1 mm of width can be used. The unit of the compaction force can be considered as Newton per width (N/mm) since the compaction force should be increased linearly when increasing the width. The diameter is 70 mm for the roller and 140 mm for the mandrel, while rubber cover has various dimensions. Furthermore, this 2D model is simplified to the right half (Fig 4.1 right) due to its symmetry about yz plane, which will be further explained later.

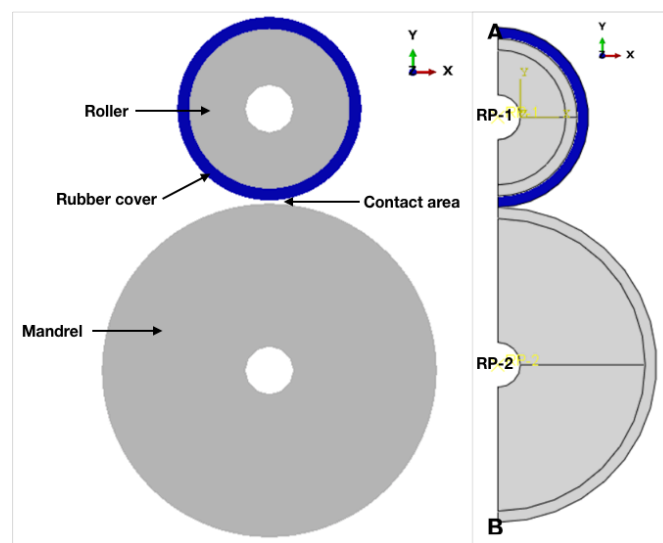


Figure 4.1 Two-dimensional FE model under plane strain condition: whole model (left) and half model (right)

#### Load & BCs

In the experimental setup, roller is vertically pressed by a pneumatic cylinder through a bearing system. In order to simulate this, a concentrated force of 8 N/mm is applied to the center of the roller (RP-1) and is coupled to the contact area between the bearing and the roller using kinematic coupling, which corresponds to the lower half of the roller's inner surface as highlighted in pink in Fig 4.2 (left). Only a quarter of the inner surface is used due to symmetric condition. The amplitude of the force is chosen based on compressive testing results (Fig 3.5), so that maximum vertical strain of rubber does not exceed the linear range (around 0.35 of the nominal strain). Additionally, the center of mandrel (RP-2) is fixed and coupled to entire inner surface of mandrel (highlighted in pink), as illustrated in Fig 4.2 (right). Since the geometry, force and BCs are all symmetric to yz plane, the 2D model can be further reduced to half of the geometry with symmetric boundary condition in the mid line ( $\overline{AB}$ ), as shown in Fig 4.1 (right). The symmetric BCs are listed as follows:

$$U1 = UR2 = UR3 = 0$$

4-1

where  $U_i$  refers to displacement in  $i$  direction (1, 2 and 3 direction correspond to x, y and z direction), and  $UR_i$  refers to the rotation about  $i$  direction.

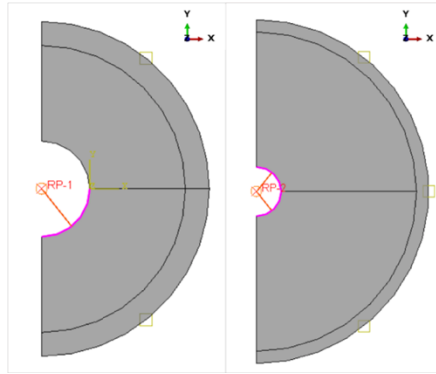


Figure 4.2 Coupling in roller (left) and mandrel (right) under symmetric condition

### Interactions

The term *Contact pairs* is used to describe the interaction between two separate surfaces (Abaqus, 2011). There are two contact interactions involved: Int-1 (between roller and rubber), and Int-2 (between rubber and mandrel) as shown in Fig 4.3. A contact interaction requires a master and a slave surface to be defined. In this case, the surfaces of the roller and the mandrel are considered as master surface as listed in table 4.1 since the roller and the mandrel are stiffer than the rubber ring (Abaqus, 2011). Detailed setup is included in Appendix 2.1.

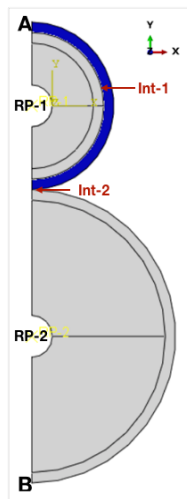


Figure 4.3 2D FE model with two interactions: Int-1 and Int-2

	Int-1	Int-2
Master surface	Roller's outer surface $\widehat{C_{ro}D_{ro}}$	Mandrel's outer surface $\widehat{AE}$
Slave surface	Rubber's inner surface $\widehat{C_{ru}D_{ru}}$	Rubber's outer surface $\widehat{EB}$

Table 4.1 Master surface and slave surface in the interaction setting, where *ro* stands for roller and *ru* for rubber

### Steps

There are four steps in the 2D model besides the initial step (default), including stretching, roller moving, waiting and pressing, as illustrated in Fig 4.4. General static step type is used to analyze the static problem, which is applicable to all four steps. Further explanation is made

in Appendix 2.1. All forces, BCs and interactions are summarized in table 4.2, where the global and cylindrical coordinates are marked in Fig 4.4 (left most)<sup>1-2</sup>. Then, interaction Int-1 is activated in the third step. In the last step, concentrated force is applied to RP-1 and interaction Int-2 is activated<sup>3</sup>. In addition, attention should be paid to the distance between rubber and mandrel ( $\overline{EF}$ ), which is set according to the results at the end of the step 3, since the thickness of the stretched rubber is unknown after stretching.

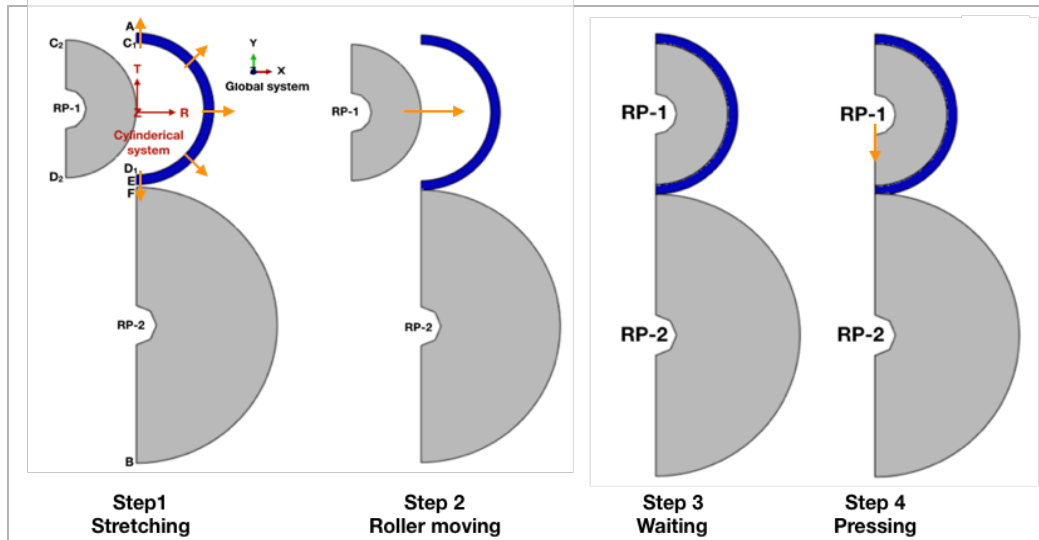


Figure 4.4 Step explanation for 2D static model

	Content	Regin	Constraints	Coordinate system		Content	Initial Step	Step 1	Step 2	Step 3	Step 4
Proce	A concentrated force to press roller	RP-1	F	Global	Proce	A concentrated force to press roller		Stretching	Roller moving	Waiting	Pressing
Boundary Conditions	BC1	Fix mandrel	RP-2	$U1 = U2 = UR3 = 0$	Global	BC1	Fix mandrel	Created	Propagated	Propagated	Propagated
	BC2	Stretching rubber	Rubber's inner surface ( $\widehat{C_1D_1}$ )	$U1 = 1.5$	Cylindrical	BC2	Stretching rubber	Created	Propagated	Inactive	Inactive
	BC3	Symmetric conditions for rubber and mandrel	Mid-line of Rubber and roller ( $\widehat{AC_1}, \widehat{D_1E}, \widehat{FB}$ )	$U1 = UR3 = 0$	Global	BC3	Symmetric conditions for rubber and mandrel	Created	Propagated	Propagated	Propagated
	BC4	Moving roller	Entire roller	$U1 = 35$	Global	BC4	Moving roller		Created	Inactive	Inactive
	BC5	Roller Y constrain	Entire roller	$U2 = 0$	Global	BC5	Roller Y constrain		Created	Propagated	Inactive
	BC6	Roller constrain in pressing	RP-1	$U1 = 35, UR3 = 0$	Global	BC6	Roller constrain in pressing			Created	Propagated
	BC7	Symmetric conditions for roller after moving	Mid-line of roller ( $\widehat{CD}, RP-1$ )	$U1 = 35, U2 = 0$	Global	BC7	Symmetric conditions for roller after moving			Created	Propagated
Interactions	Int-1	Interaction of roller and rubber	Between $\widehat{C_1D_1}$ and $\widehat{C_1D_1}$	/	Int-1	Interaction of roller and rubber				Created	Propagated
	Int-2	Interaction of rubber and mandrel	Between $\widehat{AE}$ and $\widehat{FB}$	/	Int-2	Interaction of rubber and mandrel					Created

Table 4.2 Summary of loads, BCs and interactions and their actives in each step

### Mesh refinement

Accuracy is of great importance to finite element analysis. Therefore, mesh refinement is made to improve the accuracy of FE results, keeping the computational time at an optimum. This is done by decreasing the element size, increasing the order of polynomial approximation of the elements (element's order) (Kikuchi N. , 1986), and using full integration instead of

<sup>1</sup> Note that the center of the cylindrical coordinate is concentric with the center of the rubber ring. In the stretching step, the rubber ring is stretched (BC2) by increasing the radius of its inner surface from 33.5 to 35 mm.

<sup>2</sup> It is not allowed to use different coordinate systems in adjoin regions. Hence, BC of pt  $C_1$ , pt  $D_1$  and art along  $\widehat{C_1D_1}$  except for pt  $C_1$ , pt  $D_1$  should be defined separately, in different coordinates, *i.e.* global coordinate for the first two while cylindrical coordinate for the last one. In the second step, the roller is moved (BC4) so that rubber ring fits along the roller.

<sup>3</sup> Int-2 cannot be activated in step 3 because rubber and mandrel might be not touching.

reduced integration. During the mesh refinement procedure, an exponential rate of convergence can be achieved (Szabo, 1984). A converged mesh size is achieved as a result of the mesh refinement.

The mesh strategy is shown in Fig 4.5. Quadrilateral elements are used in the contact area, including the rubber ring and the regions of the roller and the mandrel that are close to the outer surfaces, since it can provide accurate results at lower cost when compared to triangular elements (Abaqus, 2011). Instead, triangular elements are used in the inner regions of roller and mandrel, which are less important compared to the contact area. As a result, both the roller and mandrel are split by a concentric circle into two regions for different element types and mesh strategies: the outer area and inner area. Triangular element with reduced integration (CPE3R) is used in the inner part of roller and mandrel for the bias mesh with larger biased ratio compared to quadrilateral element, where R stands for reduced integration and PE refers to plane strain element to plane strain condition (Abaqus, 2011). On the other hands, quadrilateral element (CPE4R) are used in the outer part of roller and mandrel for more accurate results.

Hybrid element is often used for incompressible or nearly incompressible materials (Abaqus, 2011). Based on the hyperelastic theory, small displacement can lead to large change in stress and thus pure displacement-based solution may have large numerical error due to its high sensitivity. As a result, stress is treated as an independently interpolated basic solution variable in hybrid element, coupled to the displacement solution according to the constitutive theory and the compatibility condition (Abaqus, 2011). Therefore, 4-node bilinear plane strain quadrilateral element (CPE4RH) is used in rubber ring, where H refers to hybrid formulation.

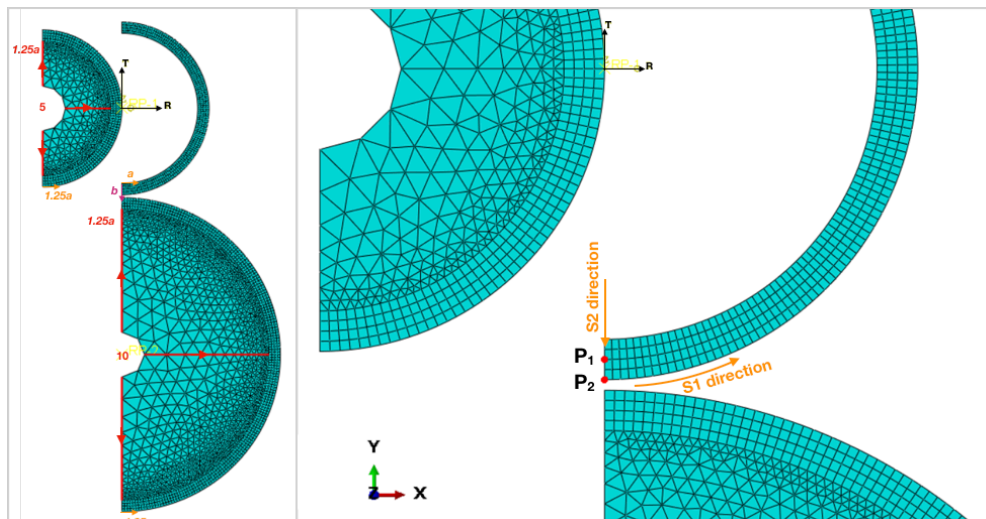


Figure 4.5 Mesh strategy: bias direction (left) and results locations (right), where mesh size ( $a$ ) and element number  $b$  are shown on the left side

Rubber has a uniform mesh while both the roller and the mandrel have the similar mesh strategy: uniform mesh in the outer part while biased mesh in the inner part. The direction of bias mesh is shown in Fig 4.5 (left). The mesh sizes are summed up in table 4.3, where  $a$  and  $b$  are constants. When two surfaces are in contact, the slave surface should have finer mesh than master surface. Accordingly, the rubber ring is meshed finer than that of outer surfaces of roller and mandrel. The ratio of element size between slave surface and master surface is kept constant, *i.e.* rubber has the element size of  $a$  mm and thus that of roller and mandrel is  $1.25a$  along the outer surfaces. The mesh size along the inner surfaces of roller and mandrel are also fixed to 5 and 10 mm, respectively.

Mesh strategy	Rubber	Mesh strategy	Roller	Mandrel
Mesh size [mm] in the circumferential direction (uniform)	$a$	Mesh size [mm] in the outer area (uniform)	$1.25a$	$1.25a$
Mesh size [mm] in the radial direction (uniform)	$b$	Mesh size [mm] in the inner area (bias)	$1.25a <- 5$	$1.25a <- 10$
		Mesh size [mm] in the inner surface (uniform)	5	10

Table 4.3 Mesh sizes for 2D model: rubber, roller and mandrel

As mentioned before, hybrid formation element is used to describe stress-strain behavior of rubber, where the stress and strain are treated independently and coupled together based on the constitutive theory and the compatibility condition (Abaqus, 2011). As a result, both of the strain and pressure distribution in the contact area between rubber and mandrel will be obtained from FEM. Therefore, strain and contact pressure (CPRESS) are compared under various mesh sizes for mesh refinement. The mesh sizes are changed in circumferential direction (S1 direction) and radial direction (S2 direction), separately. The compared values are the logarithmic strain in vertical direction (LE22) at  $P_1$  and contact pressure (CPRESS) at  $P_2$ , where  $P_1$  and  $P_2$  are shown in Fig 4.5 (right). The results are shown in Fig 4.6 – 4.7. It can be concluded that both of CPRESS and LE22 are converged when mesh size is smaller than 1 mm in S1 direction and 0.5 in S2 direction. The errors of the selected mesh sizes are less than 1.5% for all four cases, compared to results from the smallest mesh size. Furthermore,

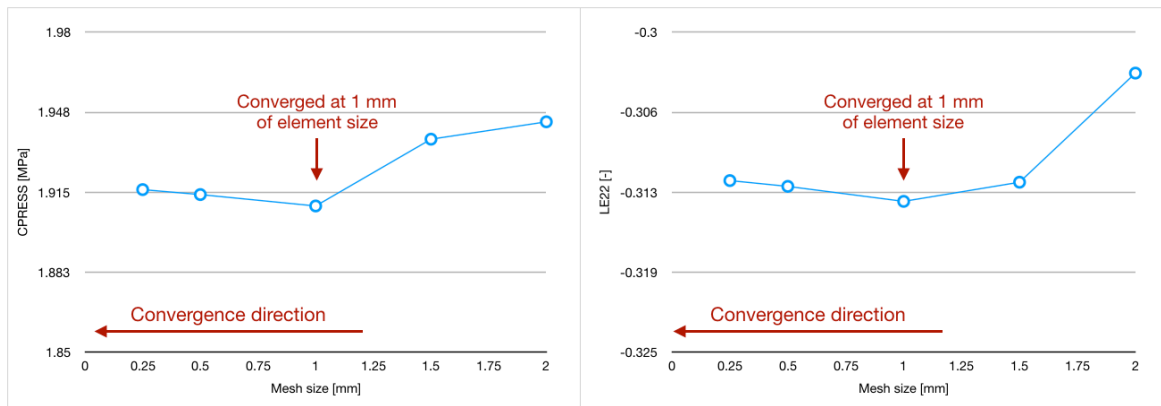


Figure 4.6 Mesh refinement in circumferential direction (S1 direction)

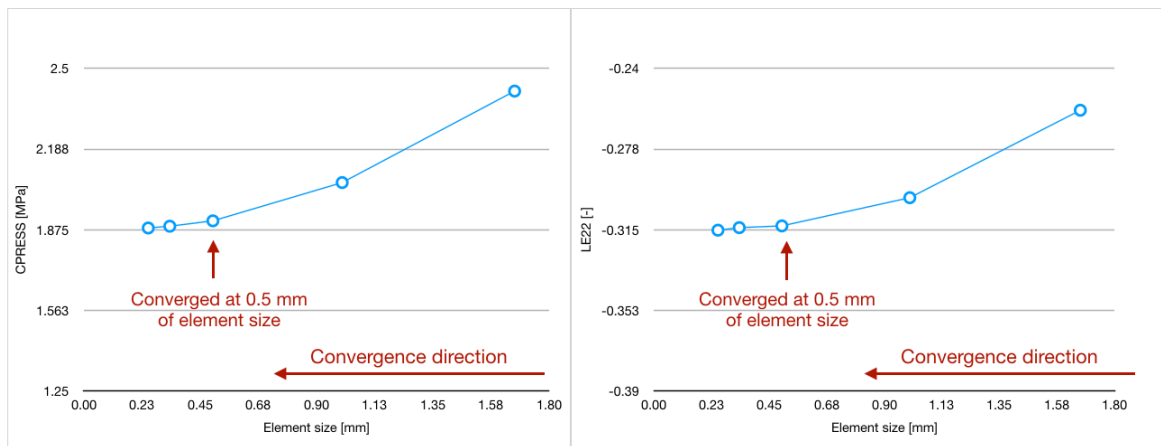


Figure 4.7 Mesh refinement in radial direction (S2 direction)

*The influence of full integrated element and higher order element*

Besides decreasing the mesh size, higher order element or fully integration can also be used for better accuracy. For nodal quantitative variables, such as displacement, equilibrium equations are solved at the nodes of each element (Abaqus, 2011). At the other locations of the element, results are interpolated based on the nodal values. The order of interpolation is decided by the number of nodes in the element. As shown in Fig 4.8, four nodes are used at the corners of the element for first-order interpolation (first order element / linear elements) while eight nodes are used for second-order interpolation (second order element / quadratic elements). In addition to nodal variables, some variables are integrated at the integration point of the element by Gaussian quadrature, such as Logarithmic strain and stress (Abaqus, 2011). At each element, reduced integrated element has one integration point at the element center while fully integrated element has four integration points as illustrated in Fig 4.8. Whether using full integration or reduced integration for higher accuracy mainly depends on the nature of the problem (Abaqus, 2011). Therefore, two comparisons are made between full & reduced integration and first order & second order elements under the same amount of force and same mesh strategy S11-S205 as concluded, where S11 refers to 1 mm of mesh size along S1 direction and S205 means the 0.5mm of the element sizes in S2 direction.

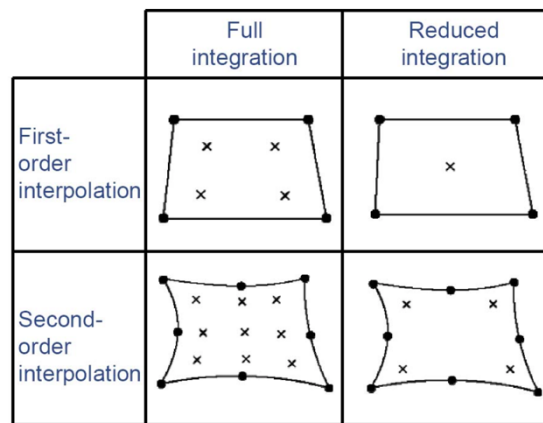


Figure 4.8 Explanations of 2D element: Full/reduced integration and first/second-order interpolation (Zienkiewicz, 2005)

Reduced vs. Full integration

Comparison is made between reduced and fully integrated linear elements using the same amount of force and the same mesh strategy S11-S205. In Abaqus, radial stress (S11) and radial logarithmic strain (LE11) are calculated at the integration points of each element (Abaqus, 2011). Hence, the results of S11 and LE11 at the integration points are compared. There are four integration points in fully integrated element and thus S11 and LE11 are obtained from each integration point, from which an averaged value at the element center is interpolated and compared with that of reduced integration element. Fig 4.9 plots the results calculated at the center of selected elements in cylindrical coordinate, where the origin is at the center of rubber ring as shown in Fig 4.10. The selected elements for S11 and LE11 are marked in red in Fig 4.10, separately. It can be concluded that the accuracy is comparable for LE11 while higher accuracy is achieved by using reduced integrated linear element for S11. Therefore, fully integrated element type is used.

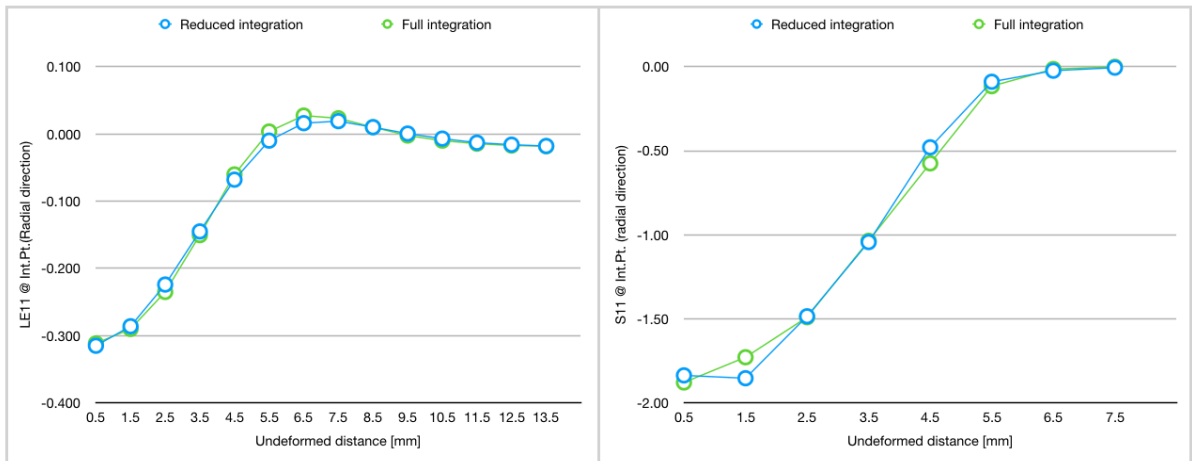


Figure 4.9 LE11 and S11 at the element center (cylindrical coordinate)

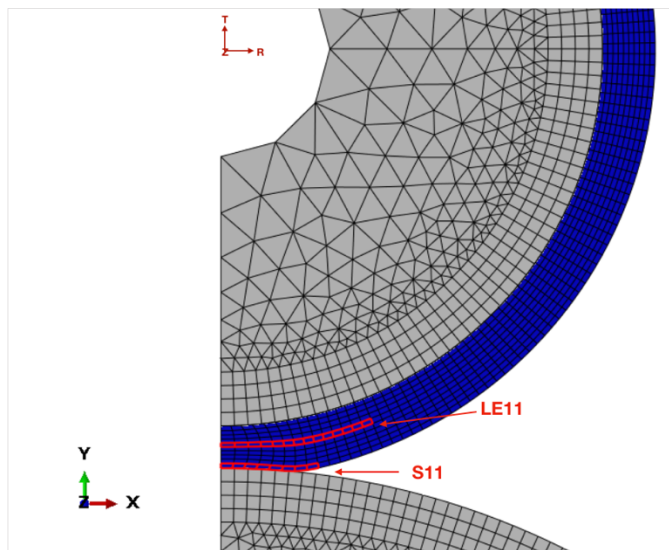


Figure 4.10 Selection elements for LE11 and S11

First order vs. second order element

Comparison are also made between linear and quadratic elements using the same amount of force and same mesh strategy S11-S205 with reduced integration. The results are shown in Fig 4.11, where quadratic element causes extra distortion in the marked area due to extra freedom in the middle of the edge. Hence, linear elements are preferred, which will be emphasized again in the mesh refinement part for 3D model.

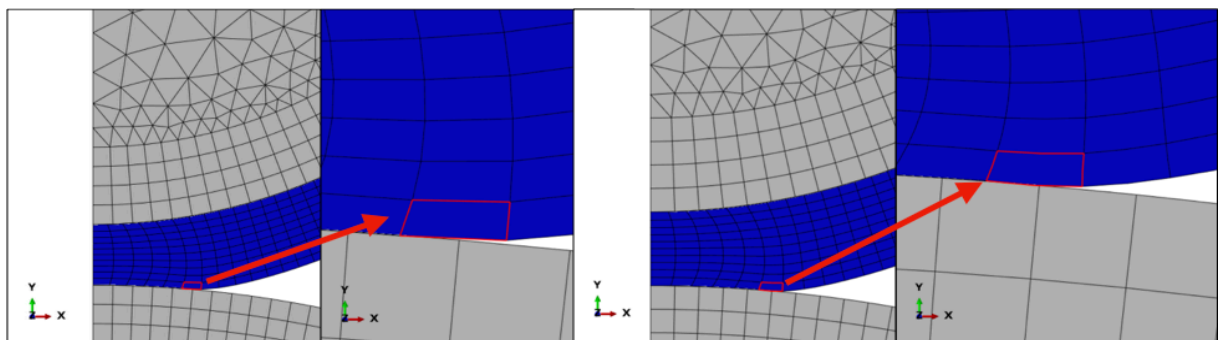


Figure 4.11 Deformation comparison between linear and quadratic element

## Conclusion

The mesh strategy is finalized by comparing vertical logarithmic strain (LE22) at  $P_1$  and contact pressure (CPRESS) at  $P_2$ , where two points are shown in Fig 4.5. As a result, linear element with full integration is used with the mesh size of S11-S205 (1mm in circumferential direction and 0.5 mm in radial direction).

### 4.1.2 Three-dimensional static contact model.

#### Geometry

Three-dimensional static contact model has a similar geometry to 2D model, as illustrated in Fig 4.12 (left). Only a quarter of the entire structure is considered due to the symmetry about yz and xy planes. Hence, half of the width is used, which is 25 mm for the roller and the mandrel, and 23 mm for the rubber ring. In addition, rubber ring has smaller width than roller and mandrel due to the fact that rubber ring deforms towards the out-of-plane direction (S3) during compression, which should be within the outer surfaces of roller/mandrel, as indicated in Fig 4.12 (right).

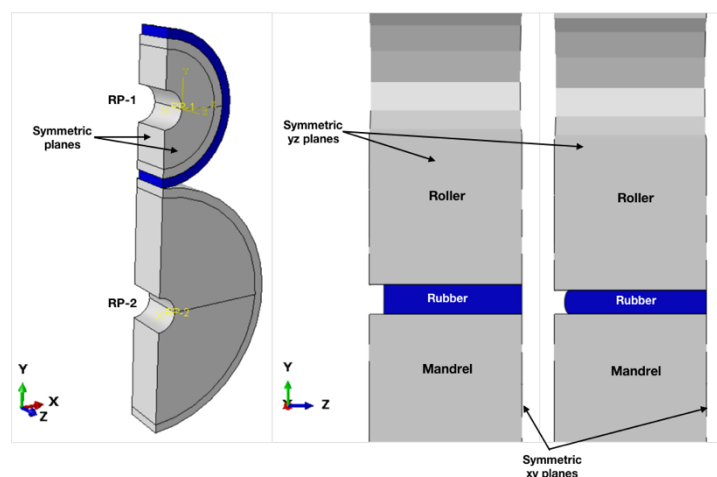


Figure 4.12 3D FE model with symmetric conditions about xy and yz planes (left) and the side view of 3D model: before (middle) and after pressing (right)

#### Load & BCs

A concentrated force of 184 N is applied at RP-1 (Fig 4.12 left) and its amplitude is calculated from multiplying the force per unit width in the 2-D model with the width of the 3-D model ( $8 \text{ N/mm} \cdot 23 \text{ mm} = 184 \text{ N}$ ). The corresponding force in the full model is thus to be four times to the one used in 3D model:  $184 \text{ N} \cdot 4 = 736 \text{ N}$  due to two symmetric planes. The coupling setups are similar to that of 2D model. In case of BCs, plane strain condition is removed since a 3D geometry is considered. Symmetric conditions are still applicable to all points in the symmetric planes. As can be seen in Fig 4.12, there are two kinds of plane symmetries involved: symmetry about the yz plane and the xy plane. The boundary conditions are summarized in table 4.4.

Symmetric plane	Boundary conditions
yz	$U1 = UR2 = UR3 = 0$
xy	$U3 = UR1 = UR2 = 0$

Table 4.4 Boundary conditions of different symmetric planes

*Interactions.* Interactions are exactly the same as that in the 2D static model.

### Steps

Similar steps are shown in Fig 4.13, where roller is moving along the z axis instead of x axis. Detailed information is included in Appendix 2.2.

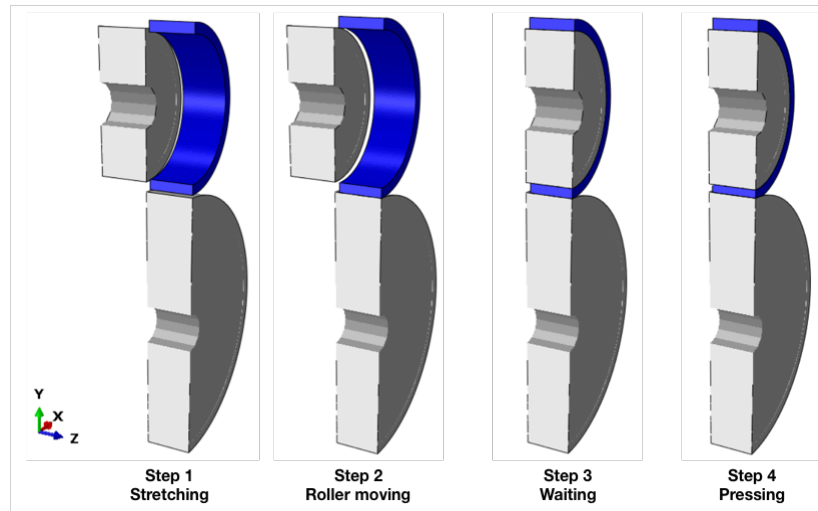


Figure 4.13 Step explanation of 3D model

### Mesh refinement

The meshing strategy is shown in Fig 4.14 (left), which is parallel to that of 2D model as well, except that quadrilateral elements are replaced with hexahedrals (C3D8) while triangle elements are replaced with tetrahedrals (C3D4) and C3D8H is used in the rubber ring.

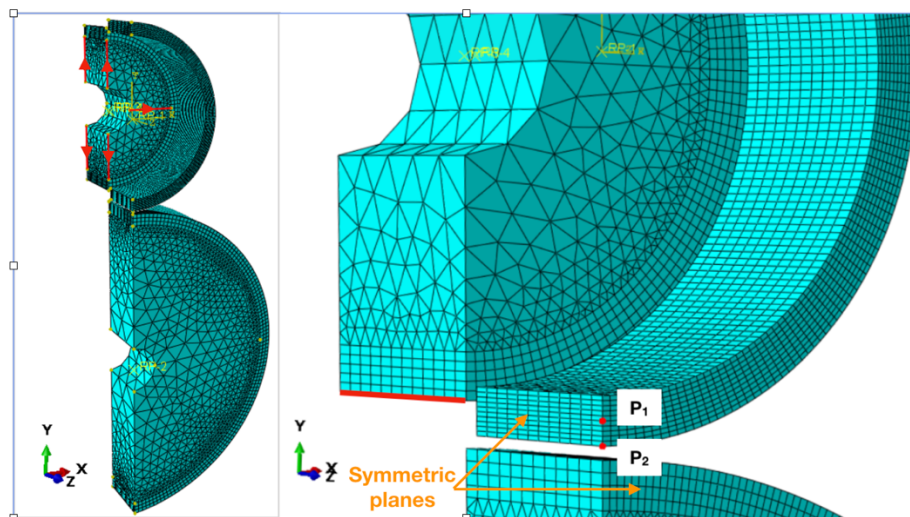


Figure 4.14 Mesh strategy: bias direction (left) and results locations (right)

As illustrated in Fig 4.14 (right), the logarithmic strain in vertical direction (LE22) at  $P_1$  and contact pressure (CPRESS) at  $P_2$  are compared under various mesh sizes for the in-plane mesh refinement. However, the distributions of vertical stress (S22), out-of-plane stress (S33), vertical logarithmic strain (LE22), out-of-plane logarithmic strain (LE33) and contact pressure (CPRESS) along the contact line (marked in red) are compared separately for mesh refinement in the out-of-plane direction.

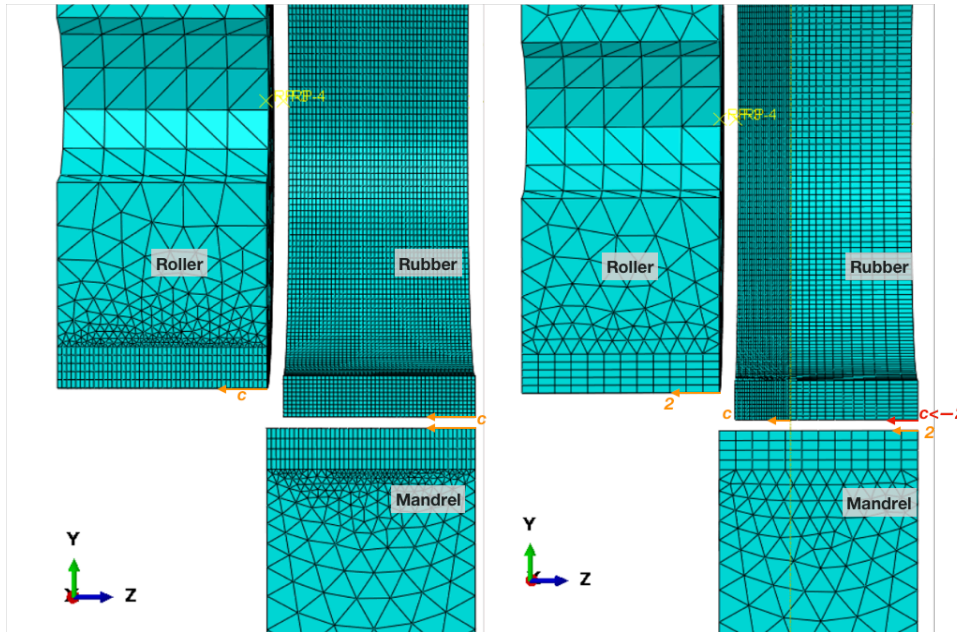


Figure 4.15 Mesh strategy in the out-of-plane direction: uniform mesh (left) and uniform + biased mesh

Mesh strategy		Rubber	Roller	Mandrel
Mesh size [mm] in the out-of-plane direction	Uniform mesh	c	c	c
	Uniform + biased mesh	Left 1/3 part is uniform: c Right 2/3 part is biased: c -> 1	1	1

Table 4.5 Mesh sizes for 3D model: rubber, roller and mandrel

The in-plane mesh strategies are similar to that of the 2D (table 4.3) model while two meshing strategies are used in the out-of-plane direction (Fig 4.15): uniform mesh and uniform + biased mesh, as summed up in table 4.5, where  $c$  the mesh size in  $z$  direction. Fig 4.16 plots the comparisons of S22, S33, LE22, LE33 and CPRESS between the uniform mesh and uniform + bias mesh when  $c = 0.5$  mm. They have almost the same output but the latter saves great amount of computational effort. As a result, uniformed + biased mesh is used when mesh size is smaller than 1.4 mm. For convinces, the uniform + biased mesh uses its equivalent uniform element size, *i.e.* Fig 4.15 (left) use 0.5 mm in the left 1/3 part, which is equivalent to the uniform mesh with  $c = 0.5$  mm (Fig 4.15 right).

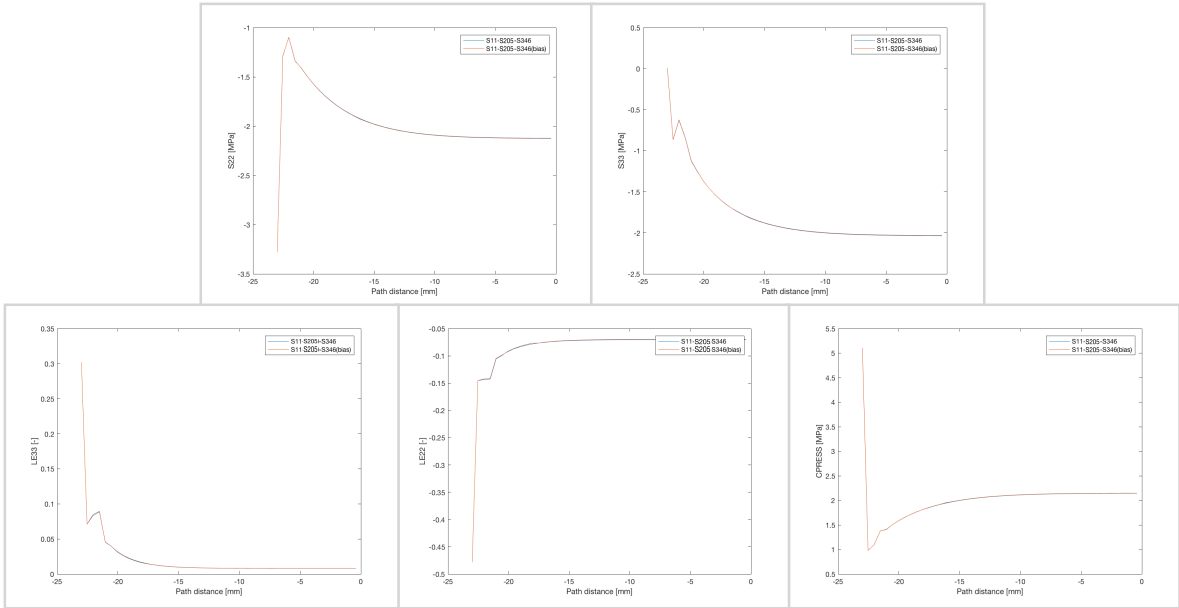


Figure 4.16 Comparisons of S22, S33, LE22, LE33 and CPRESS between a uniform mesh and a uniform + bias mesh when  $c = 0.5 \text{ mm}$

Results of mesh refinement in circumferential direction (S1 direction) and radial direction (S2 direction) are plotted in Fig 4.17 - 18, separately. Similar conclusions can be drawn that CPRESS and LE22 are converged when mesh size is smaller than 1 mm in S1 direction and 0.5 mm in S2 direction.

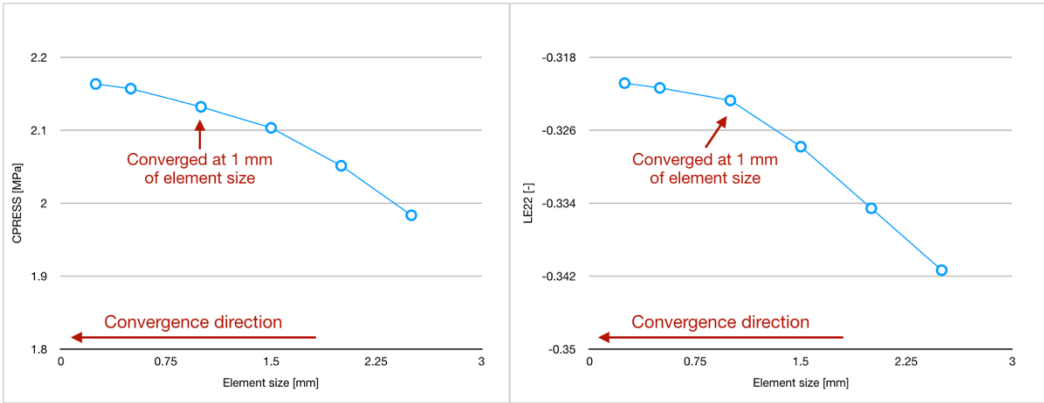


Figure 4.17 Mesh refinement in circumferential direction (S1 direction)

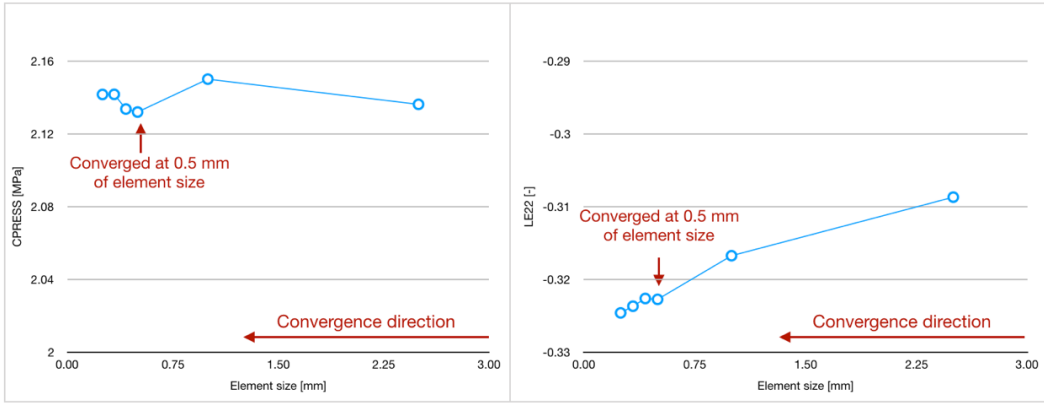


Figure 4.18 Mesh refinement in radial direction (S2 direction)

Regarding the mesh refinement in the out-of-plane direction (S3 direction), stress concentration (singularity) is observed at the edges of rubber ring, as shown in Fig 4.19. This

is due to the fact that plastic deformation is not taken into account in material properties. When the strain is beyond linear range, linear extrapolation is used to get the corresponding stress while plastic deformation occurs in real life. Therefore, the results of the outermost four layers of elements are excluded in Fig 4.20 (left) to ignore the edge effects, correspondingly 2 mm from the edge. It can be seen that LE22 distribution is almost uniform through z direction in Fig 4.20 (right), indicating that 2D model is representative to 3D model in case of LE22 distribution.

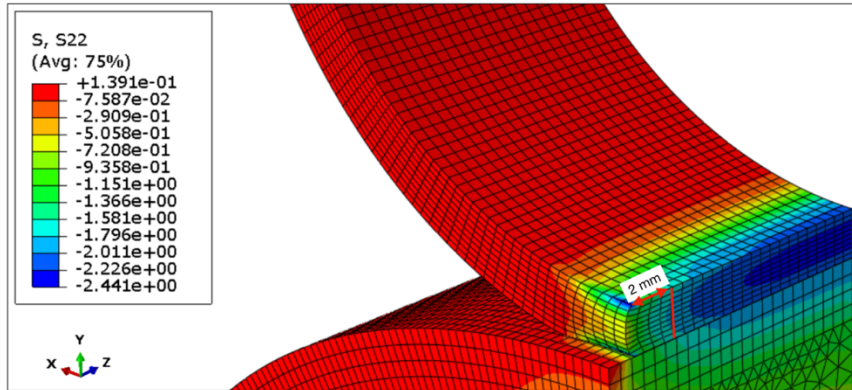


Figure 4.19 S22 distribution along the out-of-plane direction (S3 direction)

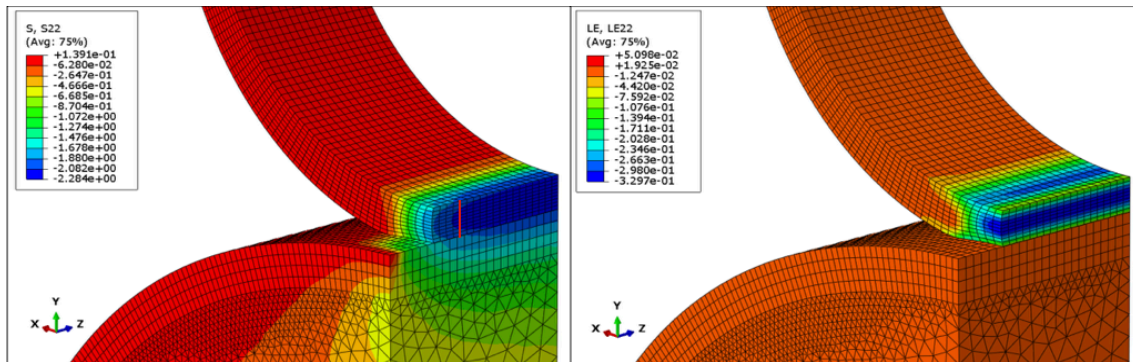


Figure 4.20 S22 (right) and LE22 (left) distribution along the out-of-plane direction (S3 direction) when the four outermost layers of elements in rubber are removed, and the element size along S3 direction is 0.5 mm

The distributions of S22, S33, LE22, LE33 and CPRESS along the contact line are plotted in Fig 4.21 and the results of LE22 and LE33 at the 5th point, that is 2 mm from the left ( $x = -21$ , marked as a red line in Fig 4.20 left), are compared for mesh refinement in Fig 4.22. It can be concluded that the distributions of variables mentioned above are converged at the z values (along x axis in Fig 4.21) ranging from -21 to 0 mm when the mesh size is larger than 0.5 mm. The relative errors are 8% and 5% for LE22 and LE33, respectively, when compared to that of the smallest mesh size. The relative errors are rather larger due to small denominator. The absolute error is 0.01 and 0.003, which are way smaller than the accuracy of DIC results. Therefore, the results can be considered to be converged at 0.5 mm of the mesh size along z direction.

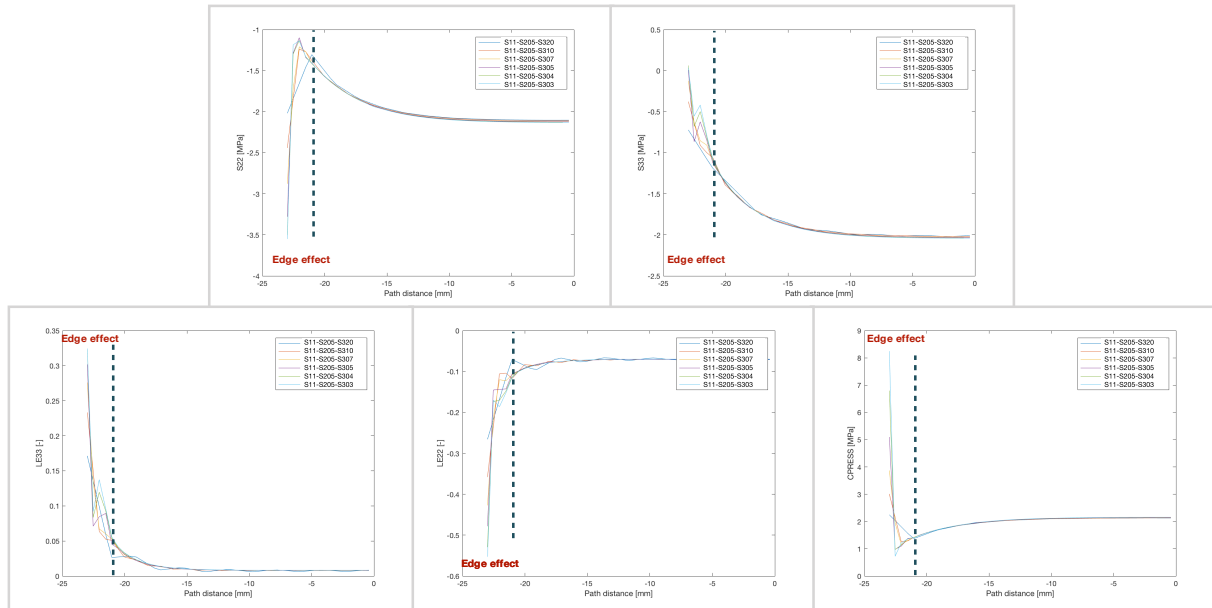


Figure 4.21 Distributions of S22, S33, LE22, LE33 and CPRESS along the out-of-plane direction under various mesh sizes

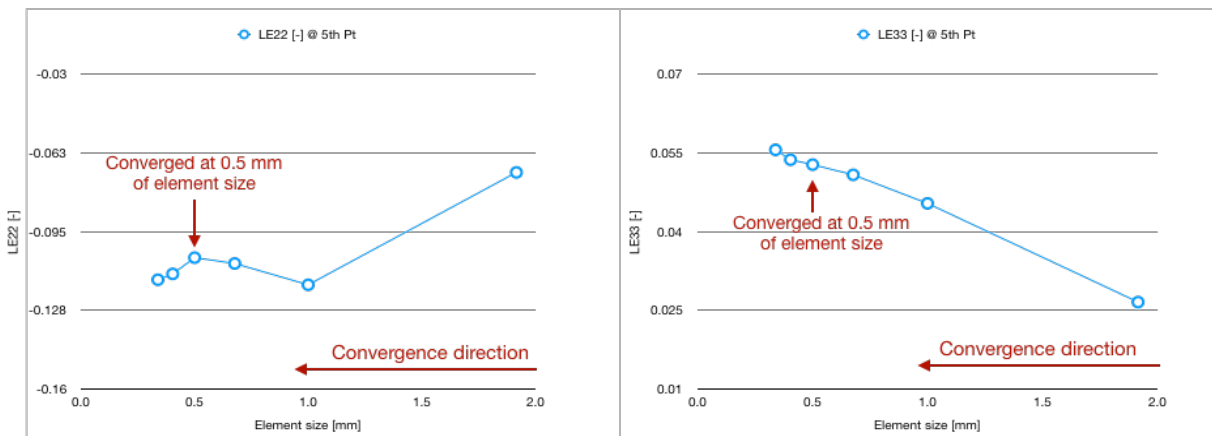


Figure 4.22 Mesh refinement of the 5th point ( $x = -21$ ) in the out-of-plane direction (S3 direction)

In other words, results are converged when mesh size S11-S205-S305, which refers to the mesh size of 1 mm in S1 direction, 0.5 mm and in both S2 and S3 direction.

#### The influence of higher order element

Fig 4.23 compares LE33 between the fully integrated linear elements and reduced integrated quadratic elements under same mesh size S11-S205-S305. Quadratic elements with reduce integration are used instead of full integration since the former is computationally cheaper than the latter. Similar to the comparison in 2D model, quadratic elements are severely distorted at the edge, causing unrealistic stress concentration. As a result, linear elements with full integration are used for later analysis.

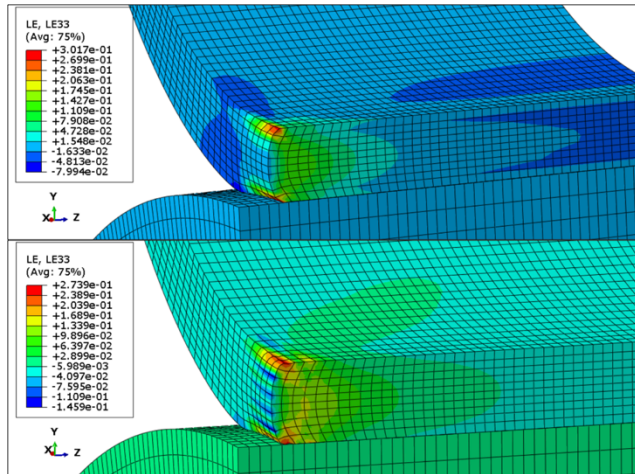


Figure 4.23 Comparison of LE33 between linear and quadratic element

### 4.1.3 Two-dimensional rolling model.

#### Steps

There are five steps in the 2D rolling model as shown in Fig 4.24. The first four steps are exactly the same as those stated in 2D static contact model. The only difference is that the full model is analyzed instead of half model, since symmetric condition about y axis is not applicable anymore for the rolling.

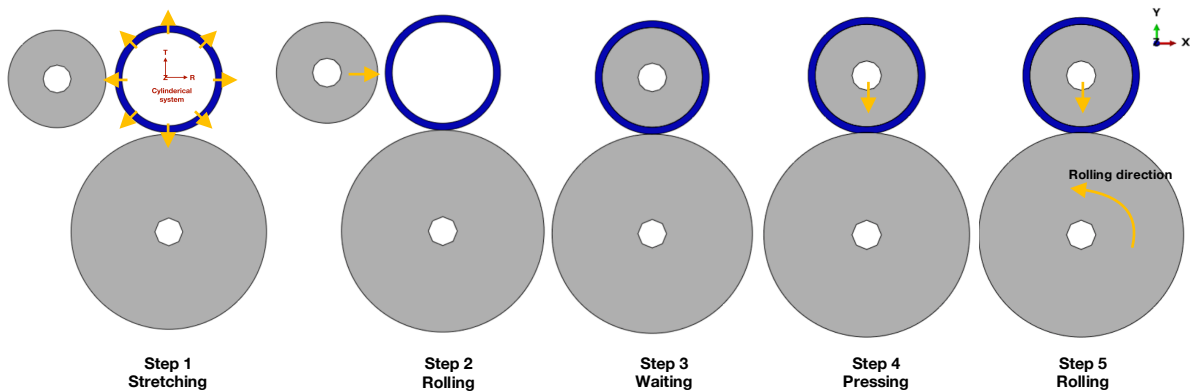


Figure 4.24 Step explanation for 2D rolling model

All forces, BCs and interactions are summarized in table 4.6. BC1 - 5 are similar to that in 2D static model (table 4.2). In the rolling step, the concentrated force applied to RP-1 at step 4 is propagated. RP-1 is only fixed in U1 and RP-2 is fixed in both U1 and U2. A boundary condition of UR3 is applied to RP-2 and allows the point RP-2 to rotate. Since RP-2 is coupled to inner surface of the mandrel, the mandrel will rotate around RP-2. The rotating angle is  $180^\circ$  so that the mandrel rotates half round in the model.

	Content	Regin	Constraints	Coordinate system		Content	Initial Step	Step 1	Step 2	Step 3	Step 4	Step 5		
Froce	A concentrated force to press roller	RP-1	F	Global		A concentrated force to press roller		Stretching	Roller moving	Waiting	Pressing	Rolling		
Boundary Conditions	BC1	Fix mandrel	RP-2	$U1 = U2 = UR3 = 0$	Global	Boundary Conditions	BC1	Fix mandrel	Created	Propagated	Propagated	Propagated	Inactive	
	BC2	Stretching rubber	Rubber's inner surface ( $\widehat{C_1D_1}$ )	$U1 = 1.5$	Cylindrical		BC2	Stretching rubber	Created	Propagated	Inactive	Inactive	Inactive	Inactive
	BC3	Moving roller	Entire roller	$U1 = 35$	Global		BC3	Moving roller		Created	Inactive	Inactive	Inactive	Inactive
	BC4	Roller Y constrain	Entire roller	$U2 = 0$	Global		BC4	Roller Y constrain		Created	Propagated	Inactive	Inactive	Inactive
	BC5	Roller constrain in pressing	RP-1	$U1 = 35, UR3 = 0$	Global		BC5	Roller constrain in pressing			Created	Propagated	Inactive	Inactive
	BC6	Roller constrain in rolling	RP-1	$U1 = 80$	Global		BC6	Roller constrain in rolling					Created	Propagated
	BC7	Mandrel constrain in rolling	RP-2	$U1 = U2 = 0$ $UR3 = 3.14$	Global		BC7	Mandrel rolling & constraint						Created
Interactions	Int-1	Interaction of roller and rubber	Between $\widehat{C_1D_1}$ and $\widehat{C_2D_2}$	/		Interactions	Int-1	Interaction of roller and rubber			Created	Propagated	Propagated	
	Int-2	Interaction of rubber and mandrel	Between $\widehat{AE}$ and $\widehat{FB}$	/			Int-2	Interaction of rubber and mandrel				Created	Propagated	

Table 4.6 Summary of loads, BCs and interactions and their actives in each step

Similarly, the first four steps are general static steps while general dynamic step is used in the rolling process, where dynamic responses are investigated, involving nonlinearity and contact (Abaqus, 2011). The commonly applied rolling speed is 100 mm/s for the tape winding process with in-situ consolidation as stated by Stokes-Griffin *et al.* (Stokes-Griffin & Compston, 2016). The detailed setup is discussed in Appendix 2.3.

### Mesh refinement

The mesh strategy is the same as that in the 2D static model shown in Fig 4.5. The element type is linear element with full integration as concluded in section 4.1.1. Only the contact pressure (CPRESS) will be checked for convergence study, which is affected more by the mesh size along S1 direction during rolling process. Fig 4.25 (left) plots the CPRESS distribution along the rubber's outer surface line over the rolling time using the mesh size of S11S205, which is the converged mesh sizes of the 2D static model. The x axis stands for the distance of the rubber's outer surface line, which is marked as red arrow in Fig 4.25 (right) starting from A and increasing anticlockwise. From Fig 4.25 (left), it can be seen that in each time frame, CPRESS has a similar distribution along the contact area. The peak shifts from left to right, indicating the contact area moves anticlockwise when the mandrel rotates half round. As a result, the CPRESS peak at every time increment is compared for mesh refinement.

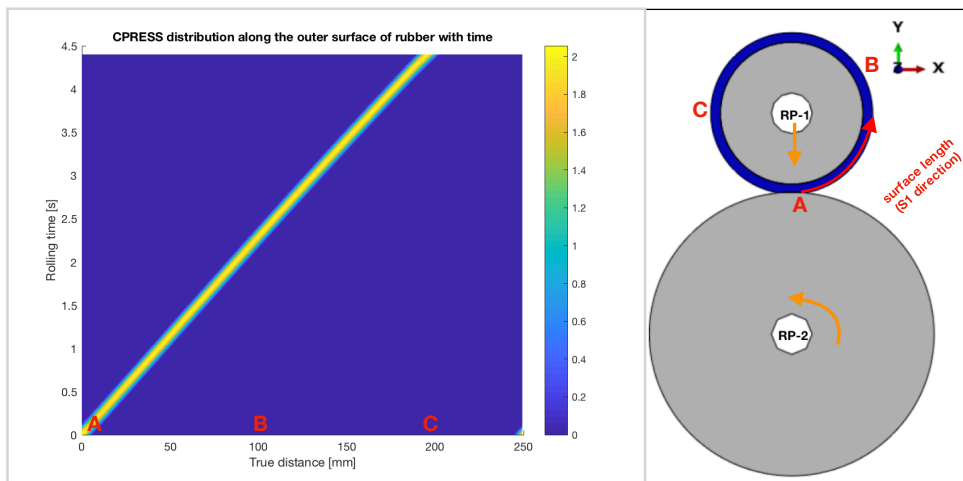


Figure 4.25 CPRESS distribution of the rubber's outer surface over rolling time (left), where the true distance of the rubber's outer surface is marked on the right before rolling (rolling time = 0)

At each time increment, the maximum CPRESS is plotted in Fig 4.26 (left) under different mesh sizes along S1 direction, which has a major influence on the pressure distribution compared to the one along S2 direction. The mesh size in S2 direction is fixed at 0.5 mm

except for the case of S115S2075, since the element aspect ratio should be no larger than 2. Regardless of the mesh size, the curves have similar trends: the peak value is reached right after the mandrel starts rotating. After a sudden drop, the maximum CPRESS values slightly increases and get stabilized after 1 s. The reasons will be further discussed in section 4.3. The averaged CPRESS after stabilization is compared under the three different mesh sizes in circumferential (S1) direction. The results are shown in Fig 4.26 (right). It can be seen that the results are converged when the mesh size is 1 mm (S11S205). It has a coefficient of variants (COV) is 0.5 % in the stabilizing range. The relative error of 2% compared to the finest mesh and the corresponding absolute error is 0.04 MPa, which is smaller than the accuracy of pressure sensitive film. Therefore, the mesh size of (S11S205) is selected.

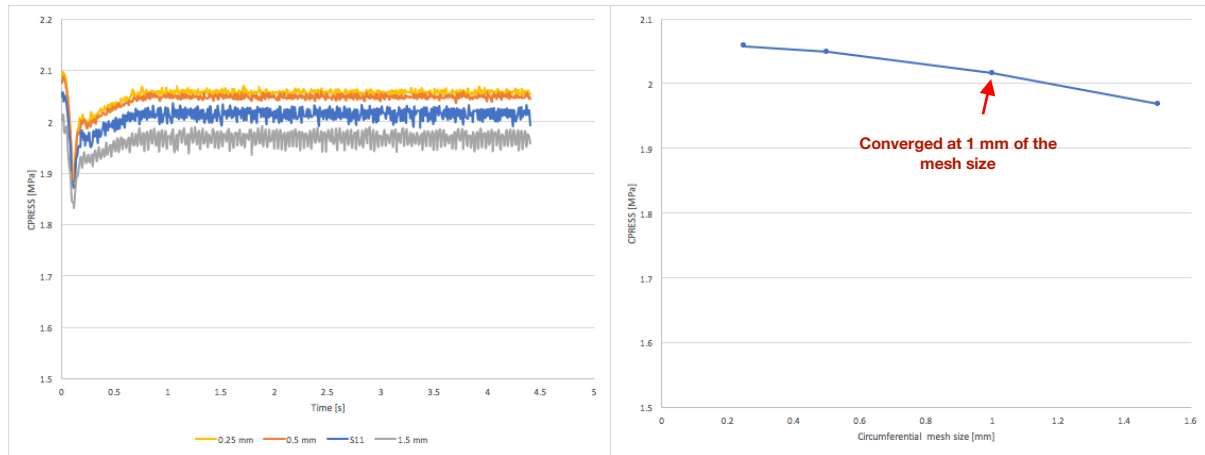


Figure 4.26 Maximum CPRESS along the rubber's outer surface line over rolling time using different mesh sizes in circumferential direction (left) and averaged CPRESS after stabilization under different mesh size

## 4.2 Model selection

In this section, two comparisons will be made to confirm the assumptions made in model reduction. As mentioned before, tape winding process is a 3D rolling process. The aim is to reduce the FE model to 2D static model, in order to save some computational time. Therefore, two comparisons have been made to check whether the model reduction can be achieved or not. This is done by comparing 2D static model and 3D static model to check if it is possible to reduce the model from 3D to 2D. Then, 2D static model and 2D rolling model is compared to see whether the rolling process can be simplified to a static process. The speed used in the 2D rolling model is 100 mm/s, which is commonly applied in the application (Stokes-Griffin & Compston, 2016). The model dimension used in comparison among those three model are the same. The diameter is 70 mm for the roller and 140 mm for the mandrel. The rubber dimension is 67 mm of the inner diameter and the thickness is 5 mm. In 3D model, the width is 25 mm for both the roller and the mandrel, and 23 mm for rubber. The forces applied to the rubber center are equivalent, that are 8 N ( $8 \text{ N/mm} * 1 \text{ mm}$ ) for 2D model with the plane strain width of 1 mm, and 184 N ( $8 \text{ N/mm} * 23 \text{ mm}$ ) for 3D model with the real width of 23 mm.

### 4.2.1 Comparison between 2D and 3D static models

The distributions of the contact pressure (CPRESS) between the rubber and the mandrel are compared between 2D and 3D static contact models under equivalent forces, as shown in Fig 4.27. Also, the CPRESS distribution of 2D and 3D models along the circumferential direction and through the out-of-plane direction are plotted in Fig 4.28, respectively, where the locations of point A-E in Fig 4.27 are also marked near the CPRESS curves. The dashed line is 2 mm

from the sides, suggesting the range that is influenced most by the edge effects discussed before. In the circumferential direction, CPRESS shows a similar trend between  $\overline{AB}$  and  $\overline{CE}$  but 3D model has a higher value. The relative error of their peak value is 12.7%. In the out-of-plane direction, CPRESS at point A in the 2D model suggests a constant value along the thickness, while CPRESS varies in 3D model. Along the line  $\overline{CD}$ , there is higher CPRESS in the middle than on the sides. This is because LE33 ( $\varepsilon_z$ ) assumed to be zero in the 2D model due to the plane strain condition, is not valid through the whole thickness in the 3D model. Fig 4.29 plots the LE33 distribution in 2D and 3D static model. Along the line  $\overline{CD}$ , point F is the location where LE33 = 0. On one hand, it can be seen that the assumption of plane strain condition is confirmed in the width range of line  $\overline{CF}$ , where LE33 is so small (-0.02 - 0) that it can be assumed to zero. In order to have good quality during tape winding, high pressure is required in a contact width larger than the tape width (10 mm). The length of  $\overline{CF}$  is around 10 mm in the 3D model. Note that 3D model is a quarter of the full model. Hence, the width range where the pressure is comparable to that in 2D model is 20 mm in the whole model, which is double the tape width (10 mm) and thus the verified width range is sufficiently large so that it covers the whole tape width.

On the other hand, LE33 in the line  $\overline{FD}$  is not negligible anymore. Rubber is assumed to be an incompressible material as discussed before. Resulting from that, it has more lateral deformation on the sides since there is no constraint, leading to less contact pressure transformed from the roller. As a result, 2D model is able to predict the CPRESS distribution accurately in the middle part of 3D model (in the thickness rang of  $\overline{CF}$ ), which provides high pressure in a sufficiently large area compared to the tape dimension (the width of out-of-plane).

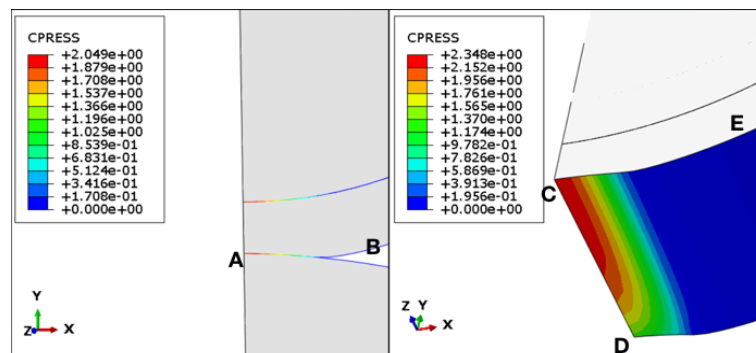


Figure 4.27 Comparison of contact pressure (CPRESS) between 2D and 3D static models

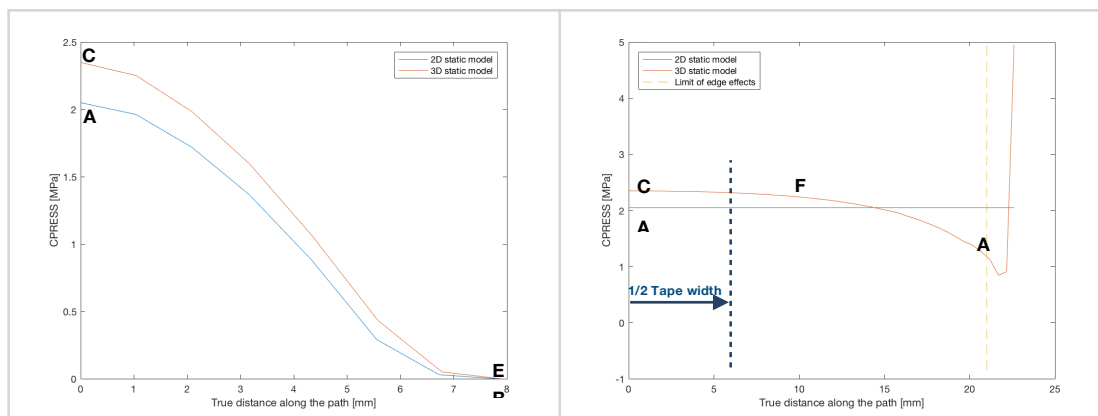


Figure 4.28 Comparison of contact pressure (CPRESS)<sup>1</sup> between 2D and 3D static models along the deformed circumferential length (left) and in the out-of-plane direction (right)

<sup>1</sup> It should be noted that the CPRESS distribution in Fig 4.28 (left) is along deformed circumferential length

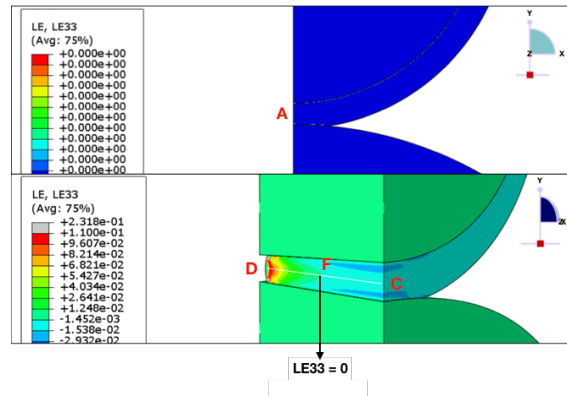


Figure 4.29 Comparison of out-of-plane logarithmic strain (LE33) between 2D (upper) and 3D (lower) static models

In addition, the results of vertical logarithmic strain (LE22) at the rubber are compared between 2D (at point A) and 3D ( $\overline{CD}$ ) static contact models under equivalent forces, as shown in Fig 4.30, where 2 mm-thick layer of rubber ring is removed from the side due to edge effect, as discussed in the previous section. In xy plane, the LE22 distributions are similar comparing 2D with 3D models. In out-of-plane direction (z direction), the LE22 at point A in 2D model and that along the line  $\overline{CD}$  in 3D model are plotted in Fig 4.31. Similarly, the dashed line is 2 mm from the sides, suggesting the range that is influenced most by the edge effects discussed before. In the 2D model, LE22 at point A indicates a constant value through the plane strain thickness, while in the 3D model, LE22 looks almost constant but it is 2.5% larger on the sides than that in the middle. This is due to the fact that rubber has larger lateral deformation on the sides, which is discussed in the previous paragraph. Nevertheless, the results of LE22 and LE33 looks consistent through the thickness direction in the middle part of rubber ( $\overline{CF}$ ).

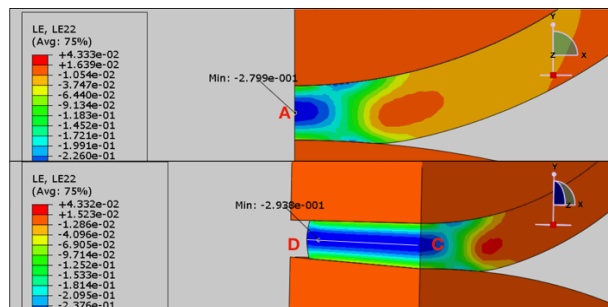


Figure 4.30 Comparison of vertical logarithmic strain (LE22) between 2D and 3D static models, where a 2 mm-thick layer of rubber ring is removed from the side due to edge effect

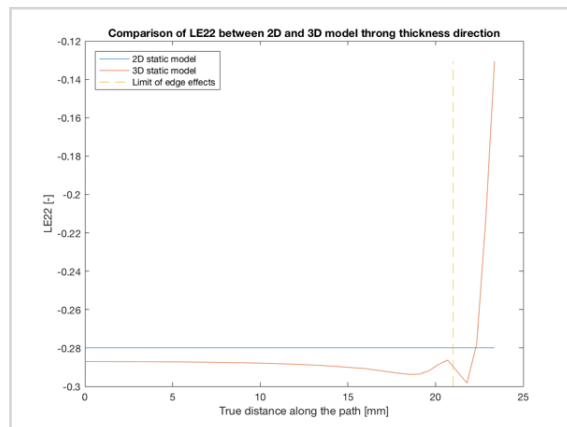


Figure 4.31 Comparison of vertical logarithmic strain (LE22) between 2D and 3D static models in the out-of-plane direction

As a conclusion, 2D model of static contact is able to provide good results of the contact pressure and the logarithmic strain (LE) in the middle part of rubber (20 mm of the width), which is very interesting since the 12.7 mm-wide tape will be pressed by the middle part of rubber.

#### 4.2.2 Comparison between 2D static and 2D rolling models

The maximum CPRESS along the rubber's outer surface line is plotted in Fig 4.26 over the rolling time ( $t_{rolling}$ ). After initiation phase ( $t_{rolling} = 0 - 1s$ ), the maximum CPRESS gets stabilized. The maximum CPRESS is averaged when  $t_{rolling} = 1 - 4.4s$  and is compared with that at  $t_{rolling} = 0 s$ . It turns out that there is a small drop of CPRESS comparing the maximum CPRESS at  $t_{rolling} = 0 s$  with that at  $t_{rolling} > 1s$ . The reason is that the contact status between roller and rubber changes due to friction. Fig 4.32 compares the contact status (left), friction/CSHEAR1 (middle) and circumferential stress  $S_\theta$  distribution (right) at  $t_{rolling} = 0s$  and  $t_{rolling} = 4s$ , where the mandrel almost rotated  $180^\circ$  and the maximum CPRESS is already stabilized. The cylindrical system is shown in Fig 4.24. It can be seen that the opened regions (black lines) shifts to the right during rolling, owing to the variation of the friction that exists in the contact region (red and green lines). As shown in Fig 4.32 (middle), the maximum friction occurs on the left between roller and mandrel, causing the roller-rubber opening increase and shift to the right. Furthermore, the variation of friction also leads to the changing of the circumferential stress ( $S_\theta$ ) in the rubber. Comparing the  $S_\theta$  at  $t_{rolling} = 0s$  and  $t_{rolling} = 4s$  (Fig 4.32 (right)),  $S_\theta$  in the rubber decreases from positive values to negative values in the contact region, meaning that the rubber elements are compressed at  $t_{rolling} = 4s$ . Under incompressible assumption, circumferential compression leads to a small increase of the thickness, which indicates that some of the stress is used to balance the pushing force provided by the rolling mandrel and thus not all of the compaction force is transformed to the contact area. As a result, there is a slight drop of the vertical stress, causing a small drop in CPRESS. The influence of rubber thickness will be further discussed in the section 4.3.2. Additionally, in the initiation phase ( $t_{rolling} = 0 - 1s$ ), CPRESS drops by 10% and then slightly increases to stabilized value. The reason for the 10% drop is the sudden change in contact at the beginning of the rolling. It is a numerical issue, as indicated by Fig 4.33, where the maximum CPRESS along the rubber's outer surface is compared with the maximum COPEN<sup>1</sup> between roller and rubber during the rolling time. Before stabilizing, the maximum COPEN increases constantly, while the maximum CPRESS suddenly drops and then increases again. Therefore, it is suggested to wait for some time after the mandrel starts to rotate and then the tape to be laid on the mandrel and start consolidation.

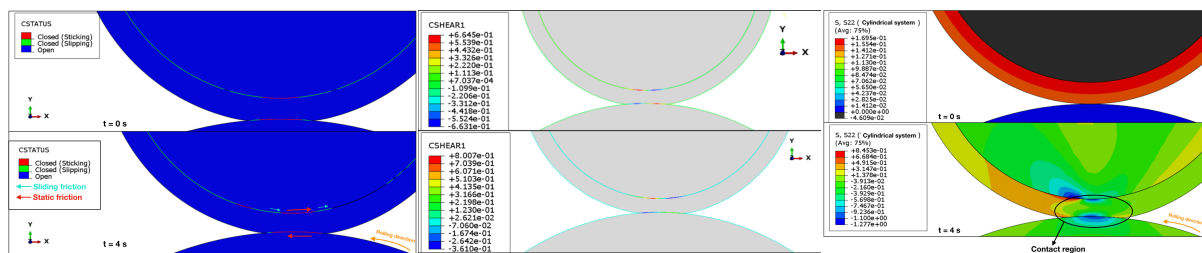


Figure 4.32 Comparisons of contact status (left), CSHEAR (middle) and circumferential stress ( $S_\theta$ ) distribution (right) at rolling time  $t_{rolling} = 0s$  and  $t_{rolling} = 4s$  in the 2D rolling model with the converged mesh size (S11S205) at the constant rolling rate of 100 mm/s (rolling direction: anticlockwise)

<sup>1</sup> COPEN is the gap between two adjacent surfaces in mm

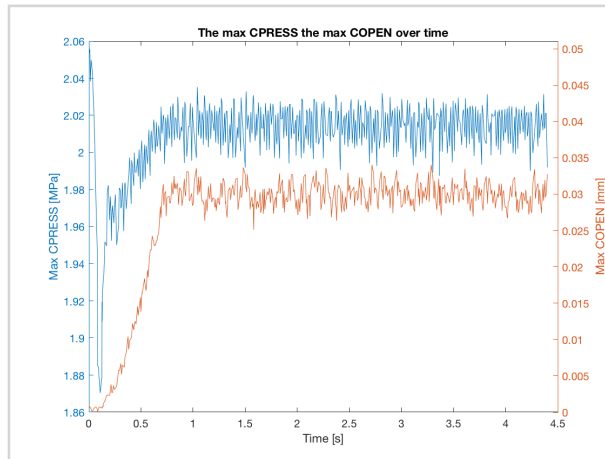


Figure 4.33 COPEN distribution along the rubber's inner surface over time (left y axis) and the maximum COPEN over time (right y axis)

The CPRESS distribution is averaged in the 2D rolling model after it stabilizes ( $t_{rolling} = 1 - 4$  s), using the same method as explained in section 3.1.2. The results of the averaged CPRESS curve is compared with those at different rolling times as illustrated in Fig 4.34 (left). In Fig 4.34 (right), the averaged curve is again compared with the CPRESS distribution obtained in the 2D static model under the equivalent force. They have similar shape but the curve of the rolling model shifts around 0.3 mm to the left due to the frictional contribution. Hence, the results in 2D static model agree with that in the 2D rolling model, which confirms the assumption of simplifying the rolling process to a static contact due to low rolling speed. Therefore, rolling process at a low rolling speed (100 mm/s) can be modeled as static contact.

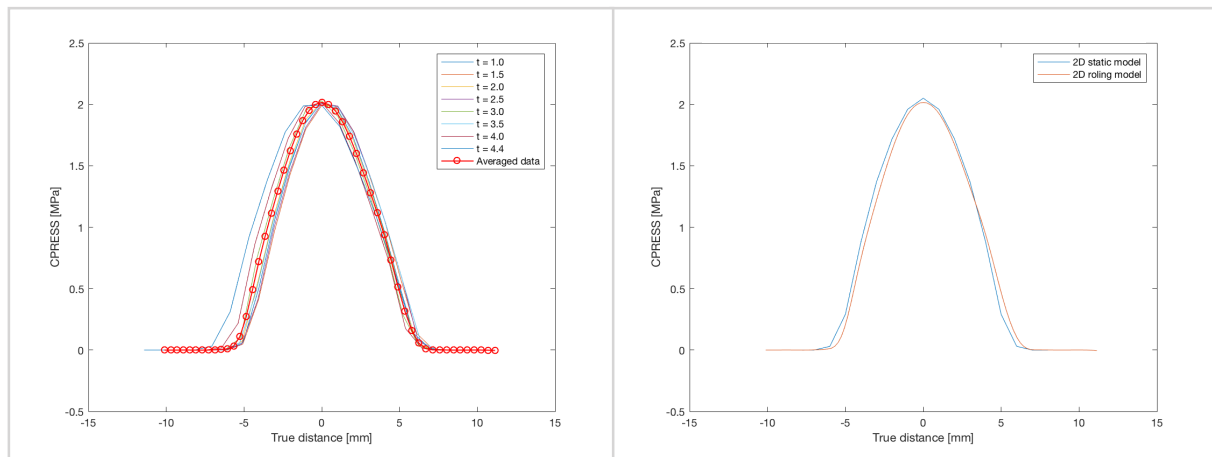


Figure 4.34 The pressure (CPRESS) distribution along undeformed circumferential length at different rolling time in the 2D rolling model (left) and comparison of CPRESS distribution between 2D static and rolling model (right)

### 4.2.3 Conclusion

In a nutshell, 2D static model is able to get similar pressure results comparing to 3D static model and 2D rolling model (rolling speed up to 100 mm/s). Running a 2D static model takes less than 1min, 3D static model takes 9h, 2D rolling model takes 5h, not to mention the 3D rolling model. Therefore, great amount of computational time can be saved by model reduction.

## 4.3 Results & discussion

Several factors that influence the pressure distribution between rubber and mandrel will be discussed, including the compaction force applied to the roller, the rubber thickness, and whether a pre-stretching force in the rubber is used in the rubber or not. Then, a trade-off is made to optimize rubber dimensions and the compaction force based on the equipment limitations and pressure requirements. It should be noted that all the FEM results are obtained in 2D static model since it is concluded in the previous section that the CPRESS results in 2D static model are consistent with that in 3D static model and 2D rolling model.

### 4.3.1 Influence of the compaction force on the pressure distribution

The influence of the compaction force on the pressure distribution is investigated by comparing the pressure distributions in the contact area between the rubber and the mandrel under three different forces (4-8-12 N/mm) in the 2D static model. The rubber dimensions are the same (inner diameter of 67 mm and the thickness of 5 mm). The results are shown in Fig 4.35. As mentioned before, the compaction force has a unit of Newton per width (N/mm) since the model width will not affect the results under plane strain condition. According to Fig 4.35 (left), the trend of the pressure distributions under different forces are similar and comparable with that in literature (Levy et al., 2012) as shown in Fig 2.7. The pressure distribution can be evaluated by maximum CPRESS and the contact length, which is defined as the circumferential length where CPRESS is larger than zero. As mentioned in section 2.2, intimate contact occurs when two surfaces are in contact (CPRESS > 0), which is the prerequisite of autohesion in order to achieve good bond quality. Combining with the contact length and rolling speed, the processing time can be determined. According to Fig 4.35 (left), the relation between maximum CPRESS/contact length and compaction force is plotted in Fig 4.35 (right). The maximum pressure (CPRESS) increases linearly when the force goes up from 4 to 12N/mm. However, the contact length get after 8 N/mm, indicating that the influence of the compaction force on the contact length is negligible for thin rubber (thickness of 5 mm). Therefore, the force applied to the roller mainly affects the pressure value.

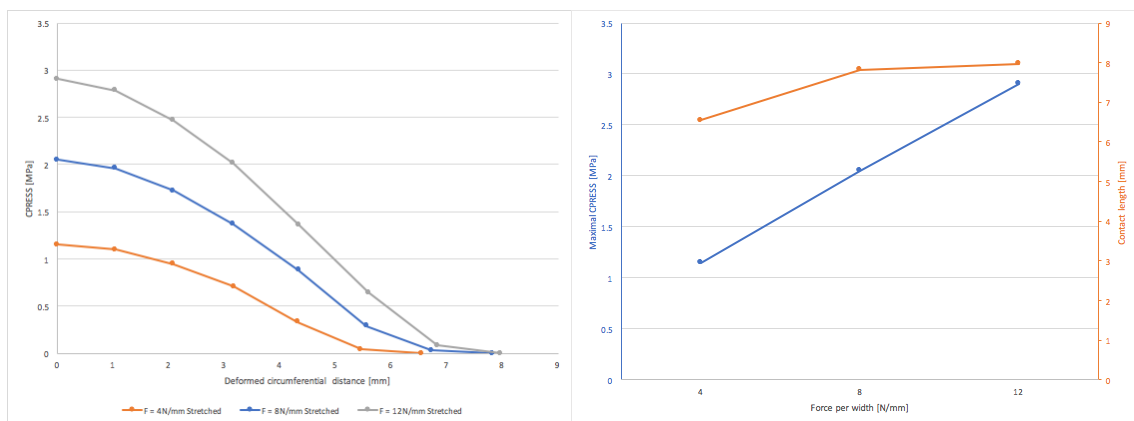


Figure 4.35 Pressure (CPRESS) distribution along deformed circumferential length between the mandrel & a 5 mm thick rubber under different forces (left), according to which the variation of maximum CPRESS/contact length under different forces (right)

### 4.3.2 Influence of rubber thickness on the pressure distribution

The influence of the rubber thickness on the pressure distribution is investigated by comparing the pressure distributions in the contact area between the rubber and the mandrel with three different rubber thickness (5-10-15 mm) in the 2D static model. The pre-stretching force is assumed to be sufficient to avoid rubber-roller separation. The inner diameter is 67 mm for 5 mm-thick rubber and 65 mm for 10 mm-thick and 15 mm-thick rubber. The results are shown in Fig 4.36. The compaction

force is fixed at 12 N/mm in the Fig 4.36 (left), according to which the variation of maximum CPRESS/contact length is plotted with different rubber thicknesses. It can be seen in the Fig 4.36 (left) that the rubber thickness changes both the maximum pressure and the contact length. Based on Fig 4.36 (right), the maximum CPRESS increases almost linearly and contact length decrease almost linearly as the rubber get thicker. In other words, thicker rubber tends to have lower maximum CPRESS but larger contact length compared to thinner ones. Thicker rubber is preferred since its larger contact length increases the bonding time comparing to thinner rubber at same rolling speed. However, in order to achieve same maximum CPRESS, larger force is required for thicker rubber, meaning that more power of the pressing equipment will be needed. Nevertheless, a trade-off has to be made between the contact length and the compaction force, which will be discussed later.

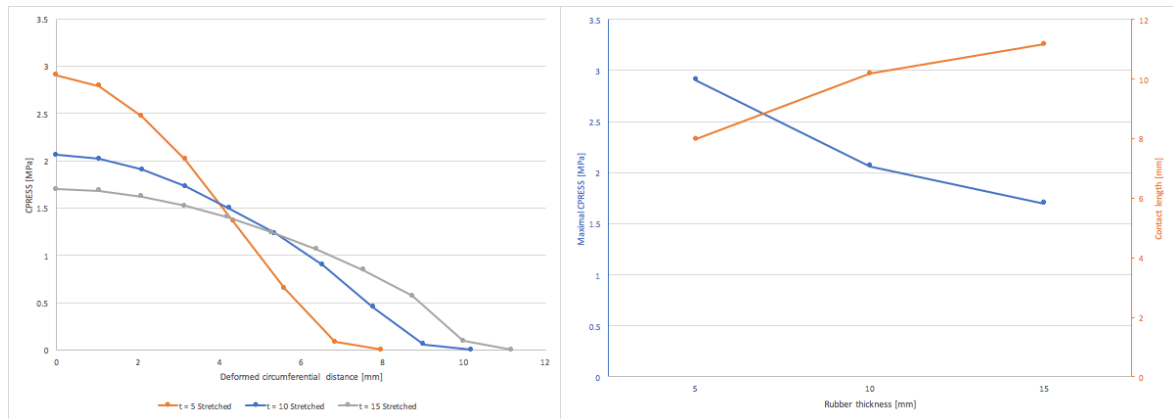


Figure 4.36 Pressure (CPRESS) distribution along deformed circumferential length under different rubber thicknesses: using same force of 12 N/mm (left), according to which the variation of maximum CPRESS/contact length under different rubber thicknesses (right)

### 4.3.3 Influence of rubber's pre-stretching force on the pressure distribution

The influence of using pre-stretching or not on the pressure distribution is investigated by comparing the pressure distributions in the contact area with pre-stretched rubber and non-stretched rubber. Three loads are used to verify this influence of the pre-stretching force. The pre-stretching force is selected such that it is assumed to be sufficient to avoid rubber-roller separation and thickness reduction can be negligible. The pre-stretched rubber has an inner diameter of 67 mm and the non-stretched rubber has an inner diameter the same as the roller's diameter (70 mm). They have the same thickness of 5 mm. The results are shown in Fig 4.37. It can be seen that the pressure distribution of pre-stretched rubber and non-stretched rubber are similar for all three loads. Rubber-roller separation is observed but it doesn't occur in the contact region. Therefore, pre-stretching force is not make any difference in 2D static FE models.

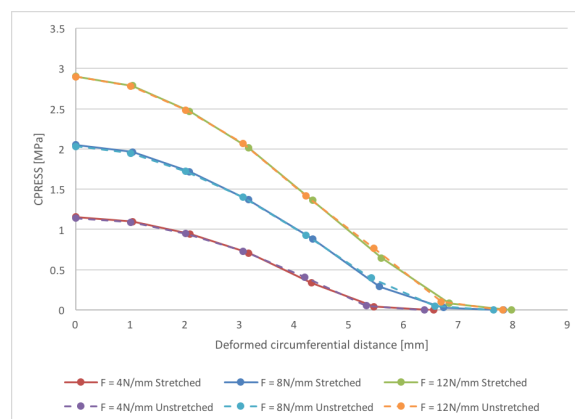


Figure 4.37 Pressure (CPRESS) distribution along deformed circumferential length with pre-stretched rubber and non-stretched rubber under different loads

The CPRESS distribution along the deformed circumferential length is also compared between pre-stretched and non-stretched rubber in the 2D rolling model as it might affect separation. The roller models are shown in Fig 4.38 (a). The force applied to the roller is the same (8N/mm). The maximum CPRESS is compared over the rolling time between pre-stretched rubber and non-stretched rubber in Fig 4.38 (b). It can be seen that both of them have an initiation phase, which is 1 s for pre-stretched rubber and less than 0.5 s for non-stretched rubber. The pre-stretched rubber has a long initiation phase, which is probably due to the interaction in the stress field at the beginning of rolling. In addition, it is interesting to see that non-stretched rubber has a lower stabilized pressure value compared to that of pre-stretched rubber. This is because non-stretched rubber become looser, as indicated by the smaller circumferential stress  $S_{\theta}$  in Fig 4.39. Accordingly, less force is transferred from the roller when rubber has more lateral deformation. As a result, pre-stretched rubber is used instead of the non-stretched one since there is less pressure drop during rolling. However, there are more practical reasons that why pre-stretched rubber is preferred. In reality, the winding setup usually suffers from the misalignment between the roller and the mandrel, which causes rubber move to one side during process, due to the fact that there is no constraint in the out-of-plane direction. In simulation, this will not occur because rubber, roller and mandrel are constrained by the symmetric BCs. Also, the roller and the mandrel are modeled to be perfectly alignment. As a result, using pre-stretched rubber is one of the options that can prevent the rubber from moving to the sides. Other options will be explained in next chapter to prevent rubber's lateral movement.

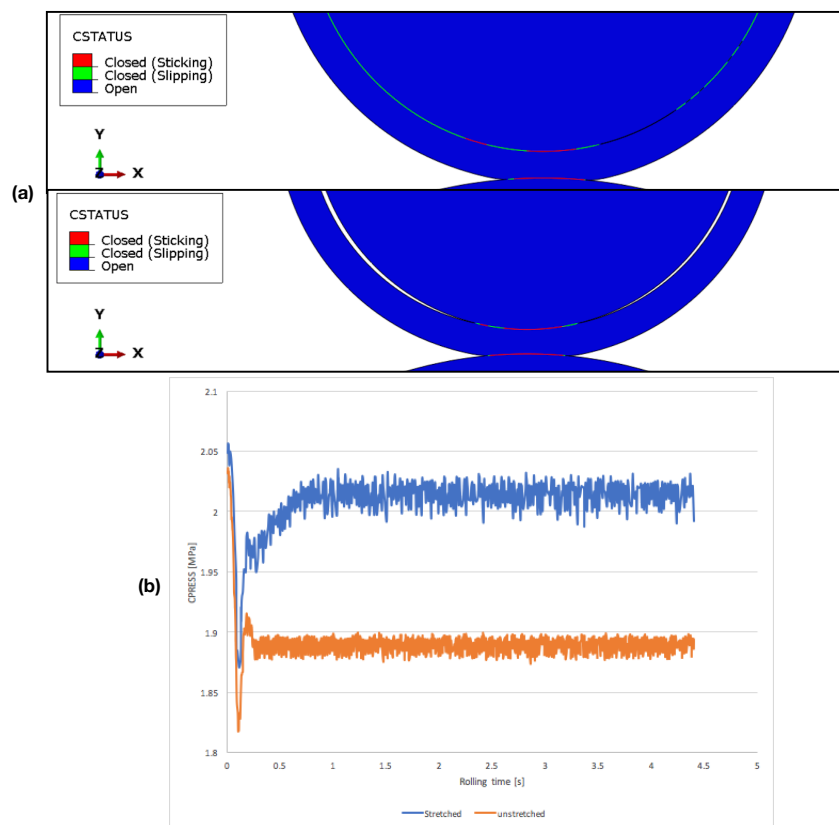


Figure 4.38 (a) 2D rolling models for pre-stretched rubber (upper) and unstretched rubber (lower) and (b) Comparison of the maximum CPRESS over time between pre-stretched rubber and non-stretched rubber

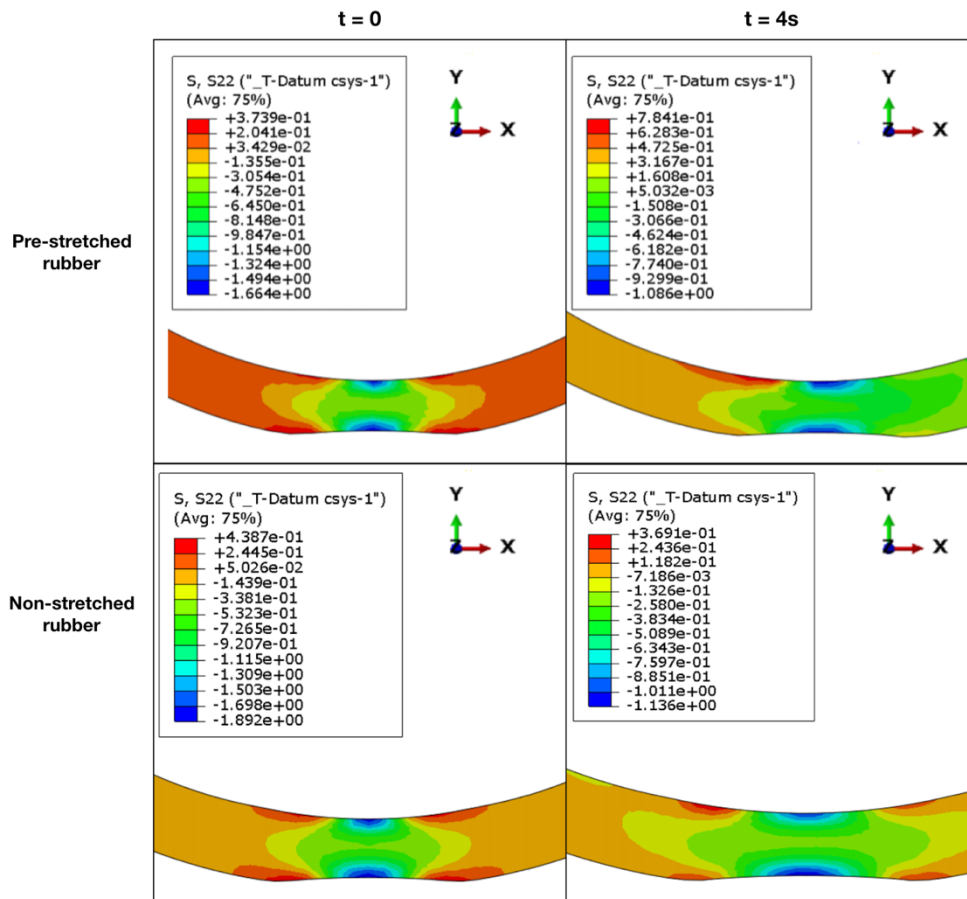


Figure 4.39 The comparison of circumferential stress ( $S_{\theta}$ ) distribution between pre-stretched rubber (1st row) and non-stretched rubber (2nd row) at roller time  $t_{\text{rolling}} = 0$  (1st column) and  $t_{\text{rolling}} = 4s$  (2nd column)

### 4.3.4 Rubber size optimization

As mentioned before, the pressure distribution can be evaluated by the maximum CPRESS and the contact length. Both of them are affected by compaction force and rubber thickness. Their effects on maximum CPRESS and contact length are presented in Fig 4.40 - 4.41. Fig 4.40 shows that the maximum CPRESS increases linearly when rubber gets thicker under same force, or when increasing the compaction force under same rubber thickness. In Fig 4.41, linear behavior is also observed between the contact length and rubber thickness/compaction force, except for thinnest rubber (5mm thick), where the force get saturated when the force is larger than 12 N/mm.

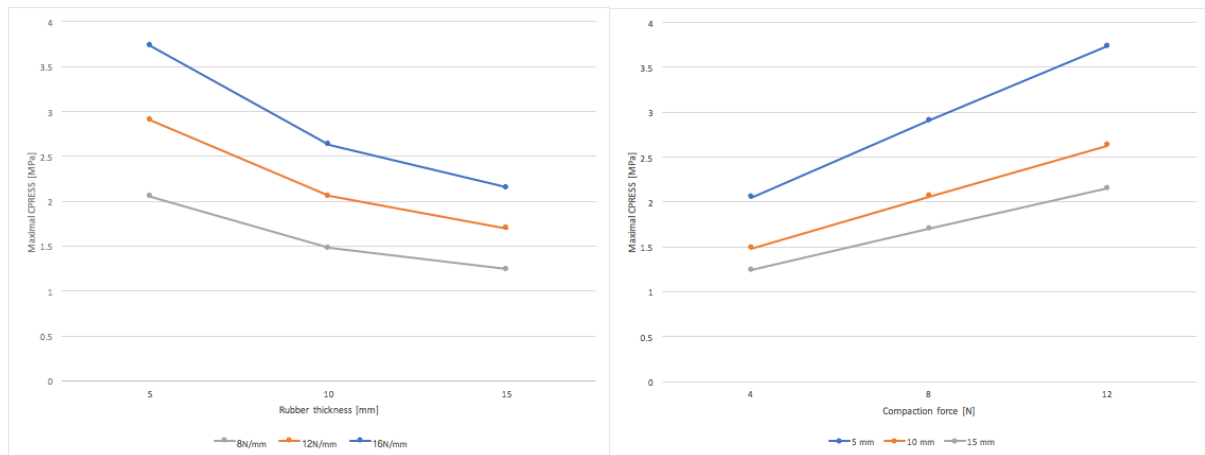


Figure 4.40 Effects of rubber thickness on maximum CPRESS under same compaction force (left) and effects of compaction force on maximum CPRESS under same rubber thickness (right)

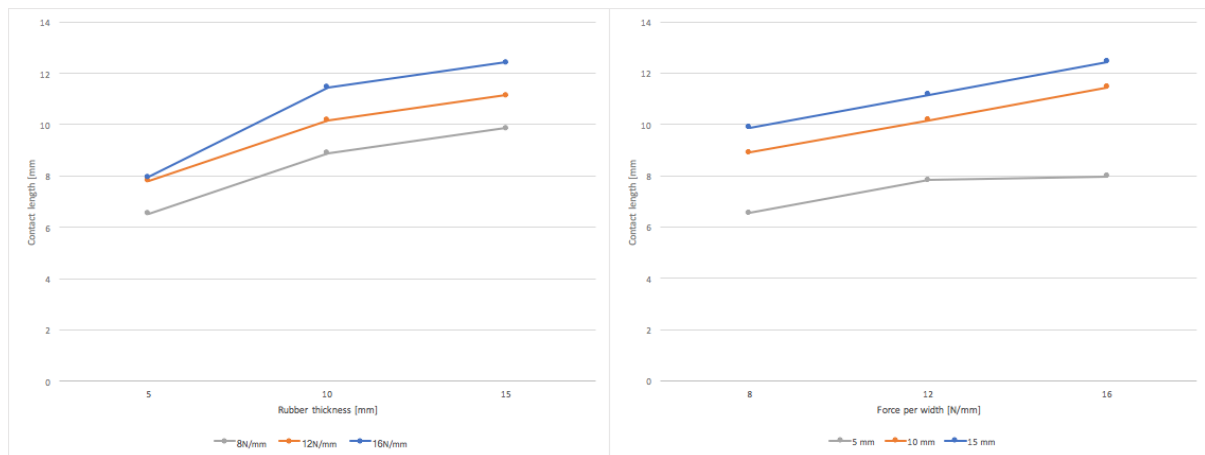


Figure 4.41 Effects of rubber thickness on contact length under same compaction force (left) and effects of compaction force on contact length under same rubber thickness (right)

The rubber dimension is selected mainly based on the equipment limitations and the pressure requirements. For one thing, the compaction force is usually limited by the equipment (*i.e.* the power of motor and pneumatic cylinder in this case). For another, pressure range is determined based on the theory of intimate contact (C Ageorges et al., 2001), where a good bond quality can be achieved when the thermoplastic tape is pressed for a certain amount of time, given sufficient temperature. Bonding time is influenced by the contact length, together with rolling speed. In order to speed up the manufacturing process of tape winding, rolling speed can be increased for larger contact length if the bonding time is fixed. To this end, thicker rubber is preferred since it provides larger contact length. However, larger compaction force is needed to achieve same maximum CPRESS than thinner rubber, indicating that more power of the pressing equipment is desired. Nevertheless, a trade-off is needed to select the rubber dimension based on compaction force and the pressure requirement.

## 4.4 Conclusion

In this chapter, finite element analysis is carried out to predict the pressure distribution in the contact area between rubber and mandrel. In order to save computational time, model reduction is made by using a 2D static contact model to simulate the 3D winding process based on several assumptions. 2D model can be simplified based on plane strain condition since the dimension in the contact area is rather small (10 mm) compared to the width dimension (50 mm). Furthermore, rolling process can be modeled as a static contact process due to the low rolling speed and thus the inertia effect can be ignored.

Three types of FE models are investigated, including a 2D static contact model, a 3D static contact model and a 2D rolling model. In order to confirm the assumptions made for model reduction, two comparisons are made. Firstly, 2D static model is compared with 3D static model to confirm the plane strain condition. Secondly, the pressure distribution in 2D static model is compared with that in 2D rolling model and it can be concluded that pressure (CPRESS) distributions are similar and thus the inertia effect is neglected. As a result, 2D static contact model is used to predict the pressure and the computational time is saved significantly from 9h of 3D static model and 5h of 2D rolling to 1min of 2D static model.

The pressure distribution in the contact area between rubber and mandrel is predicted by 2D models to study the influences of the compaction force applied to the roller, the rubber thickness, and whether a pre-stretching force in the rubber is used in the rubber or not. The influences of those three factors are discussed separately, followed by a guidance to optimize the rubber size. The compaction force affects more on the maximum CPRESS than on the contact length. Thicker rubber has larger contact length but smaller maximum CPRESS compared to thinner ones. Using a pre-stretching force have no influence on the pressure distribution in 2D static model but has a slightly larger maximum CPRESS in 2D rolling model than that without pre-stretching force. Under the compaction force of 8N/mm (in half 2D model), the difference (0.14 MPa) is rather small so that it might not be captured by pressure film. Rubber thickness can be optimized based on force limitation and pressure requirements. Thicker rubber is preferred due to the larger contact length compared to thinner rubber, leading to longer processing time and thus better bond quality. However, larger compaction force is required to have same maximum pressure. Therefore, a trade-off has to be made between rubber thickness and compaction force. Experiments have been conducted to validate the FE models, which will be elaborated in next chapter.



# 5 Experimental validation

Experiments have been conducted to validate the FEM models described in chapter 4, with several techniques including digital image correlation (DIC) and pressure sensitive film. First of all, the experimental setup is presented in section 5.1. Secondly, compaction force, provided by a pneumatic cylinder, is calibrated by measuring the force under various air pressures using a load cell. The strain/displacement field and pressure distribution are validated experimentally. As mentioned before, hybrid formation element is used to describe stress-strain behavior of rubber, where the stress and strain are treated independently and coupled together based on the constitutive theory and the compatibility condition (Abaqus, 2011). As a result, both of the vertical strain/displacement and pressure distribution in the contact area will be validated. In the section 5.3, the distribution of vertical displacement/vertical strain distribution on the one side of rubber is measured by DIC in both static contact and rolling processes, which will be later compared to the FEA results. In section 5.4, the pressure distribution in the contact area between roller and mandrel is obtained from the pressure sensitive film and compared with FEA simulations. Lastly, conclusions will be drawn to determine whether FE models are validated or not.

## 5.1 Experimental setup

The experimental setup mainly consists of a compaction roller, a rubber cover and a mandrel. As shown in Fig 5.1, the compaction roller is attached to a pneumatic cylinder and the compaction force is controlled by the pressure of the compressed air that is connected to the pneumatic cylinder. The control system of the air pressure is made of a pressure regulator and a pressure meter, as shown in Fig 5.2. Hence, the air pressure can be changed by adjusting pressure regulator and reading the pressure value in the pressure meter. Furthermore, the mandrel is connected to a motor so that it can rotate at a given speed. It should be noted that the compaction force is limited by the motor power. The roller gets stuck when the compaction force is larger than 580 N.

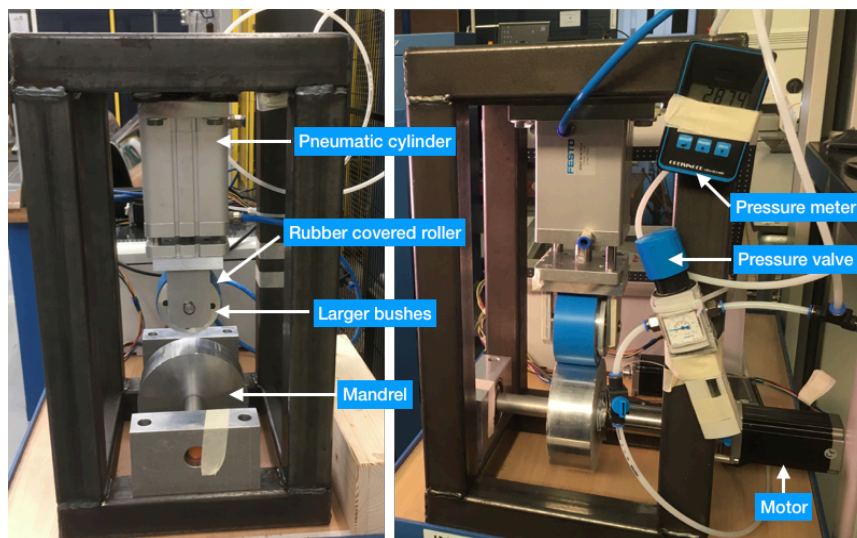


Figure 5.1 Experimental setup

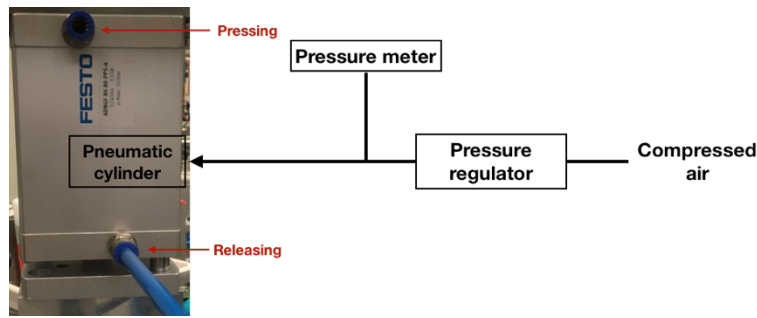


Figure 5.2 Control system of the air pressure

The width is 50 mm for the roller and mandrel and around 46 mm for the rubber cover. As explained before, rubber ring might be moved out during rolling due to the lack of lateral constraint. Therefore, two bushes are placed on the sides of the roller, which are 2.5 mm larger in diameter than the roller. Additionally, the roller and the mandrel are aligned by metal slims, which makes sure that the rubber ring does not push the bushes too much as it could, avoiding unevenly distributed pressure during rolling. The pressure distribution is checked by the pressure sensitive film. Fig 5.3 shows the results of pressure sensitive films that indicates unevenly distributed pressure (left) and evenly distributed pressure through the width direction (right).

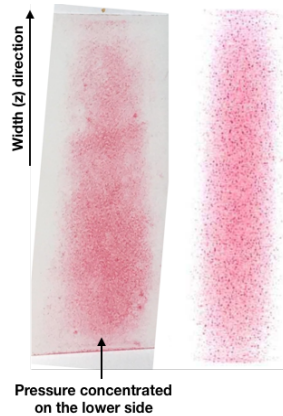


Figure 5.3 Results of pressure sensitive film: unevenly distributed pressure (left) and evenly distributed pressure (right)

The sample manufacturing has been explained in Appendix 1.1. There are five different sizes of the rubber ring. Their numbering is listed in table 5.1. The unstretched rubber ring has an inner diameter the same as the roller's diameter (70 mm) while the stretched rubber ring has a smaller inner diameter. The intention is to have sufficient friction to prevent lateral movement. However, a too tight rubber ring is difficult to use DIC to measure the strain field and also is sensitive to cracks. Therefore, the inner diameter is selected based on the compensation between having enough friction and application easiness.

No.	Stretched/ Unstretched	thickness [mm]	Inner diameter [mm]
1	Stretched	5	67
2	Stretched	10	65
3	Stretched	15	65
4	Unstretched	5	70
5	Unstretched	10	70

Table 5.1 Numbering of the five sizes of the rubber ring

## 5.2 Force calibration of the pneumatic cylinder

Before the validation of the FEA analysis, the force applied by the pneumatic cylinder needs to be calibrated as the cylinder applies air pressure. This is done by finding the relation between the applied force and the pressure of compressed air used in the pneumatic cylinder. As a result, compaction force can be adjusted by changing the air pressure using the pressure regulator.

### 5.2.1 Test procedure

The test setup is shown in Fig 5.4. The compaction force is measured by a load cell that is pressed by the pneumatic cylinder under different air pressure. Two loading cycles are used to check the residual force. The air pressure ranges from 0 to 6 bar, as limited by the pneumatic cylinder. The air pressure is slowly increasing and decreasing. The force and air pressure values are read after around 5 s until the pressure is stabilized.

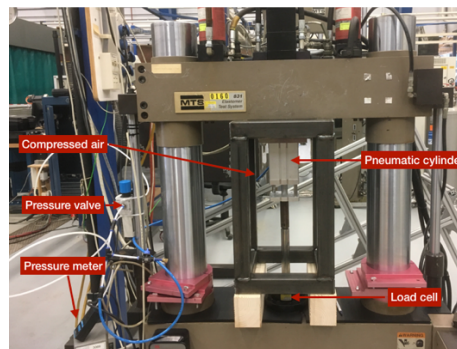


Figure 5.4 Experimental setup of the force calibration for the pneumatic cylinder

### 5.2.2 Results & discussion

The results of the force-air pressure curve are plot in Fig 5.5 (left). It can be seen that the curves of two loading cycles are almost overlapped except for the loading curves below 2.5 bar of the air pressure, indicating the residual force only affects the loading under small air pressure, which might be an issue if small compaction force ( $< 500$  N) is applied. 2nd loading has slightly smaller force than that of the 1st loading under the same air pressure ( $< 2.5$  bar) due to residual force. Therefore the 1st curve will be used to calculated the compaction force from the air pressure. The 1st and curve is fitted to polynomial equation. The results are presented in the Fig 5.5 (right) and compared with experimental data.

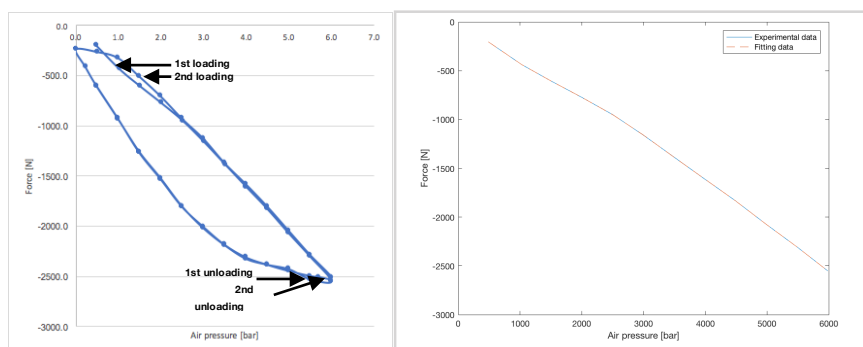


Figure 5.5 Force - air pressure curves of the pneumatic cylinder under two loading cycles: experimental data (left) and fitted data (right)

### 5.3 Validation of rubber's displacement/strain field

The rubber's vertical displacement/strain field under various compaction forces is one of the most important variables obtained from FE models, since it directly affects the contact pressure as described in hyperelastic material model. The compaction force is calibrated in the previous section. In order to validate the vertical displacement/strain field, digital camera correlation is applied to measure the displacement/strain field in both static contact and rolling process. This section consists of three parts: sample preparation, test procedure and result & discussion.

#### 5.3.1 Sample preparation

The speckle pattern needs to be painted on the rubber's outer surface so that the contrast ratio is increased and thus the displacement/strain distribution is more detectable by cameras than the rubber's original blue color. The unstretched rubber and stretched 5 mm-thick rubber ring are painted without the roller because they can be later applied along the roller before testing without damaging the paint. However, the rubber with other sizes need to be painted after fit them along the roller as shown in Fig 5.6. Otherwise the paint get broken if paint the rubber first and then stretched it to fit to the roller.

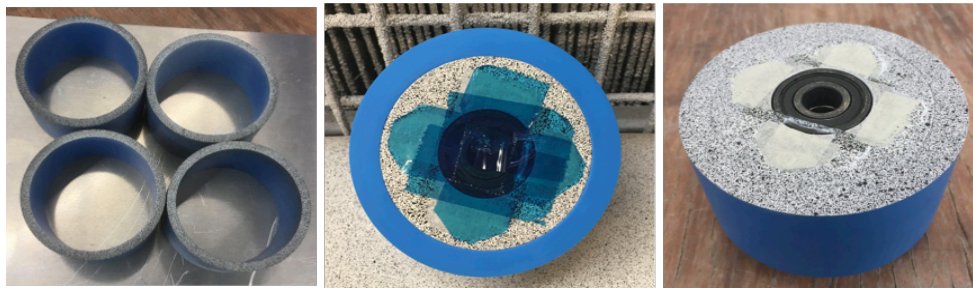


Figure 5.6 Paint the speckle pattern to stretched 5 mm-thick rubber rings (left), the roller covered with stretched 10 mm-thick rubber before (middle) and after paint (right)

#### 5.3.2 Test procedure

The test setup is shown in Fig 5.7. Two cameras are used to capture the vertical strain/displacement field on the rubber's outer surface under various compaction forces. The force range is selected such that the maximum vertical logarithmic strain remains in the elastic range (below 0.35) as illustrated in section 3.1.2. In addition, the maximum contact pressure should not exceed 2.5 MPa as limited by measuring rang of the pressure sensitive film (LLW), which will be discussed later. Accordingly, seven load levels are chosen and listed in table 5.2. Force per width is obtained from dividing the applied force by the rubber width (46 mm). The displacement/strain distribution is measured in static contact and in rolling process, separately. All seven loads will be applied to static contact. The force range (276 - 1104 N) is selected according to the measure range of the pressure sensitive film (1 MPa - 2.5 MPa), which will be further discussed in the next section. Owing to the power limitation of motor, the first three loads are selected such that they are covered within the force range (0 - 552 N) under which the mandrel is able to rotate by the motor. The rest load levels are evenly distributed from 552N to 1104 N. As explained before, two bushes are used to prevent the rubber from moving out. However, in order to capture all the paint attached to rubber's outer surface, one bush needs to be removed. Therefore, measurements under static loads are applicable for all rubber dimensions while measurements during rolling is only applicable for stretched rubber

since unstretched ones are moving out immediately after rolling.

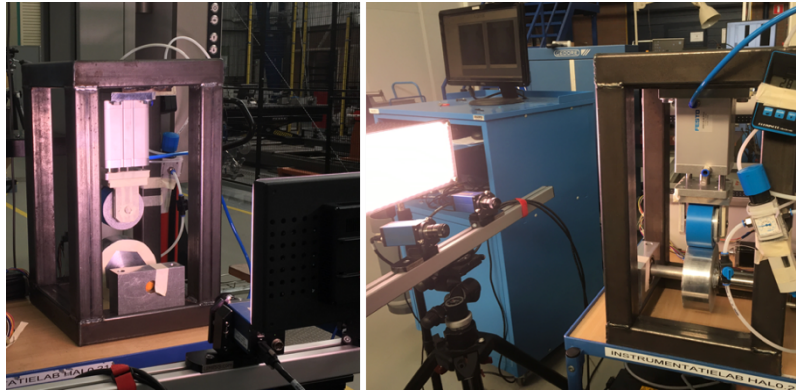


Figure 5.7 Experimental setup of DIC

No.	Force [N]	Force per width [N/mm]	Air pressure [mili bar]	Status
1	276	6	647	static + rolling
2	414	9	968	static + rolling
3	552	12	1344	static + rolling
4	644	14	1616	static
5	736	16	1893	static
6	920	20	2418	static
7	1104	24	2873	static

Table 5.2 All seven load levels that are used for DIC measurement

One of the difficulties of using DIC in this case is to define the initial status (zero displacement/strain field). Ideally, the initial status should be when the rubber-covered roller is touching the mandrel without any contact force, which, however, cannot be achieved by the pneumatic cylinder. Therefore, when the roller is pushed down, small air pressure is used to make it rebound and then fall down slowly by its gravity, introducing a pre-load (shown in Fig 5.8). Furthermore, the maximum rolling speed is determined by the camera setting, such as frames per second (FPS) and exposure time. Hence, the speed of 25 mm/s is used according to the maximum FPS of 9 and the exposure time is adjusted to 19ms based on the light. In addition, the detectable rolling angle is restrained to around 150° due to the fact that the paint hidden in the bracket cannot be captured by DIC, as explained in Fig 5.9.

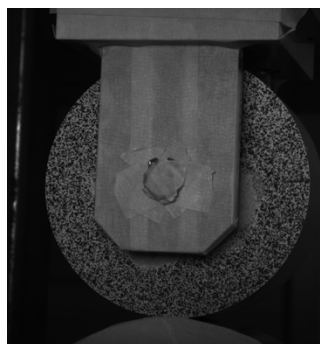


Figure 5.8 Initial status of one rubber sample (15 mm thick, No.4)

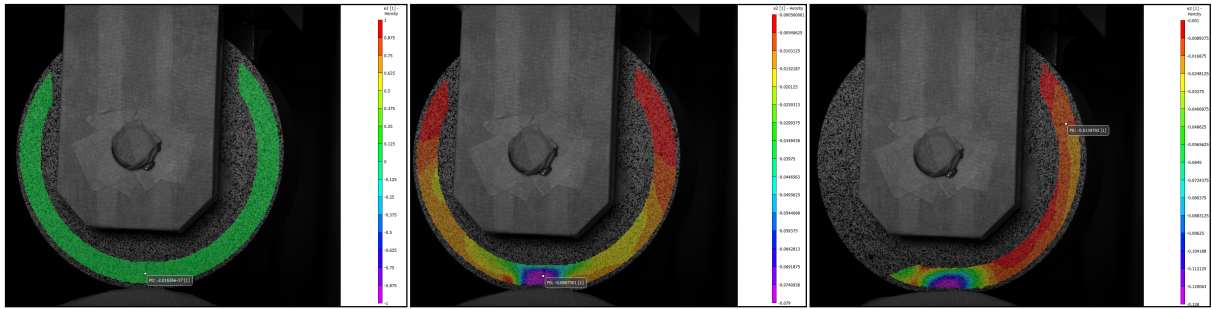


Figure 5.9 Vertical logarithmic strain distribution of 10 mm-thick rubber: initial status (left), start to rotate (middle) and end of rolling (right)

The DIC results are analyzed by Vic 3D 8<sup>®</sup>, a commercial digital image correlation software. Firstly, the area of interest (ROI) should be defined and further split into evenly spaced grids (Pan, Qian, Xie, & Asundi, 2009) as shown in Fig 5.10. By default, the grid size (subset size) of 29 and the integration step of 9 are used in Vic 3D 8. The displacement at grid points are calculated by tracking the same locations of images before and after deformation (Pan et al., 2009). Therefore, the displacement field and strain can be obtained.

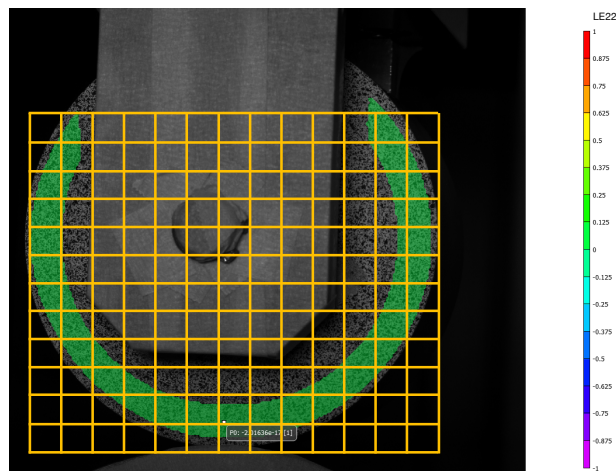


Figure 5.10 The grid in the area of interest (ROI) of the undeformed image (reference image)

### 5.3.3 Results & discussion

The displacement/strain distribution is measured by DIC in both static contact and rolling process. In static contact, the distribution of vertical displacement (U2) and vertical logarithmic strain (LE22) through thickness are compared with FEM results. Furthermore, the results of U2 and LE22 under different load levels are also compared. During rolling process, the comparison LE22 distribution is made between DIC and FEM.

#### *U2 and LE22 distribution through thickness*

The distributions of U2 and LE22 through thickness under the same load (736N) for all 5 different sizes of rubber are obtained from Vic 3D 8. As shown in Fig 5.11, the overall U2 distribution in the contact region in DIC is compliant with the results in 2D and 3D FE models. To be more specific, the U2 distributions through the mid-line ( $\overline{AB}$ ) in the lower half of rubber are compared with that in 2D model (along  $\overline{CD}$ ) and that in 3D model (along  $\overline{EF}$ ). On the left, 5 or 9 points are evenly selected from the mid line ( $\overline{AB}$ ), where 5 points are used for 5 mm-thick rubber and 9 points are used for 10 and 15 mm thick rubber. Fig 5.12 plots the averaged U2 results of DIC with error bars, where the averaging method is discussed in section 3.1.1. The U2 distribution of 2D and 3D FE models are also included in Fig 5.12, where the results are along the mid-line  $\overline{CD}$  in 2D FEM (Fig 5.12 middle) and  $\overline{EF}$  on the outer surface in the 3D FEM as shown in Fig 5.12 (right). In addition, the DIC results are not available along the rubber edges due to the paint inconsistency. Hence, the results locations are calculated based on the measured the inner diameter of the results (Fig 5.11 left) and the coordinates of the selected points.

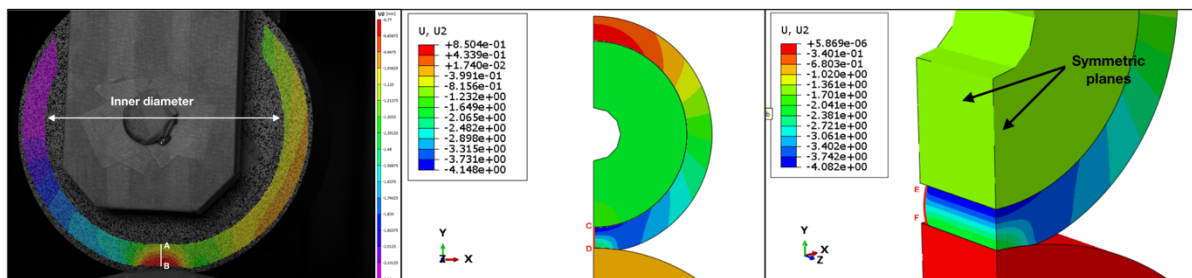


Figure 5.11 Location of the U2 and LE22 results in DIC (left), 2D FEM (middle) and 3D FEM (right)

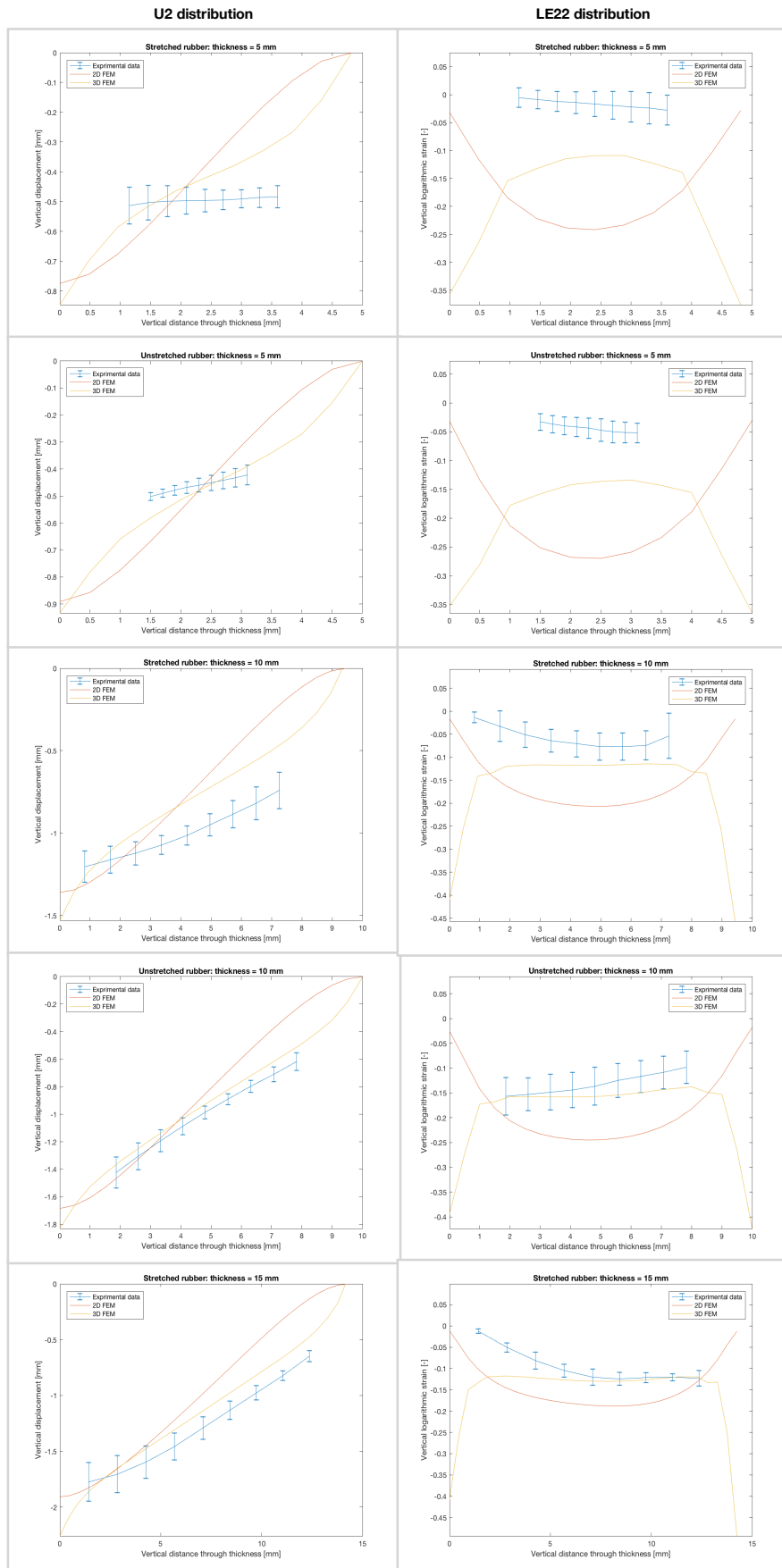


Figure 5.12 U2 (first column) and LE22 (second column) comparisons of 5 different rubber sizes (in each row) between DIC, 2D and 3D FEM static results

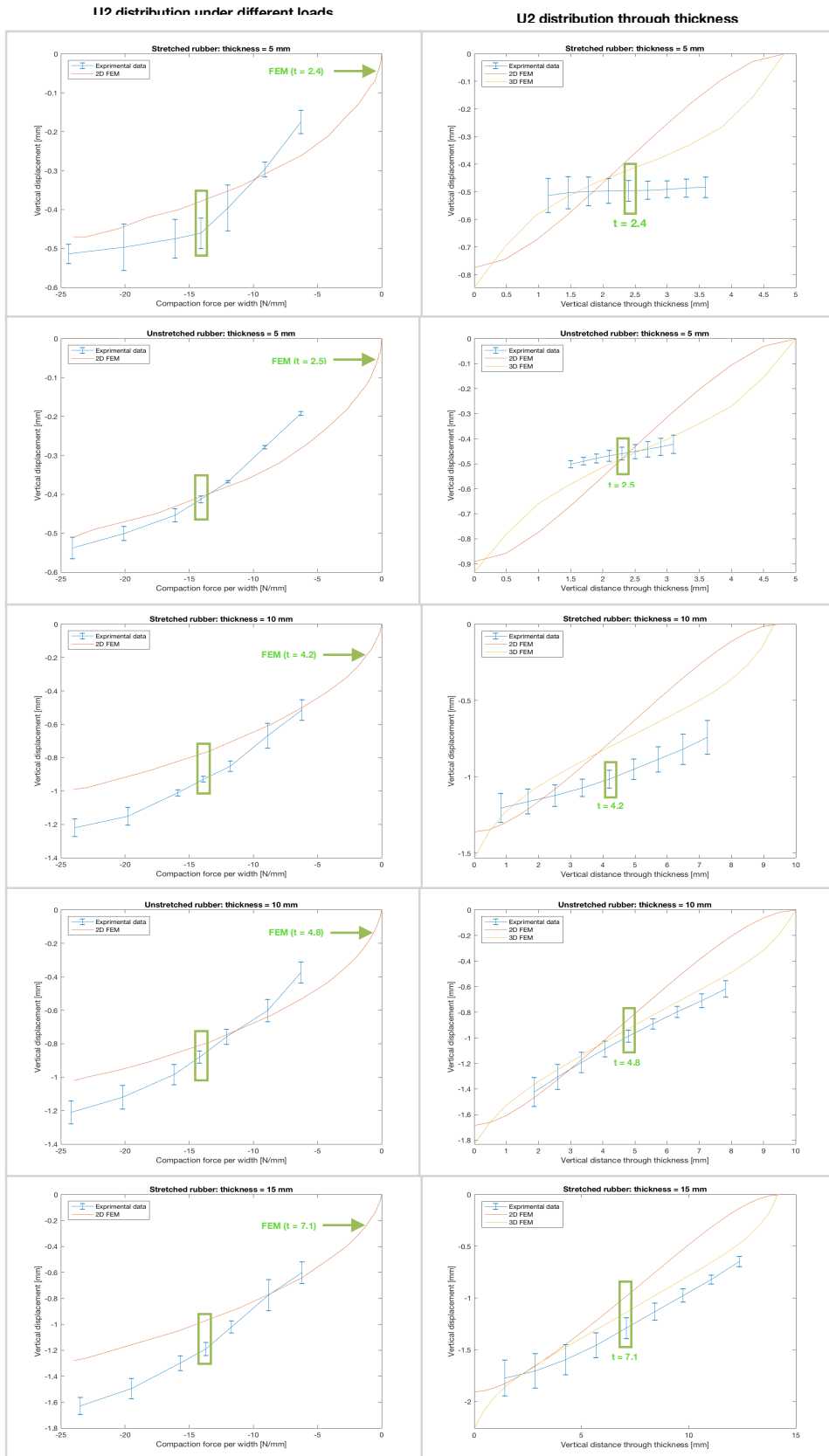


Figure 5.13 U2 distribution under different loads (first column) and through thickness (second column) of 5 different rubber sizes (in each row) between DIC and 2D FEM static results

Comparing 2D and 3D FEM results, the U2 distributions are similar while the LE22 values of 3D FEM are smaller in the mid-thickness. This is due to the lateral deformation as discussed in section 4.2.1. This difference becomes less when the rubber thickness is increasing because of less deformation occurs for thicker rubber under the same load. Furthermore, there are two peaks of LE22 on the sides in 3D FEM results that exceeds the input range of the material data, which can be ignored since the plasticity is not included in material properties.

Comparing the U2 distribution along thickness (y) direction for the stretched rubbers with different thicknesses, U2 distribution is barely detected in DIC for 5 mm-thick rubber and it levels off to the U2 value at the mid-thickness instead. However, when the rubber thickness increase to 10 and 15 mm, the U2 distribution is more detectable through the thickness and the results are closed to that of 3D FEM. Generally, 3D FEM underestimates the U2 distribution due to the pre-load exists when the rubber-covered roller presses the mandrel. As discussed in the previous section, zero displacement/zero strain is defined under a smaller load, which is considered as a pre-load.

Comparing the LE22 distribution of the stretched rubbers with different thicknesses, LE22 distribution in DIC is almost zero for 5 mm-thick rubber due to the leveled off U2 distribution. When the thickness increase to 15 mm, the LE22 distribution is comparable to that of 3D FEM.

Comparing the results of stretched and unstretched rubber, the latter has more repeatable results and closer to 3D FEM prediction than the former, especially for the 10 mm-thick rubbers. The reason is probably because of the less interaction between the paint and rubber's outer surface in unstretched rubber. When spraying the paint, the unstretched rubber is in a stress-free condition while the tension exists in paint of the stretched rubber before testing. Nevertheless, the results between stretched and unstretched rubber are comparable, which is complies with the FEM results.

#### *U2 comparisons under different loads*

The U2 results of the mid-point along the mid-line ( $\overline{AB}$  in Fig 5.11 left) under seven different load levels are plotted for all 5 rubber dimensions separately in the first column of Fig 5.13. The FEM results at the corresponding location are marked in the second column of the Fig 5.13, which is not necessarily the mid-point through the thickness. And the U2 results at that point under different loads of the 2D FEM are also plotted together with the DIC results in the first column of Fig 5.13.

Generally, the U2 trends of different dimensions are compliant with the 2D FEM results. 2D FEM indicates a linear U2-compaction force relation. However, the DIC results are smaller under small loads due to the residual force of the pneumatic cylinder as indicated in the force validation curve shown in Fig 5.5. In small load level, less force is applied under the same air pressure, leading to less U2. On the other hand, the U2 - force/width curves are almost parallel to FEM results but have larger U2 under the same Force/width, which can be explained by two reasons. The first reason is the pre-load in the initial status of the testing. Hence, the real load should include the pre-load and thus be higher than that is calculated from the air pressure in the pneumatic cylinder. The other reason is due to the edge effects, which is the difference between 2D and 3D FE models, representing the U2 results in the mid-plane and outer surface, respectively.

#### *LE22 variation during rolling*

Fig 5.14 compares the LE22 distribution between DIC and 2D FEM before and after rolling. The general trends in DIC are compliant with that in 2D rolling FE models. The averaged LE22 results at the mid-point of the 10 mm-thick rubber along the mid-line (*i.e.*  $\overline{AB}$  in Fig 5.11 left) are plotted during rolling for three different load levels, as illustrated in Fig 5.15. The results of 3D FEM at the corresponding locations are also plotted in Fig 5.11 at the beginning of rolling since those 3D FE models are static contact models. 3D FEM over predicts the LE22 at rolling

time = 0, which is discussed before. However, LE22 increases in the rolling initiation phase and gets stable at a higher value during rolling. However, 2D rolling model shows a constant LE22 at the corresponding location at the mid-plane during rolling. The increment is probably due to the edge effects and cannot be explained by 2D rolling model.

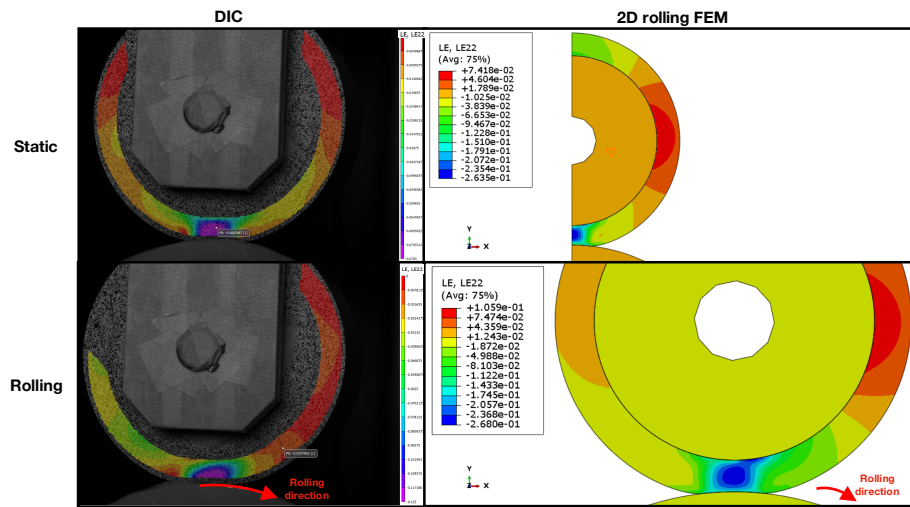


Figure 5.14 Comparison of the LE22 distribution between DIC and 2D FEM before and during rolling

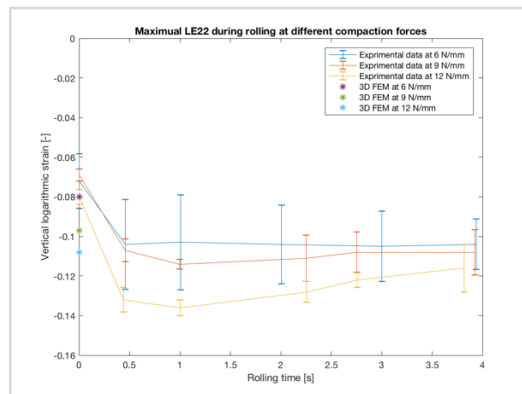


Figure 5.15 Averaged LE22 at the mid-point along the mid-line under different loads during rolling

## 5.4 Validation of contact pressure

The contact pressure between rubber and mandrel is one of the most important variables obtained from FE models, since it directly affects intimate contact, which is the prerequisite to good bond quality as stated in literature study. In order to validate the contact pressure, the pressure sensitive film (Fuji Prescale Pressure Measuring Film<sup>®</sup>) are used to measure the contact pressure between the rubber and the mandrel. The type of LLW (super low pressure range) is used with the pressure range from 0.5 - 2.5 MPa. As mentioned before, the pressure film is sensitive to the scanning method and room condition, including room temperature and humidity. Therefore, a calibration process needs to be made to find the relation between pressure and color density. Then, the contact pressure of various rubber sizes under different loads is measured and the results will be discussed comparing to FEM results.

### 5.4.1 Calibration of the pressure sensitive film

The calibration of the pressure sensitive film has been conducted based on previous work (Bachus et al., 2006; Brulotte et al., 2012; Liggins et al., 1994, 1992). The calibration setup is presented in Fig 5.16 (left), including a calibration pin, a ball bearing, a supporting pin and a load cell. The ball bearing is used to reduce the eccentric loading caused by the misalignment of those two pins (Liggins et al., 1992). The pressing surfaces are finely ground (Bachus et al., 2006) since the pressure film is found to be extremely sensitive to the surface level fluctuations (Liggins et al., 1992). Fig 5.16 (upper right) shows a stain image under the force of 1300N. However, the color is not uniformly distributed. Compared to a stain image from literature (Bachus et al., 2006) (Fig 5.16 lower right), the pin edge is distinguishable. The stain size is measured to be around 25 mm in diameter while the diameter of the calibration pin is 50 mm, indicating a protruding surface of the calibration pin. It is difficult to obtain the flat surface of such a large pin by grinding. The pin used in literature (Bachus et al., 2006) only has a diameter of 23 mm. Therefore, extra procedure is required to obtain the contact area in order to find the applied pressure.

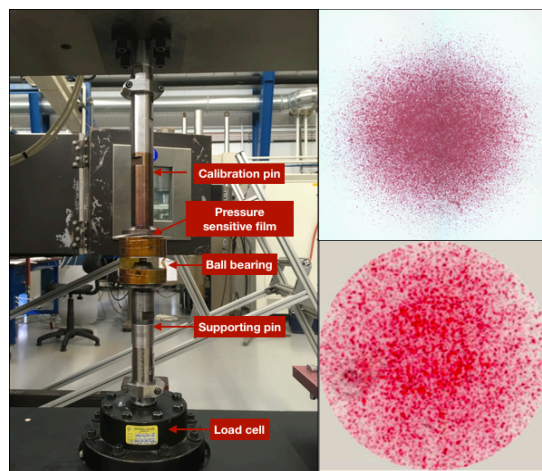


Figure 5.16 Calibration setup (left) and stain image under 1300 N (upper right) and from literature (lower right) (Bachus et al., 2006)

When measuring the pressure, the pressure sensitive film should be pressed at a known pressure. The stain image is then scanned by Keyence microscope and the color density map can be transformed to grey-scale mode (256 grey-level), as shown in Fig 5.17. Note that several images are stitched together by Keyence (1px = 10.9 $\mu$ m) since the entire picture cannot be scan at once even at the smallest magnification factor (x 20). The detailed information of the image processing is included in appendix 3. As a result, the relation between color density and pressure are obtained. In order to capture the momentary pressure, a load profile is suggested in the manual, which is ramping up to the desired load level in 5 s and held for 5s. Accordingly, stain images are obtained by the load control. 12 different load levels are used, covering the pressure range from 0.25 to 3.5 MPa. Additionally, three measurements are made for each load.

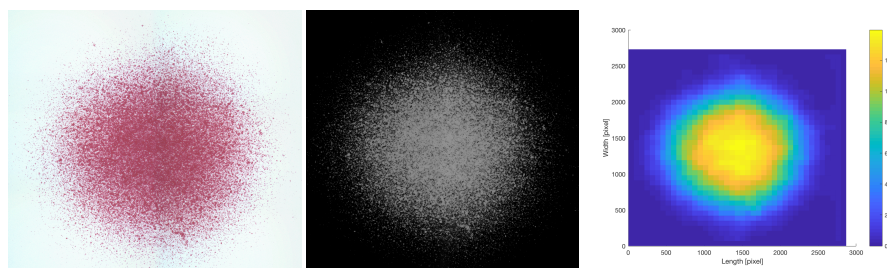


Figure 5.17 Stain image scan (left), transformation to grey level (middle), and inversed grey level map (right)

Uniform pressure can be assumed and thus the uniform color density is found by averaging the stain image. The averaged pressure can be obtained by applied force dividing by the contact area. However, the stain edge is difficult to be identified to calculate the contact area and averaged color density since the average value is significantly influenced by the minimum color density. Therefore, two thresholds of the grey level are used to filter out the region where the grey level is smaller than the threshold to calculate the contact area (ratio 1) and averaged color density (ratio 2), respectively. Those two thresholds are written in terms of the ratio to the maximum value. For instance, Fig 5.18 shows two contours that are filtered by those two thresholds. Threshold 1 (ratio 1) represents the contact area (blue edge) and threshold 2 (ratio 2) shows the region (green edge) used to average the grey level values.

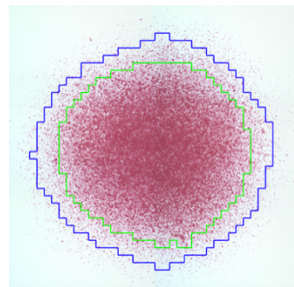


Figure 5.18 Stain image with two contour filtered by two thresholds: ratio 1 = 0.08 (blue) and ratio 2 = 0.3 (green)

Given a calibration curve, the force can be calculated by integrating the pressure map. Therefore, ratio 1 can be determined if ratio 2 is known. Initially, the values of ratio 2 are selected to be 0.3, 0.4, 0.5. The corresponding ratio 1 for each ratio 2 can be obtained in a similar way explained before. As a result, three ratio combinations are found and listed in table 5.3. Calibration curves of three ratio combinations are plotted in Fig 5.19 (left) and the corresponding integrated force curves are compared with applied force in Fig 5.19 (right). As can be seen, the calculated force get saturated after test No.8. Before test No.8, the calculated force of combination 1 matches the applied force curve most and always smaller than the applied force since the calculated pressure is smaller than applied pressure, due to the fact that the pressure film overestimate the contact area for high loads in larger loads as stated by Bachus *et al.* (Bachus et al., 2006). Therefore, it has been decided to use 0.08 for ratio 1 and 0.3 for ratio 2.

Combination No.	Ratio 1	Ratio 2
Aim	Contact area	averaging the color density
1	0.08	0.3
2	0.1	0.4
3	0.1	0.5

Table 5.3 Three ratio combinations found by comparing applied and calculated force

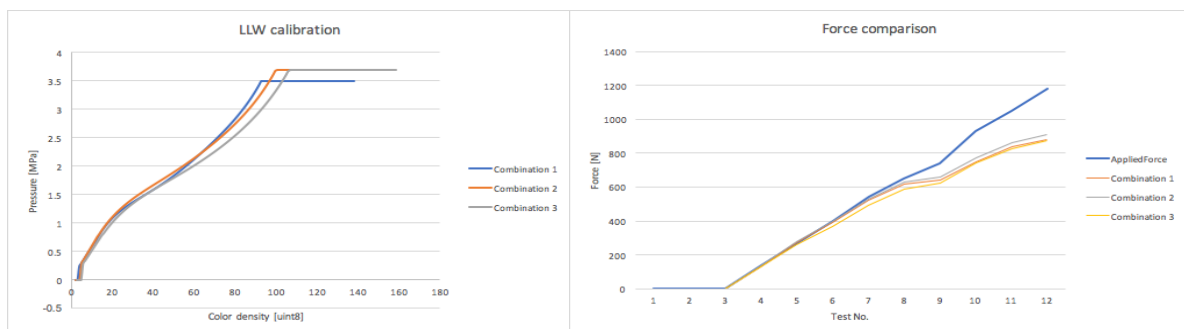


Figure 5.19 Calibration curves of three ratio combinations (left) and the comparison between the corresponding calculated forces and applied force; Room condition: 22.8°C, RH% = 34%

## 5.4.2 Test procedure

Pressure measurements are performed in static contact and during rolling process. In static contact, roller is pressed without the pressure films and a certain compaction force is adjusted by the pressure regulator. Then, release the roller and place the pressure film on top of the mandrel. After that, roller is pressed at a selected load, hold for 5 seconds and released manually. During rolling process, the films are pressed after mandrel rotates almost one round since pressure get stable after a contact initiation phase as discussed before. Testing setup is shown in Fig 5.20. Pressure sensitive films are taped along one side. Then, roller is pressed and the compaction force is adjusted by the pressure meter. It is suggested to stretch the films before they are pressured by the roller for better contact. Otherwise, two films are partially contacted, causing inconsistent color density.

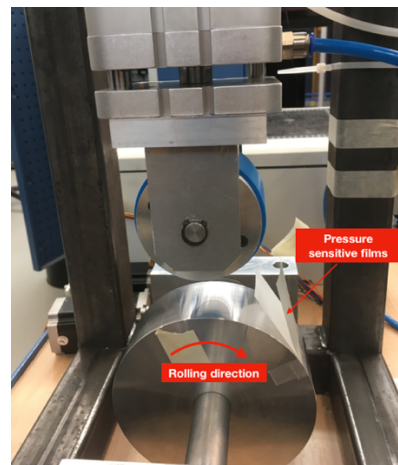


Figure 5.20 Experimental setup for pressure measurement

The room condition is closed to that of calibration and thus there is no need to calibrate the pressure sensitive film again. In the data sheet, room condition is divided to four regions as shown in Fig 5.21 and four calibration curves are provided corresponding to each region. The room conditions of calibration (marked as a red point in Fig 5.21) and experiment (marked as a blue point in Fig 5.21) are closed to each other and both of them remains in the region D. As a result, the calibration curve made in the room condition (22.8°C and 34% of relative humidity) is applicable to the experiment where the room condition is 23.1°C and relative humidity (RH) is 39%.

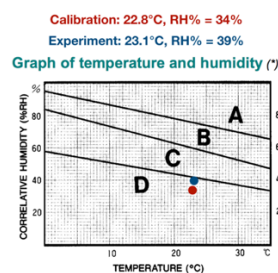


Figure 5.21 Comparison of room condition between calibration and experiment of pressure measurement (RH stands for relative humidity)

## 5.4.3 Results & discussion

### Pressure in the static contact

The pressure map is calculated based on the scanned pressure films. Image processing is explained in Appendix 3. The pressure map of 5 mm-thick rubber under two loads are

presented in Fig 5.22, together with 3D FEM results. The results of maximum pressure (CPRESS) and contact length obtained from pressure film and FEM are listed in table 5.4. Due to the symmetric condition, only a quarter of the rubber is simulated in FEM, the corresponding area is marked in the pressure film results as red dashed rectangular. It can be seen that the pressure results obtained from the pressure film are larger than that in FEM in both 8 and 12 N/mm loads. This is probably due to the impact existing when the rolling is pressing the pressure films, which causes more color releasing in the pressure film than slowly increasing the force in 5 s as made in calibration curve. Furthermore, it is difficult to manually release the pressure 5 s after pressing. In fact, the pressure is held for more than 5 s (around 6 s), which might also contribute to higher pressure. In addition, the pressure results obtained from the pressure sensitive films show that the maximum pressure distributed in blocks. This is because of non-uniform light during the image stitched process.

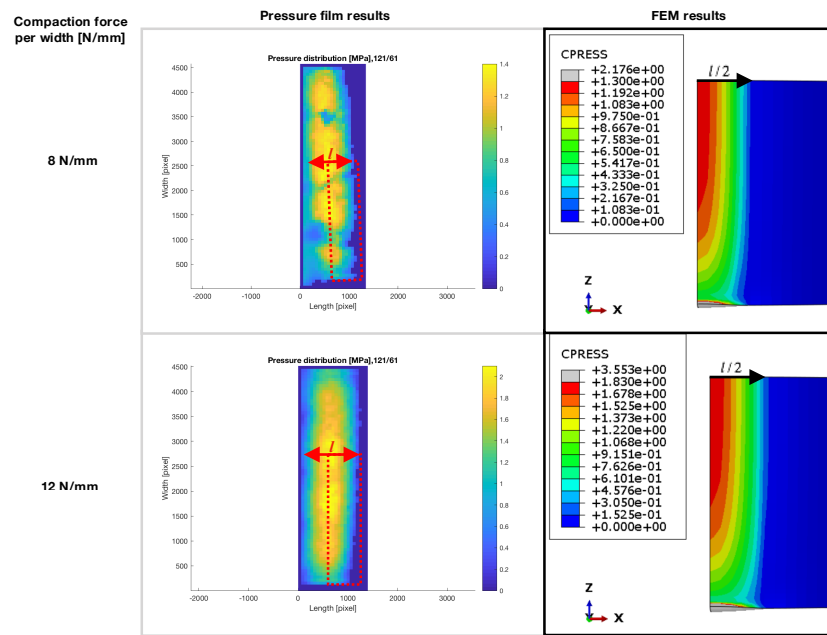


Figure 5.22 Pressure comparison between experimental and FEM results under two loads

Compaction force per width [N/mm]	Pressure map		3D FEM results	
	Contact length [mm]	Maximum pressure [MPa]	Contact length [mm]	Maximum pressure [MPa]
8	7.95	1.37	6.59	1.29
12	9.29	2.16	7.79	1.83

Table 5.4 Maximum pressure and contact length obtained from the pressure films and 3D FEM under two different compaction forces

As discussed in section 4.3.2, the contact length is defined as the circumferential length ( $l$ ) where the pressure is larger than zero, as shown in Fig 5.22. The contact lengths obtained from pressure film are manually determined based on pressure map, which is around 17% larger than that in FEM for both of the compaction forces. Two reasons explained in the previous paragraph, including the effect of impact and longer time for color material to release. In addition, this difference of contact lengths might also be contributed to the error of measuring the length by pressure films since pressure film can overestimate the area in larger loads as stated by Bachus *et al.* (Bachus et al., 2006). Furthermore, the increment of contact length is observed for larger compaction force in pressure film results, which is consistent with that in FEM.

## Pressure during rolling

The pressure maps measured during rolling for 5 mm-thick stretched and unstretched rubber are compared in Fig 5.23 under two load levels. As mentioned before, the pressure sensitive films are taped on one side to the mandrel and stretched on the other side by hands when pressing. It should be noted that the results for unstretched rubber are obtained with manually pulling the corners, as indicated by the two corners of bright yellow in the upper right of Fig 5.23. However, pressure films for stretched rubber are taped on all edges and pulling force is not applied. It can be seen that the pressure measured with pulling force is more uniform comparing to the one measured without pulling. Without pulling the films, two films have difficulties in following the curvature of the mandrel since they are PET- based (polyethylene terephthalate) and are rather stiff. Thermoplastic tape is even stiffer especially for the 0° tape. Therefore, the role of pulling the films acts as the tape tension, making them in contact more uniformly with each other. Similar to static pressure measurement, pressure concentrated in blocks is caused by non-uniform light during the image stitching process.

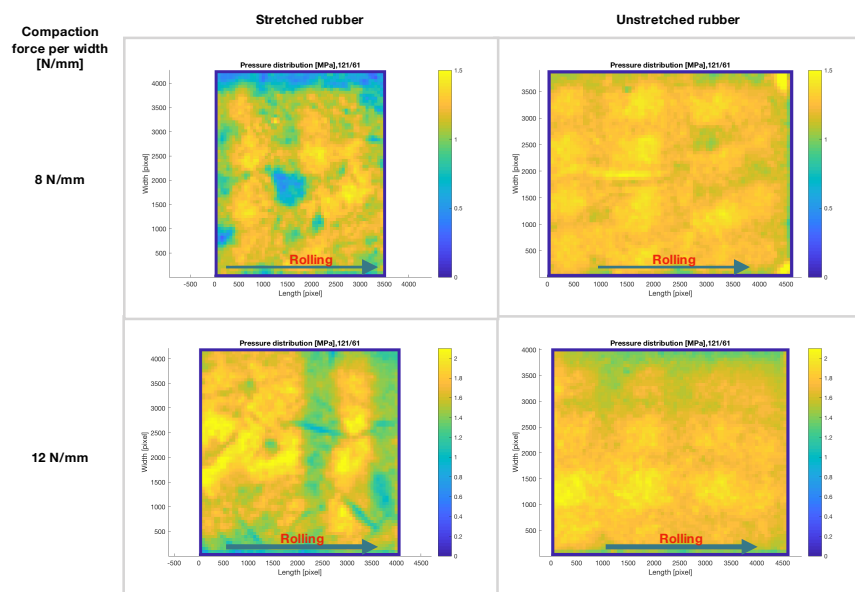


Figure 5.23 Comparison of pressure map for 5 mm stretched (first column) and unstretched (second column) rubber under two loads (in rows)

Comparing to stretched and unstretched rubber under the same load, stretched rubber has slightly higher pressure value compared to that of unstretched rubber. It seems to be compliant with the conclusion made in section 4.3.3 that the pressure of unstretched rubber is slightly smaller than that of stretched rubber due to less constraint. However, this difference might be also due to the influence of non-uniform light. Hence, it is difficult to draw a conclusion that the pressure of unstretched rubber is slightly smaller than that of stretched rubber. Furthermore, pressure results of the stretched rubber are similar between static and rolling process. The small difference (0.14 MPa) indicated by FEM is too small to be detected.

## 5.5 Conclusion

Experiments have been conducted to validate the FE models described in chapter 4, including the validation of vertical displacement/strain field by digital image correlation (DIC) and contact pressure between rubber and mandrel by pressure film. The vertical displacement /strain field on one side of the rubber is measured by DIC in both static contact and rolling process for different rubber dimensions under different load levels. Firstly, the vertical displacement ( $U_2$ ) distribution through the rubber thickness generally matches well with the results of 3D static

FEM. For thinner rubber, the U2 distribution tends to level off to the value at the mid-thickness since the edge (around 1.5 mm) cannot be detected by DIC. When the rubber thickness increase to 10 and 15 mm, the U2 distribution is more detectable through the thickness. Secondly, the distribution of vertical logarithmic strain (LE22) is only comparable with results of 3D FEM for 15 mm rubber. Less LE22 distribution is observed for thinner rubber due to the leveling off of the U2 distribution. Thirdly, the U2 difference of stretched and unstretched rubber is too small to be distinguished due to the DIC limitations. Unstretched rubber is painted in a stress-free condition and thus have more repeatable results than that of stretched ones. However, stretched rubber is painted after fitted it to the roller. Hence, the results are less repeatable due to the interaction between the paint and rubber's outer surface. As a result, the subtle difference cannot be verified by DIC.

The contact pressure between rubber and mandrel are measured by pressure sensitive film under two different loads for 5 mm-thick stretched rubber in static and rolling process. In the static contact, 3D FEM underestimates the contact pressure by 9%, probably due to the impact when roller is pressing the mandrel by the pneumatic cylinder while the force is gradually increase to the desired value during calibration. During the rolling process, the pressure value is comparable to that in static contact. More uniform pressure can be obtained if the films are taped on one side and stretched on the other side during pressing. The influence of stretching the tape is similar to tape tension since the pressure sensitive films are PET-based and they are rather stiff, but the thermoplastic tape is even stiffer. In a word, pressure distribution is validated in static contact and the FEM results are comparable with experimental data. The difference between stretched and unstretched rubber cannot be distinguished experimentally. However, the rubber with pre-stretching force is preferred to unstretched ones since it can prevent rubber from moving out and more tolerance is allowed for roller-mandrel misalignment.

As a result, 2D and 3D static contact models can be validated directly by experiment while 2D rolling model can only be validated indirectly. 3D static model can be validated by measuring the vertical logarithmic displacement/strain (U2/LE22) on one side of rubber by DIC and contact pressure (CPRESS) in the contact area by pressure film. The 2D static model only captures the LE22 in the mid-plane of the testing setup and thus cannot be validated by DIC directly. However, it could be validated based on the validation of the contact pressure measured by pressure film. 2D rolling model cannot be validated directly based on the results of DIC and pressure film. On one hand, the LE22 field during is captured on one side of rubber, which increase in the initiation phase and become stabilized, while LE22 is constant in 2D rolling model. The initiation phase is observed in 2D rolling model by changes of other variable, such as maximum CPRESS and maximum COPEN along circumferential length. However, the increment of LE22 on the sides of rubber is probably due to the edge effects and cannot be captured in 2D rolling model. On the other hand, the pressure maps during rolling obtained from pressure film show comparable results to that in static contact. However, the exact values cannot be compared, owing to the small variation in the pressure value due to the influence of non-uniform light during scanning. As mentioned, the difference of the maximum CPRESS between 2D static and 2D rolling model is rather small and it might not be captured by pressure film under small compaction force, which is around 12N/mm in 2D models (full model) and correspondingly 552 N in total for the full width. Larger force cannot be applied during rolling, owing to the power limitation of the motor. The non-uniform light affects the pressure results during rolling. Nevertheless, 2D rolling model can be validated indirectly based on the comparable pressure results of pressure film between static contact and rolling process.



## 6 Conclusion

This work is focused on the pressure prediction using finite element method, followed by the experimental validation. The influences of compaction force, rubber thickness and with/without pre-stretching force on the pressure distribution are also discussed. Furthermore, the compaction force and rubber dimensions are optimized based on equipment limitations and pressure requirements. Several conclusions can be made as follows:

1. Material characterization of unfilled silicone rubber has been conducted by mechanical testing, including tensile, compressive and planar tension tests. However, the results of planar tension test cannot be used due to the limitation of experimental setup. Therefore, only the experimental data of tensile and compressive test is implemented in Abaqus and it is found that the hyperelastic material model of 3rd-order Ogden function can well describe the stress-strain behavior of rubber material.

2. Three finite element models are created to predict the pressure distribution between rubber and mandrel. Model reduction is required to save computational efforts. Plane strain condition can be applied since the width of the contact region is larger than the in-plane dimension, which makes it possible to simplify the 3D rolling process to a 2D rolling process. Furthermore, the 2D rolling process can be reduced to 2D static contact due to the negligible inertia effect caused by low rolling speed. Those assumptions are verified by two comparisons. The first comparison is made between 3D static contact model and 2D static contact model to confirm the plane strain assumption. In addition, 2D static model is able to predict the pressure distribution in the middle part (20 mm) through the out-of-plane direction, which covers the width of the thermoplastic tape (12.7 mm). Secondly, the 2D static model is compared with 2D rolling model and it is found that the inertia effect can be ignored. As a result, 3D rolling process can be simplified to 2D static process and the computational time is saved significantly from 9h in 3D static model to 1min in 2D static model.

3. The pressure distribution of different rubber dimensions under different compaction forces are predicted by the 2D FE models. The compaction force mainly increases the maximum contact pressure and only has a negligible effect on the contact length. Instead, the contact length is influenced more by rubber thickness, which is discussed later. In order to have a good bond quality, thermoplastic tapes are required to get intimate contact during the processing time, which requires a non-zero contact pressure. The processing time has more to do with the rolling speed, which is skipped in this study, while the non-zero pressure is determined by the contact length, which is defined as the circumferential length where the contact pressure value is larger than 0. Furthermore, thicker rubber has larger contact length but less maximum pressure under the same compaction force when comparing to thinner rubber. Therefore, a trade-off has to be made between the maximum pressure/contact length and the compaction force, which is constrained by the equipment, such as the limitations of pneumatic cylinder and motor power. In addition, there is no difference of the contact pressure with and without pre-stretching force in 2D static contact model. In 2D rolling model, unstretched rubber has slightly smaller pressure (0.14 MPa smaller) than that of stretched rubber. However, stretched rubber is preferred to unstretched rubber for more practical reasons. Stretched rubber allows for more tolerance of the misalignment of the roller and mandrel and prevents rubber from moving out.

4. A processing window of pressure distribution under various compaction forces and different rubber thicknesses is plot by FEA. The rubber dimension is selected based on the limitation of compaction force and the pressure requirement. For one thing, the compaction force is limited by the equipment, such as pneumatic cylinder and motor. For another, pressure range is determined by bonding theories based on the viscosity of thermoplastic tape. In the end, the range of rubber thickness can be obtained.

5. 2D and 3D static contact models can be validated directly by experiment while 2D rolling model can only be validated indirectly. 3D static model can be validated by measuring the vertical logarithmic displacement/strain ( $U_2/LE_{22}$ ) on one side of rubber by DIC and contact pressure (CPRESS) in the contact area by pressure film. The 2D static model only captures the  $LE_{22}$  in the mid-plane of the testing setup and thus cannot be validated by DIC directly. However, it could be validated based on the validation of the contact pressure measured by pressure film. 2D rolling model cannot be validated directly based on the results of DIC and pressure film. On one hand, the  $LE_{22}$  field during is captured on one side of rubber, which increase in the initiation phase and become stabilized, while  $LE_{22}$  is constant in 2D rolling model. The initiation phase is observed in 2D rolling model by changes of other variable, such as maximum CPRESS and maximum COPEN along circumferential length. However, the increment of  $LE_{22}$  on the sides of rubber is probably due to the edge effects and cannot be captured in 2D rolling model. On the other hand, the pressure maps during rolling obtained from pressure film show comparable results to that in static contact. However, the exact values cannot be compared, owing to the small variation in the pressure value due to the influence of non-uniform light during scanning. As mentioned, the difference of the maximum CPRESS between 2D static and 2D rolling model is rather small and it might not be captured by pressure film under small compaction force, which is around 12N/mm in 2D models (full model) and correspondingly 552 N in total for the full width. Larger force cannot be applied during rolling, owing to the power limitation of the motor. The non-uniform light affects the pressure results during rolling. Nevertheless, 2D rolling model can be validated indirectly based on the comparable pressure results of pressure film between static contact and rolling process.

## 7. Recommendation

1. This work concentrates more on the validation of displacement/strain field on one side of rubber than the validation of contact pressure since the contact of only one rubber thickness is measured. Future investigation could be pursued to measure contact pressure and contact length of different rubber thicknesses by pressure film to further validate the 2D static FE model.
2. The effects of pressing time on the color density of stain image could be further evaluated. The pressure sensitive film is calibrated in 5s increasing and holding of a known pressure. However, the pressuring time is much less when measuring pressure during rolling process. Hence, calibration could be conducted at a known pressure for different pressing time. Then, it could be decided whether the variation of color density in the stain image is sensitive to the speed range (around 100 mm/s) or not.
3. This work predicts the pressure distribution for the tape winding process at room temperature. More work could be done to characterize rubber at high temperature to have a reliable pressure prediction at the processing temperature (around 350°C). In hyperelastic material models, the material constants are *constant* in room temperature. Temperature-dependent material constants can be obtained from characterizing rubber under different temperature. Abaqus also enables temperature-dependent hyperelastic material models to solve more complicated coupled thermos-mechanical problems when simulating bonding process.
4. Pressure sensitive film cannot be used above 35°. Hence, other pressure measurement device need to be considered, such as digital pressure sensing devices (Bachus et al., 2006).
5. Tape tension, as imitated by stretching the pressure film during pressure measurement, also influence the pressure distribution in the contact area, which is worth to investigate in the future. Comparing to ATP and tape winding process, one of the main difference lies in the tape tension, which is continuous in tape winding process but not continuous in ATP. It is reported that in-situ consolidation is more successful in tape winding process than that in ATP. The reason could be contributed to the role played by tape tension. After winding several layers of thermoplastic tape to the mandrel as the substrate, pressure can be measured between rubber and thermoplastic tape with the tape tension, so that the influence of the tape tension can be studied.
6. The durability of compaction roller in in-situ consolidation remains an issue to work at the processing temperature of thermoplastic tape (around 350°C). Hard-plastic roller is used in ATP with in-situ consolidation. It has higher temperature resistant that can handle 350°C. However, hard plastic roller is expensive and they are worn often and replaced soon. Use rubber-metal roller combination is a cheaper alternative. The selected silicone rubber has relatively high temperature resistant compared to other types of rubber. However, it is suggested not to be use above 250° as stated in the data sheet, which is below the processing temperature. There are some options to lower the rubber temperature during in-situ consolidation process. Kapton tape is recommended to covered the rubber ring to prevent heat transfer. Also, some cooling air can be used.



# References

- ABAQUS, A. V. (2011). 6.11 Documentation, ABAQUS. Inc., Sunnyvale, CA.
- Abubakar, I. J., Myler, P., & Zhou, E. (2016). Constitutive Modelling of Elastomeric Seal Material under Compressive Loading. *Scientific Research Publishing*, 6(April), 28–40.
- Ageorges, C., Ye, L., & Hou, M. (2000a). Experimental investigation of the resistance welding for thermoplastic-matrix composites. Part I: Heating element and heat transfer. *Composites Science and Technology*, 60(7), 1027–1039.
- Ageorges, C., Ye, L., & Hou, M. (2000b). Experimental investigation of the resistance welding of thermoplastic-matrix composites. Part II: optimum processing window and mechanical performance. *Composites Science and Technology*, 60(8), 1191–1202.
- Ageorges, C., Ye, L., & Hou, M. (2001). Advances in fusion bonding techniques for joining thermoplastic matrix composites: A review. *Composites - Part A: Applied Science and Manufacturing*, 32(6), 839–857.
- Ageorges, C., Ye, L., Mai, Y.-W., & Hou, M. (1998a). Characteristics of resistance welding of lap shear coupons. Part I: Heat transfer. *Composites Part A: Applied Science and Manufacturing*, 29(8), 911–919.
- Ageorges, C., Ye, L., Mai, Y.-W., & Hou, M. (1998b). Characteristics of resistance welding of lap shear coupons. Part II. Consolidation. *Composites Part A: Applied Science and Manufacturing*, 29(8), 911–919.
- Aluminum Association, o. (1984). Aluminum: properties and physical metallurgy. ASM International.
- Bachus, K. N., DeMarco, A. L., Judd, K. T., Horwitz, D. S., & Brodke, D. S. (2006). Measuring contact area, force, and pressure for bioengineering applications: Using Fuji Film and TekScan systems. *Medical Engineering and Physics*, 28(5), 483–488.
- Bastien, L. J., & Gillespie, J. W. (1991). A non-isothermal healing model for strength and toughness of fusion bonded joints of amorphous thermoplastics. *Polymer Engineering & Science*, 31(24), 1720–1730.
- Batra, R. C. (1980). Rubber covered rolls - The nonlinear elastic problem. *Journal of Applied Mechanics*, 47(March 1980), 82–86. Retrieved from
- Batra, R. C., Levinson, M., & Betz, E. (1976). Rubber Covered Rolls - The Thermoviscoelastic Problem, a Finite Element Solution. *International Journal for Numerical Methods in Engineering*, 10(September 1974), 767–785.
- Benatar, A. ; Gutowski, T. G. (1986). Method for fusion bonding thermoplastic composites. *Thin Solid Films*, 18:1.
- Bourban, P. E., Bernet, N., Zanetto, J. E., & Månson, J. A. E. (2001). Material phenomena controlling rapid processing of thermoplastic composites. *Composites - Part A: Applied Science and Manufacturing*, 32(8), 1045–1057.
- Box, G. E. (1978). *Statistics for experimenters*. John Wiley and sons New York.
- Brulotte, X. G., Hubert, P., & Hojjati, M. (2012). Aspects of in-situ consolidation of thermoplastic laminates manufactured by Automated Tape Placement. In *International SAMPE Technical Conference*. Retrieved from
- Butler, C. A., Mccullough, R. L., Pitchumani, R., & Gillespie, J. W. (1998). An Analysis of Mechanisms Governing Fusion Bonding of Thermoplastic Composites. *Journal of Thermoplastic Composite Materials*, 11(4), 338–363.
- Chao, M and Gillespie Jr, J. (1994). The Influence of Healing and Bondline Thickness on the Mechanical Performance of Fusion-Bonded Thermoplastic Composite Joints. *Moving Forward With 50 Years of Leadership in Advanced Materials.*, 39(6), 2023--2037.
- Dolwichai, P. a. (2006). Hyperelastic Material Models for Finite Element Analysis with Commercial Rubber. *Technology and Innovation for Sustainable Development Conference (TISD2006)*.
- Duncan, B. C., Maxwell, A. S., Crocker, L. E., & Hunt, R. (1999). VERIFICATION OF HYPERELASTIC TEST METHODS Performance of Adhesive Joints Programme Project PAJ1 - Failure Criteria and their Application to Visco-Elastic/Visco-Plastic Materials. Retrieved from
- F. Yang, & Pitchumani, R. (2003). Nonisothermal Healing and Interlaminar Bond Strength Evolution During Thermoplastic Matrix Composites Processing. *Polymer Composites*, 24(2), 263–278.
- Formlabs. (2017). Retrieved from Datasheet of the grey material (GPG02): <https://formlabs.com/media/upload/XL-DataSheet.pdf>
- Fujifilm. (n.d.). Fuji. Retrieved from Fuji Prescale Pressure Measuring Film instruction sheet: LLW

- (Super Low Pressure Range): [https://www.fujifilm-mea.com/fileadmin/products/prescale/media/Two\\_Sheet\\_Type\\_for\\_Super\\_Low\\_Pressure\\_klein.pdf](https://www.fujifilm-mea.com/fileadmin/products/prescale/media/Two_Sheet_Type_for_Super_Low_Pressure_klein.pdf)
- Fukubayashi, T., & Kurosawa, H. (1980). The Contact Area and Pressure Distribution Pattern of the Knee: A Study of Normal and Osteoarthritic Knee Joints. *Acta Orthopaedica Scandinavica*, 51(1–6), 871–879.
- Gent, A. N. (2012). *Engineering with rubber: how to design rubber components*. Carl Hanser Verlag GmbH Co KG.
- Grove, S. M. (1988). Thermal modelling of tape laying with continuous carbon fibre-reinforced thermoplastic. *Composites*, 19(5), 367–375.
- Harris, M. L., Morberg, P., Bruce, W. J. M., & Walsh, W. R. (1999). An improved method for measuring tibiofemoral contact areas in total knee arthroplasty: A comparison of K-scan sensor and Fuji film. *Journal of Biomechanics*, 32(9), 951–958.
- He, P., Alfred, D., & Loos, C. (1985). Thermoplastic Matrix Composite Processing Model.
- Hinkley, J. A., Messier, B. C., & Marchello, J. M. (1997). Effect of pressure in thermoplastic ribbon thermal welding. *International SAMPE Symposium and Exhibition*, 42(Evolving Technologies for the Competitive Edge, Book 2), 1209–1216.
- Kikuchi, N. (1986). *Finite element methods in mechanics*. CUP Archive.
- Kikuchi, N. a. (1988). *Contact problems in elasticity: a study of variational inequalities and finite element methods (Vol. 8)*. siam.
- Kim, Y. H., & Wool, R. P. (1983). A theory of healing at a polymer-polymer interface. *Macromolecules*, 16(7), 1115–1120.
- Lee, W. II, & Springer, G. S. (1987). A Model of the Manufacturing Process of Thermoplastic Matrix Composites. *Journal of Composite Materials*, 21(11), 1017–1055.
- Levy, A., Heider, D., Tierney, J., Gillespie, J. W., Lefebure, P., & Lang, D. (2012). Simulation and optimization of the thermoplastic Automated Tape Placement (ATP) process. In *SAMPE 2012 - Baltimore* (p. 15p).
- Liggins, A. B., Hardie, W. R., & Finlay, J. B. (1994). Sterilization of Fuji pressure-sensitive film. *Medical Engineering and Physics*, 16(6), 496–500.
- Liggins, A. B., Stranart, J. C. E., Finlay, J. B., Rorabeck, C. H., & E.G.Little. (1992). Calibration and manipulation of data from Fuji pressure-sensitive film. *Experimental Mechanics*, 61–70.
- Lionetto, F., Dell'Anna, R., Montagna, F., & Maffezzoli, A. (2016). Modeling of continuous ultrasonic impregnation and consolidation of thermoplastic matrix composites. *Composites Part A: Applied Science and Manufacturing*, 82, 119–129.
- Logan, D. L. (2011). *A first course in the finite element method*. Cengage Learning.
- Lynch, F. D. E. S. (1969). *a Finite Element Method of Viscoelastic Stress Analysis with Application to Rolling Contact Problems*, (September 1968), 379–394.
- Mantell, S. C., & Springer, G. S. (1992). Manufacturing Process Models for Thermoplastic Composites. *Journal of Composite Materials*, 26(16), 2348–2377.
- Martins, P. A. L. S., Jorge, R. M. N., & Ferreira, A. J. M. (2006). A Comparative Study of Several Material Models for Prediction of Hyperelastic Properties: Application to Silicone-Rubber and Soft Tissues. *Strain*, 42(3), 135–147.
- Matlab. (2017). *2017 Documentation*, Matlab.
- Meunier, L., Chagnon, G., Favier, D., Orgé As, L., & Vacher, P. (2008). Mechanical experimental characterisation and numerical modelling of an unfilled silicone rubber. *Polymer Testing*, 27(6), 765–777.
- Miller, K. (2004). *Testing Elastomers for Hyperelastic Material Models in Finite Element Analysis*. Axel Products. Inc.
- Mishra, P., & Gowda, D. (2015). Application of Predictive Engineering Tool (ABAQUS) to Determine Optimize Rubber Door Harness Grommet Design. In *2015 SIMULIA Community Conference* (pp. 1–7).
- Mooney, M. (1940). A Theory of Large Elastic Deformation. *Journal of Applied Physics*, 11(153).
- Ogden, R. W. (1972). Large Deformation Isotropic Elasticity: On the Correlation of Theory and Experiment for Compressible Rubberlike Solids. *Proceedings of the Royal Society A: Mathematical, Physical and Engineering Sciences*, 328(1575), 567–583.
- Pan, B., Qian, K., Xie, H., & Asundi, A. (2009). Two-dimensional digital image correlation for in-plane displacement and strain measurement: A review. *Measurement Science and Technology*, 20(6), 62001–17.
- Pearson, I., & Pickering, M. (2001). The determination of a highly elastic adhesive's material properties and their representation in finite element analysis. *Finite Elements in Analysis and*

- Design, 37, 221–232.
- Pitchumani, R., Ranganathan, S., Don, R. C., Gillespie, J. W., & Lamontia, M. A. (1996). Analysis of transport phenomena governing interfacial bonding and void dynamics during thermoplastic tow-placement. *International Journal of Heat and Mass Transfer*, 39(9), 1883–1897.
- Rivlin, R. S. (1948). Large Elastic Deformations of Isotropic Materials. I. Fundamental Concepts. In *Philosophical Transactions of the Royal Society of London A* (Vol. 240, pp. 459–490).
- Romanov, K. I. (2001). The Drucker stability of a material. *Journal of Applied Mathematics and Mechanics*, 65(1), 155–162.
- Sasso, M., Palmieri, G., Chiappini, G., & Amodio, D. (2008). Characterization of hyperelastic rubber-like materials by biaxial and uniaxial stretching tests based on optical methods. *Polymer Testing*, 27(8), 995–1004.
- Schell, J. S. U., Guilleminot, J., Binetruy, C., & Krawczak, P. (2009). Computational and experimental analysis of fusion bonding in thermoplastic composites: Influence of process parameters. *Journal of Materials Processing Technology*, 209(11), 5211–5219.
- Shahzad, M., Kamran, A., Siddiqui, M. Z., & Farhan, M. (2015). Mechanical Characterization and FE Modelling of a Hyperelastic Material. *Materials Research*, 18(5), 918–924.
- Shih, P., & Loos, A. C. (1997). Design of Experiments Analysis of The On- Line Consolidation Process. *Eleventh International Conference on Composite Materials, IV*, 92–102.
- Standard ASTM. (2012). D575. Standard Test Methods for Rubber Properties in Compression.
- Standard ASTM. (2016). \_412. Standard Test Methods for Vulcanized Rubber and Thermoplastic Elastomers— Tension.
- Standard ISO. (2011). D37. Rubber, vulcanized or thermoplastic — Determination of tensile stress-strain properties.
- Stokes-Griffin, C. M., & Compston, P. (2016). An inverse model for optimisation of laser heat flux distributions in an automated laser tape placement process for carbon-fibre/PEEK. *Composites Part A: Applied Science and Manufacturing*, 88, 190–197.
- Szabo, B. A. (1984). Estimation and Control Error Based on P-Convergence. WASHINGTON UNIV ST LOUIS MO CENTER FOR COMPUTATIONAL MECHANICS.
- Tannous, M., Barasinski, A., Binetruy, C., & Courtemanche, B. (2016). Contribution of thermo-mechanical parameters and friction to the bonding of thermoplastic tapes in the tape winding process. *Journal of Materials Processing Technology*, 229, 587–595.
- ThreeBond. (2008). Datasheet of ThreeBond 7738. Retrieved from [http://tranzistor.ru/bitrix/TB/TDs\\_ENG/7738.pdf](http://tranzistor.ru/bitrix/TB/TDs_ENG/7738.pdf)
- Tierney, J., & Gillespie, J. W. (2006). Modeling of In Situ Strength Development for the Thermoplastic Composite Tow Placement Process. *Journal of Composite Materials*, 40, 1487–1506.
- Treloar, L. R. (1975). *The physics of rubber elasticity*. Oxford University Press, USA.
- Wang, C. L., Cheng, C. K., Chen, C. W., Lu, C. M., Hang, Y. S., & Liu, T. K. (1995). Contact areas and pressure distributions in the subtalar joint. *Journal of Biomechanics*, 28(3).
- Wool, R. P., Yuan, B. -L., & McGarel, O. J. (1989). Welding of polymer interfaces. *Polymer Engineering & Science*, 29(19), 1340–1367.
- Wriggers, P. (2008). *Nonlinear finite element methods*. Springer Science & Business Media.
- Yousefpour, A., & Ghasemi Nejjhad, M. N. (2001). Experimental and Computational Study of APC-2/AS4 Thermoplastic Composite C-Rings. *Journal of Thermoplastic Composite Materials*, 14(2), 129–145.
- Yu, T., Shi, Y., He, X., Kang, C., & Deng, B. (2017). Modeling and optimization of interlaminar bond strength for composite tape winding process. *Journal of Reinforced Plastics and Composites*, 36(8), 579–592.
- Zienkiewicz, O. C. (2005). *The finite element method for solid and structural mechanics*. Elsevier



# Appendices

## A.1. Sample manufacturing for rubber characterization

Rubber samples are made by the following procedure (Bachus et al., 2006):

1. Mix the rubber base and curing agent with the ratio of 10:1. It is difficult to mix the rubber mixture at the bottom and along the edge. Thus, it is wise to pour the rubber mixture to another bucket so that the poorly mixed portion can be mixed properly. In addition, the mixture left at the bottom and along the edge is scraped down using a wooden stick as much as possible and it is done by same person, so that the variations in the mixing ratio can be minimized.
2. Degas under vacuum (around 5 millibar) for 15 minutes to eliminate entrapped air bubbles in the rubber mixture.
3. Clean the mold with acetone during degassing.
4. Either directly pour the mixture into the mold or use injection from a pneumatic injection syringe, depending on the sample geometry.

### A1.1 Rubber ring sample for experimental validation and tensile test

Those rubber ring covers are made by molding. The mold is shown in Fig A1.1 below. The inner cylinder is made of POM and outer part is made of Teflon. The bottom lid can be fixed to the other two parts by bolts, which eliminates the gap in between them for an easier mold release.



*Figure A1.1 Mold for rubber ring manufacturing*

Uncured rubber mixture is injected from the top due to its high viscosity so that rubber does not drop off but slowly slide down (Fig A1.2). This is also done by a pneumatic injection syringe. The rubber ring is then cured at room temperature for 10 hours.



*Figure A1.2 Injecting process*

Once it is cured, bottom lid can be easily separated after removing the bolts (shown in Fig A1.3). A pulley puller is used for de-molding. Moreover, small rubber rings can be cut by the turning machine as the samples for tensile testing.

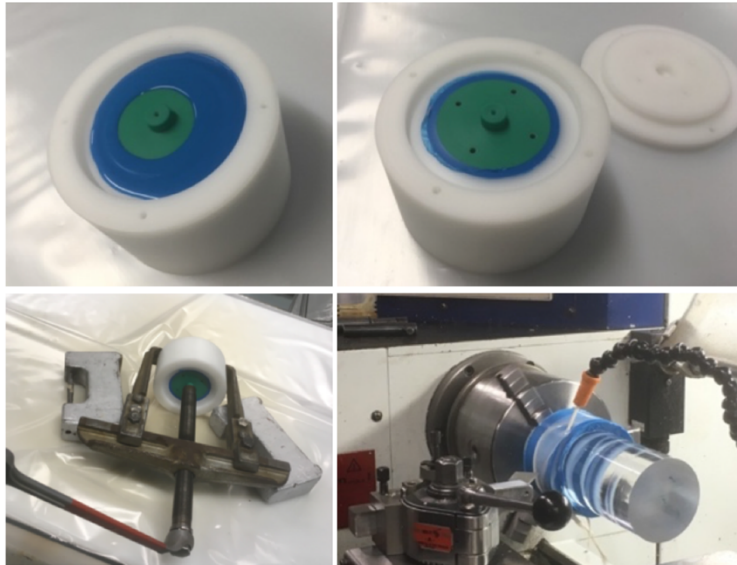


Figure A1.3 Post processing

### A1.2 Rubber cylinder for compressive test

Cylindrical rubber samples are used for compressive testing based on ASTM D575 (Standard ASTM, D575, 2012), with the diameter of 28 mm and the thickness of 12.5 mm. The mixing procedure is explained in section 3.1.1. A mold is made by 3D printing using the standard grey material (Formlabs., 2017) (GPGR02) provided by Formlabs® and post cured by LED light at 60°C for one hour. As shown in Fig A1.4, The mold is capable of making 3 samples at once. The rubber is injected by a pneumatic injection syringe. The lid is then closed with clamps and the samples were cured at room temperature for 10 hours. The sample surface might be contaminated with newly printed mold. In this case, samples are post cured at 80° for one hour. Fig 3.5 shows good repeatability in the compressive strain range from -0.35 to 0. Among all 6 samples, three samples are with post curing and three are without the post curing, indicating the possible surface contamination has a negligible influence on the compressive properties.



Figure A1.4 Procedures of cylinder sample manufacturing

### A1.3 Rubber film for planar tension test

The sample dimensions for planar tension test are determined by Shahzad *et al.*'s work (Meunier et al., 2008): length x width x thickness = 55 mm x 110 mm x 2 mm and the deformable length is 15 mm. The mold of rubber film is made of two metal plates with 2mm-thick metal spacers along the sides. Uncured rubber mixture is poured to the mold, which is later clamped vertically for curing (shown in Fig A1.5). After curing, rubber film is cut to the

final dimensions by a knife.

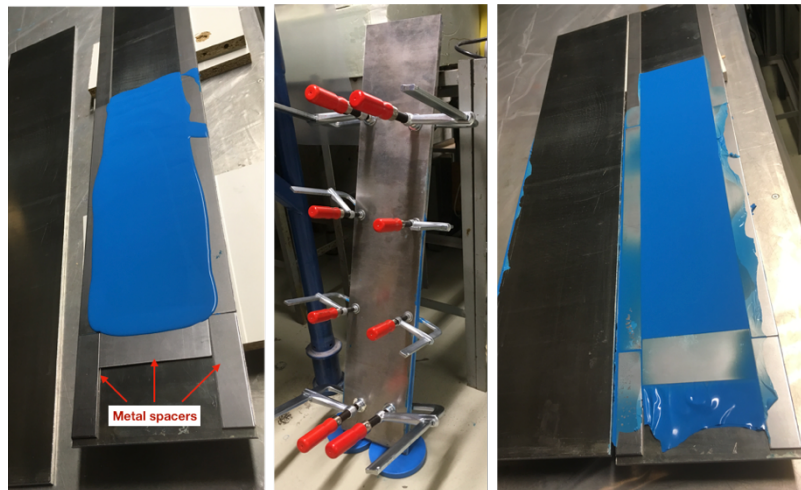


Figure A1.5 Procedures of film sample manufacturing: molding (left), vertically curing (middle) and mold releasing (right)

Rubber films are bonded with metal strips to constrain lateral deformation, as stated in Fig 2.12. This can also provide better clamps. The adhesive is Threebond 7738 (ThreeBond, 2008). Surface treatments are applied both rubber and metal strips to ensure a good bonding quality, including sand-blasting for metal strips and plasma treatment for rubber films. As shown in Fig A1.6, a 15mm-wide metal strip used as a spacer to keep the desired grip separation. Additionally, Strip edges are sanded to prevent the sharp edges from damaging rubber film during clamping.

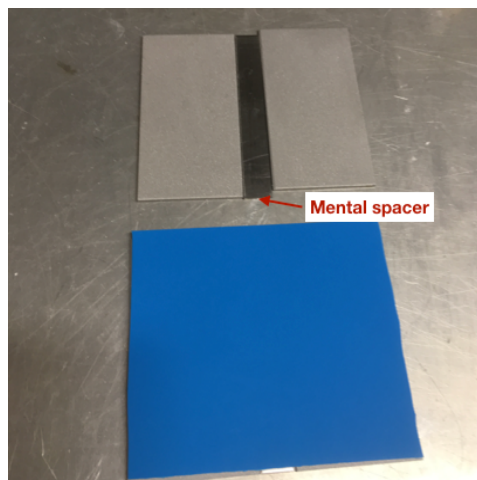


Figure A1.6 Gluing the metal plates to rubber film

## A.2. Detailed descriptions of finite element models

### A2.1 Two-dimensional static contact model.

*Interactions. Contact formulations and numerical methods*

Fig A2.1 shows the interaction properties for both Int-1 and Int-2 (the properties for Int-1 are presented as an example). Explanations for the most relevant options for the contact analysis are provided below.

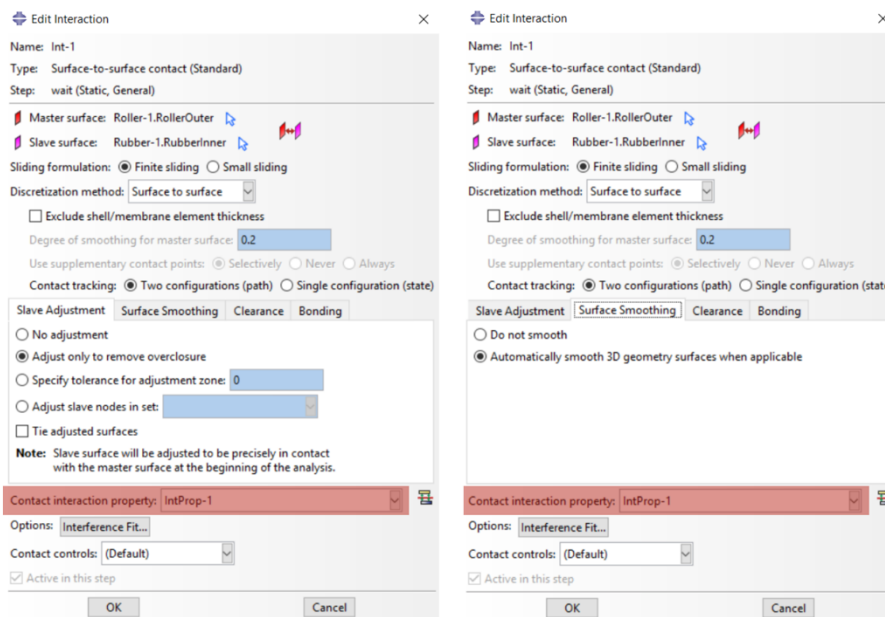


Figure A2.1 Interaction setup

**Discretization of contact pair surfaces.** Surface-to-surface option is used because it provides more accurate stress and pressure results when compared to node-to-surface discretization (Abaqus, 2011).

**Contact tracking approaches.** The finite-sliding tracking approach enables arbitrary relative separation, sliding, and rotation of the contacting surfaces while relatively little sliding of one surface along the other is assumed in the small-sliding tracking approach (Abaqus, 2011). The small-sliding tracking approach is mostly used for surfaces that do not deform relative to each other under loading (such as a shrink fit). Therefore, finite-sliding approach is more suitable for this model. Furthermore, the path-based algorithm is chosen, owing to its effectiveness when large incremental relative motion is involved (Abaqus, 2011).

**Surface Smoothing.** Automatically smoothing 3D geometry surfaces is applied to increase the accuracy for axisymmetric surfaces (Abaqus, 2011).

### Contact property models

Contact interaction properties should be also defined and assigned to the contact interaction mentioned above, as highlighted in red in Fig A2.1. These properties define the tangential and normal behaviors of contacting surfaces. The main choices made for these options are explained below.

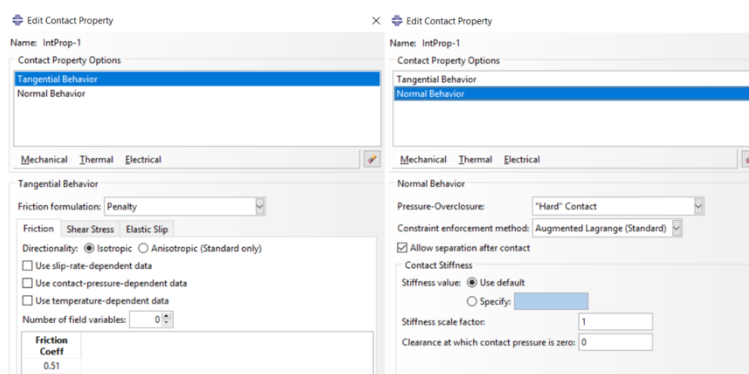


Figure A2.2 Interaction properties setup

*Frictional behavior.* The isotropic Coulomb friction model is used by defining a friction coefficient between silicone rubber and Aluminum (Abaqus, 2011).

*Pressure-overclosure.* A “hard” contact pressure-overclosure relationship is applied by default, which minimizes the penetration of the slave surface into the master surface at the constraint locations (Abaqus, 2011). Additionally, whether the zero-penetration condition is strictly enforced or not depends on the constraint enforcement method (Abaqus, 2011).

*Constraint enforcement methods.* The augmented Lagrange method uses linear penalty method within an augmentation iteration scheme that reduces the penetration distance more effectively than linear penalty method (Abaqus, 2011). If the penetration distance of a node on the slave surface is larger than penetration tolerance, the contact pressure is “augmented” and another series of iterations is computed until convergence is again reached (Abaqus, 2011). The default penetration tolerance is 5% of the characteristic interface length for surface-to-surface contact with finite-sliding (Abaqus, 2011).

### Steps

General static step type is used to analyze the static problem (Abaqus, 2011), which is applicable to all four steps. As mentioned before, nonlinear analysis is made for all four steps by switching Nlgeom on as indicated in Fig A2.3 (left). Obtaining a convergent solution is one of the main challenges in nonlinear FEM analysis. Accordingly, it is more efficient to use automatic control of the time increment when compared to the fixed control, where the initial step and minimum step size should be small for easier convergence (Abaqus, 2011). The details are shown in Fig A2.3 (right).

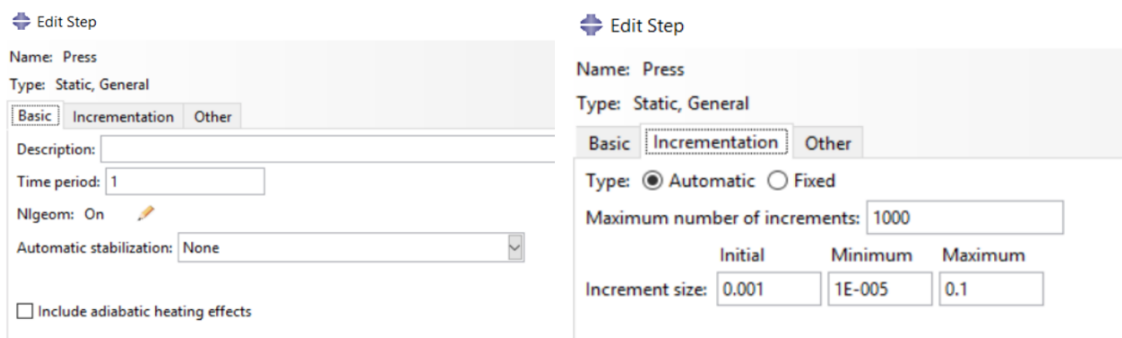


Figure A2.3 Step setup for 2D static model

## A2.2 Three-dimensional static contact model

### Steps

Compared to the 2D static contact model, the difference in step setup lies in the automatic stabilization (Fig A2.4), which is used to improve stability by introducing an artificial damping factor, enable an easier convergence for nonlinear problems (Abaqus, 2011). The dissipation energy will be checked for the model with converged mesh, which should be below 2% of the

strain energy.

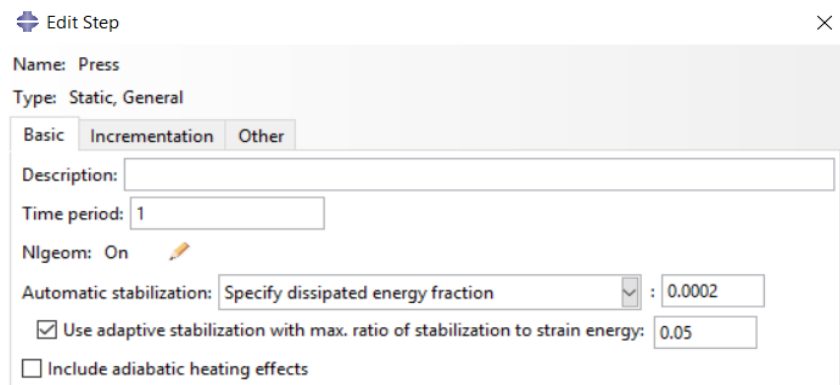


Figure A2.4 Step setup for 3D model

### A2.3 Two-dimensional rolling model.

#### Steps

The setup of the rolling step is illustrated in Fig A2.5. The time period has a physical meaning, which corresponds to the real time it takes for the mandrel to rotate half round as defined in the rolling step. Therefore, a constant rolling speed can be applied by specifying a time period in this step. The commonly applied rolling speed is 100 mm/s for the tape winding process with in-situ consolidation as stated by Stokes-Griffin *et al.* (Stokes-Griffin & Compston, 2016). The time ( $t_{rolling}$ ) of 4.4 s is calculated using the following equation

$$t_{rolling} = \frac{\pi D_{mandrel}}{v_{rolling}}$$

A2-1

where  $D_{mandrel}$  is the mandrel diameter (140 mm) and  $v_{rolling}$  is the rolling speed.

The rest in the setup of the rolling setup is used as default.

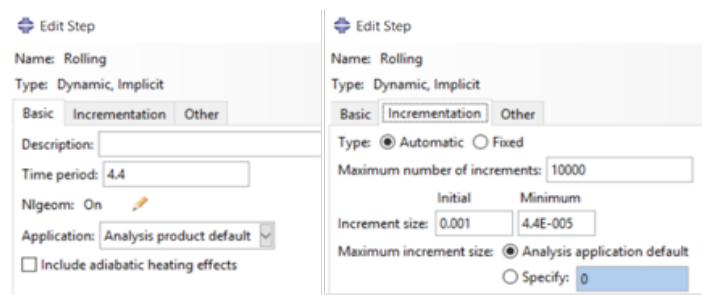


Figure A2.5 Step setup for 2D rolling model

### A.3. Image process of digital image correlation

In the digital image correlation (DIC), the scanned images are processed to obtain the grayscale map and the pressure distribution can be calculated at every pixel based on the calibration curve as discussed in section 5.4.1. The image processing algorithm is developed based on Brulotte *et al.*'s work (Brulotte *et al.*, 2012) using Matlab, which is illustrated in a flow chart as show in Fig A3.1. The main difference is that the averaged grayscale was calculated

at every pixel by Brulotte *et al.*'s work. However, it is calculated at every pixel block in this algorithm, which saves the computational time significantly.

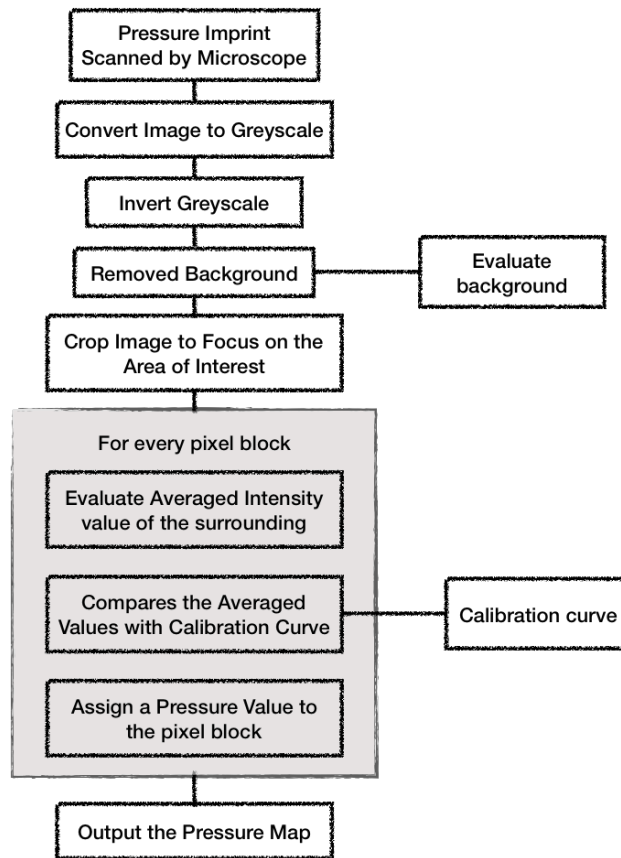


Figure A3.1 Flow chart to obtain the pressure map from the scanned pressure imprint image

Figure A3.2 shows the graphical output at each stage during the image process. (a) is the original image scanned by a microscope, resulting from the image stitching function provided by the microscope, since the image is too large and it is not possible to scan the entire image even using the lowest amplification factor (x 20). (b) is the grayscale image converted from the RGB image of (a) by forming a weighted sum of the R, G, and B components (Matlab, 2017):

$$0.2989 * R + 0.5870 * G + 0.1140 * B$$

A3-1

After inverting the grayscale (image (c)) and removed the background, (d) is the obtained by cropping the image (c), where the crop rectangular is shown in (c) as dashed line rectangular. Then, the grayscale is averaged on a blocked based, which is further explained later. Lastly, pressure distribution (image (f)) can be calculated at each pixel based on the calibration curve mentioned in section 5.4.1.

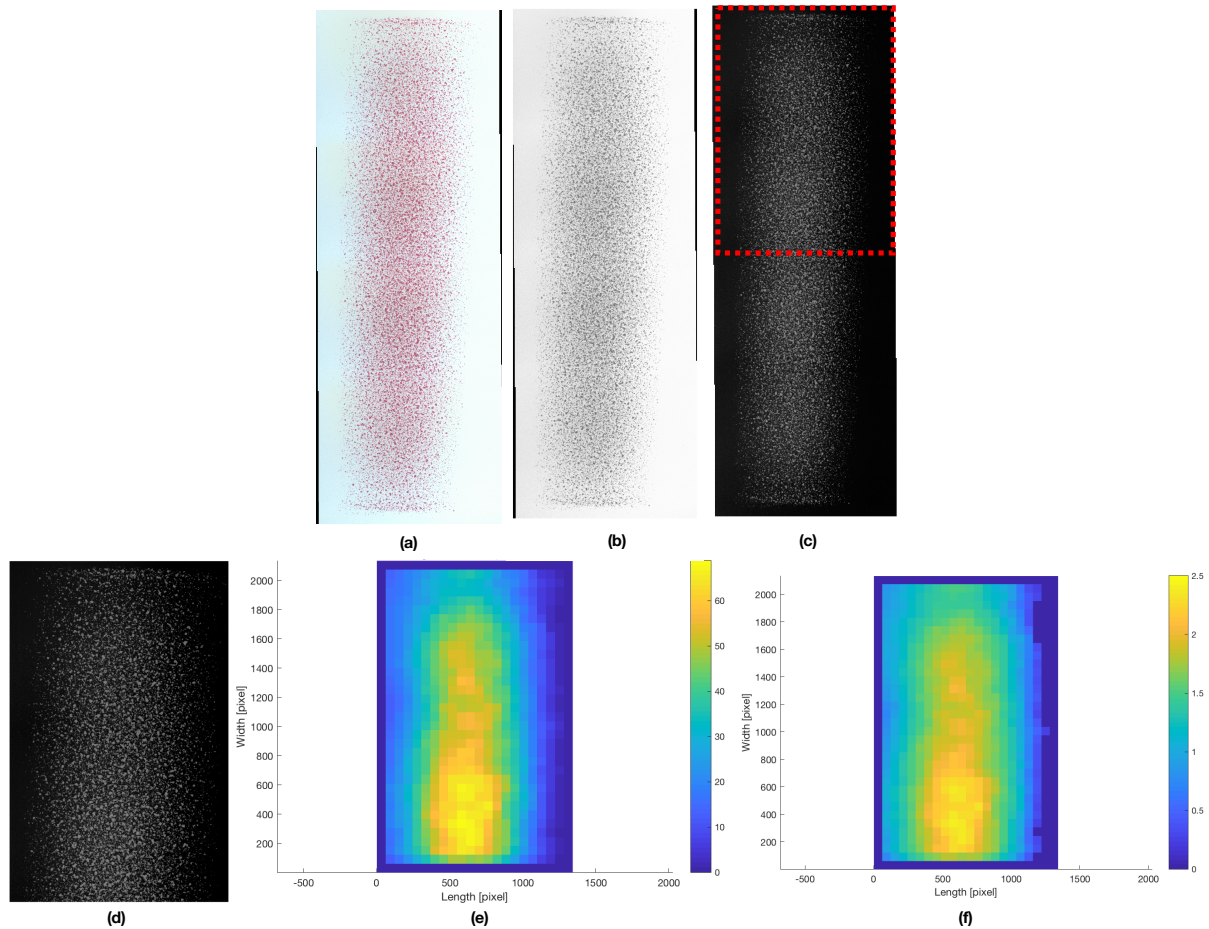


Figure A3.2 Graphical output during image processing: (a) scanned image of the pressure imprint, (b) convert the image to grayscale, (c) invert the grayscale map, (d) crop the image and remove the background, (e) grayscale map and (f) pressure map

The grayscale is averaged at on a blocked base. For instance, Fig A3.3 presents a image of 10 x 10 pixel, where each gray rectangular stands for one pixel. The block size is 2 pixels (darker blue rectangular). When averaging the grayscale, all four pixel values in each block are processed together and the values are calculated by averaging the block and its surrounding (lighter blue block), which is a 3 x 3 pixel in this case. The size of the surrounding is defined as border size. The result of the averaged grayscale map is greatly influenced by the block size and the border size. Usually, the block size should be smaller than twice of the subset size. Here the block size is the two time of the border size. Fig A3.4 compares the pressure results using two different combinations of block size and border size. After averaging, the grayscale map should be consistent. However, small block size and border size (Fig A3.4 right) still reveals the inconsistent nature of the color density in the pressure imprint. Therefore, larger block size and border size should be applied. Fig A3.4 (left) shows a consistent pressure distribution using larger block size and border size and it is acceptable. As a result, all the pressure map results are obtained using the block size of 59 and the border size of 30 pixels.

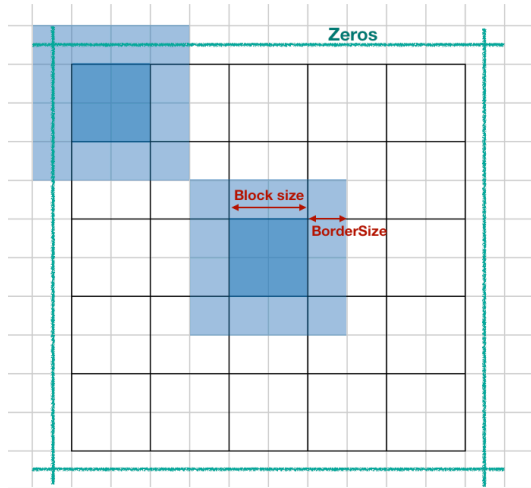


Figure A3.3 Illustration of averaging the grayscale map

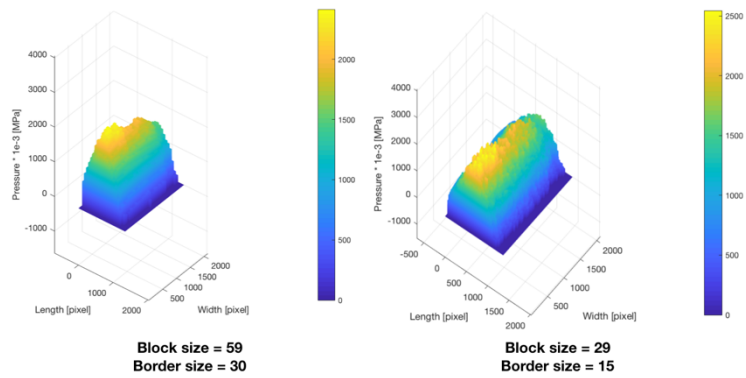


Figure A3.4 Pressure results using different block size and border size [pixel]